Magnesium Silicide Based Thermoelectric Nanocomposites

by

Nader Farahi

A thesis
presented to the University of Waterloo
in fulfillment of the
thesis requirement for the degree of
Doctor of Philosophy
in
Chemistry

Waterloo, Ontario, Canada, 2016

AUTHOR'S DECLARATION

I hereby declare that I am the sole author of this thesis. This is a true copy of the thesis, including any required final revisions, as accepted by my examiners.

I understand that my thesis may be made electronically available to the public.

Abstract

The major objective of this thesis was to investigate how far the thermoelectric (TE) properties of magnesium silicide based materials can be enhanced via doping, alloying, and nanostructuring.

The investigation of Sb and Bi doped Mg_2Si showed experimentally that the dopants can indeed substitute Si in the crystal lattice. The excess Sb and Bi atoms were found in the grain boundaries, most likely in the form of Mg_3Sb_2 and Mg_3Bi_2. As a consequence, the sample showed lower carrier concentration than the formal Sb/Bi concentration suggests, and the thermal conductivity was significantly reduced.

The investigation of the effect of germanium substitution for silicon in bismuth doped Mg_2Si, showed that the alloying drastically reduced the room temperature thermal conductivity partially due to the added mass contrast and the existence of Ge-rich domains within the sample. Due to the increased in the amount of scattering centers caused by Ge alloying, the electrical conductivity was also decreased while the Seebeck coefficient was increased only very slightly. In summary, the positive effect of Ge substitution on the TE properties of Bi doped Mg_2Si resulted in a figure of merit of 0.7 at 773 K for $Mg_2Si_{0.677}Ge_{0.3}Bi_{0.023}$ sample.

The addition of multi wall carbon nanotubes (MWCNT) to the $Mg_2Si_{0.877}Ge_{0.1}Bi_{0.023}$ resulted in an improved electrical conductivity, in particular around room temperature. The Seebeck coefficient of all nanocomposites is enhanced at 773 K due to energy filtering that stems from the introduction of CNTs - $Mg_2Si_{0.877}Ge_{0.1}Bi_{0.023}$ interfaces. The lattice thermal conductivity of the nanocomposites is reduced due to the phonon scattering by nanodomains and grain, particularly at medium temperatures, resulting in a slight reduction in total thermal conductivity. All in all, the thermoelectric figure of merit of the sample containing 0.5 weight-% MWCNT was enhanced by about 22% as compared to the pristine sample.

Finally, the investigation of the effect of silicon carbide (SiC) nanoparticles on the TE properties of $Mg_2Si_{0.676}Ge_{0.3}Bi_{0.024}$ revealed that increasing the concentration of SiC

nanoparticles systematically reduced the electrical conductivity, while enhancing the Seebeck coefficient. In spite of its high thermal conductivity, SiC could successfully decrease the lattice thermal conductivity through adding more interfaces. The HRTEM study showed the existence of both Ge and Bi in the Si position, and some Bi segregation at the boundary. In summary, the figure of merit reached its maximum value of 0.75 at 773 K for the sample containing 0.5 wt.-% SiC, which is among the highest achieved in the $Mg_2Si_{1-x}Ge_x$ system.

Acknowledgements

Dedication

To all the people who try to make the world a better place to live

"There is only one good, knowledge, and one evil, ignorance."

~Socrates~

Table of Contents

List of Figures

List of Tables

Chapter 1

Introduction to Thermoelectricity[*]

1.1 Why Thermoelectrics?

Undoubtedly, energy is one of the biggest challenges that mankind faces in this era. With simultaneous reduction of fossil fuel resources and increase in population around the world, reliance on consuming fossil fuels would not be feasible without proper energy management. Different strategies are being pursued to reduce the dependency on fossil fuels, through the development of a variety of alternative and renewable energy sources. To convert waste heat into useful energy, thermoelectric (TE) materials are inimitable due to their unique ability to convert heat into electricity. As one of the emerging technologies, certain obstacles such as efficiency, profusion and toxicity of these materials need to be addressed before establishing them for industrial applications. In this chapter, an introduction to thermoelectric effects together with an overview on silicide thermoelectrics and future materials will be presented.

1.2 Thermoelectric Effects

In 1821 Thomas Johann Seebeck a German physicist, observed when the junctions of a circuit made of two different conductors held at different temperatures, can deviate a compass needle close to it. This phenomenon is due to the magnetic force which is created by the current passing through the circuit. The current itself generated from the temperature gradient at the junctions. This effect is the foundation of thermoelectric effect that named after Seebeck (Figure 1.1   (a) Thermoelectric power generation through Seebeck effect; (b) thermoelectric Refrigeration through Peltier effect.Figure 1.1a).[1] The Seebeck coefficient (*S*) is equal to the ratio of the induced voltage (Δ*V*), caused by the temperature gradient at the two junctions (Δ*T*) (Equation 1.1).

$$S = \frac{\Delta V}{\Delta T}$$
<div align="right">Equation 1.1</div>

This sign of the Seebeck coefficient rely on the type of major charge carriers of the materials (negative for *n*-type and positive for *p*-type materials). The dimension is in (V/K) which for convenience is stated as (μV/K).

Around thirteen years after the discovery of Seebeck, Jean Charles Athanase Peltier a French physicist, noticed passing a current through a circuit made of two different materials can change the temperature at the junctions (Figure 1.1b).[2] This is due to the heat generated or absorbed at the contacts with respect to the direction of a passing current. This phenomenon is known as the Peltier effect. The ratio of the heat carried through charges (*Q*) to the passing current across the junction (*I*) is expressed as the Peltier coefficient (π) (Equation 1.2).

$$\pi = \frac{Q}{I}$$
<div align="right">Equation 1.2</div>
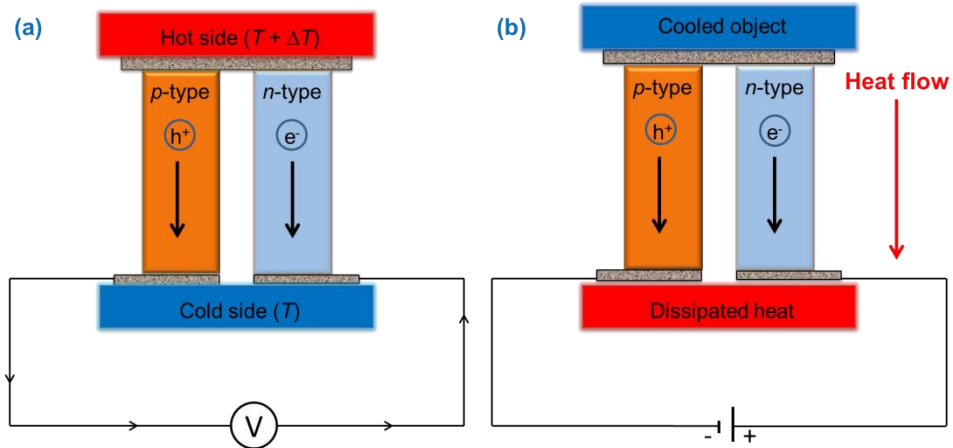
Figure 1.1   (a) Thermoelectric power generation through Seebeck effect; (b) thermoelectric Refrigeration through Peltier effect.

Seventeen years after the discovery of the Peltier effect, William Thomson (known as Lord Kelvin) explained the thermodynamic correlation between Seebeck and Peltier effects which is known as Thomson effect (Equation 1.3).[3] In this effect, heat will be absorbed (carriers moving in opposite to the thermal gradient) or produced (carriers moving parallel to the thermal gradient) by passing a current in a material with a temperature gradient.

$$\pi = S.T \qquad\qquad \text{Equation 1.3}$$

1.3 Thermoelectric Efficiency

The criteria for evaluating the efficiency of a thermoelectric material in its modern concept was developed by Abram Fedorovich Ioffe (1949).[4] The figure of merit ZT is shown in Equation 1.4 which was derived thermodynamically.

$$ZT = \frac{S^2 \sigma}{\kappa} T \qquad\qquad \text{Equation 1.4}$$

3

Where S, σ, κ and T represent the Seebeck coefficient, electrical conductivity, thermal conductivity and absolute temperature, respectively. The average figure of merit over temperature ($\overline{ZT}$) can be used to calculate the efficiency of thermoelectric module. The efficiency of the device working between the hot (T_h) and cold (T_c) side is expressed by Equation 1.5, and is constrained by the Carnot efficiency.

$$\eta = \frac{T_h - T_c}{T_h} \frac{\sqrt{1+\overline{ZT}}-1}{\sqrt{1+\overline{ZT}}+\frac{T_c}{T_h}}$$
Equation 1.5

1.3.1 Strategies to improve thermoelectric performance

In an ideal case, doping is achieved through substituting the lattice atoms with the atoms of suitable elements without disturbing the structure. This has been proven to be an efficient way to improve the ZT in many conventional materials, such as Bi_2Te_3, PbTe, and SiGe. Since introducing foreign atoms into the structure can dramatically affect the mobility of carriers, it is recommended to start with only small amount of doping concentration and increase gradually.

To enhance ZT, the electrical conductivity and the Seebeck coefficient need to be increased while maintaining or reducing the thermal conductivity. Unfortunately these properties are entangled in such a way that simultaneous improvements are not always feasible, as for example both the electrical and the thermal conductivity increase with higher charge carrier concentration, while the Seebeck coefficient decreases. One of the strategies to overcome this issue was proposed by Glen A. Slack, known as the PGEC concept, which represents "a phonon glass and an electron single crystal".[5] This means a material which possesses a short phonon and a long electron mean free path. It has been found that the phonon mean free path in a glass at room temperature is in the scale of the structure of the glass, i.e. approximately 7 Å, and a relationship between the glass-like thermal conductivity and the minimum value has been established.[6] Consequently, compounds containing heavy elements, such as Tl, Pb, Bi, or Te are expected to decrease sound velocity therefore lattice

4

thermal conductivity which leads to large *ZT* values. Some methods used for reducing the lattice thermal conductivity for approaching the minimum value include: i) to use solid solutions to create mass fluctuation scattering, which will usually lower the phonon mobility, ii) to disrupt the periodicity and create defects, iii) to introduce rattling atoms or ions into caged structures, and iv) to generate fine microstructures. Several materials have been proven to satisfy the PGEC concept, including skutterudites, β-Zn_4Sb_3, and clathrates[7]. The search for these materials is ongoing, which majorly focuses on small bandgap semiconductors containing heavy elements with low electronegativity differences.

Nanostructuring has been experimentally shown to be an effective method to enhance *ZT* through reducing the lattice thermal conductivity for various thermoelectric materials. This technique was found to drastically increase the number of interfaces, therefore enhance the phonon scattering. However, the optimal sizes of the nanostructures strongly depend on the phonon and electron mean free path of the matrix material. One of the strategies to enhance *ZT* is through embedding nanomaterials into the bulk matrix, which is known as "nano-inclusion".[8] The idea of having nanostructures is to reduce thermal conductivity through scattering of the mid- to long- wavelength phonons, and to sustain electrical conductivity while improving the Seebeck coefficient via energy filtering of carriers.[8–10] The nanoscale inclusions in nanocomposites can vary from nanoparticles,[11] to nanowires,[12] nanotubes,[13] or nanohorns.[14] The nanocomposite materials are potentials for scaled-up production and practical applications.

1.4 Thermoelectric Applications

Probably the best known application of thermoelectrics is the thermocouples, in which loops are made from wires using two dissimilar metals (Figure 1.2).[15] The operating principle of thermocouples is based on the Seebeck effect, where the junction end is in contact with or immersed in the part whose temperature needs to be identified, and the tail end is kept at ambient temperature. The temperature difference between these two sides induces an electrical potential at the tail end. Thermocouples are made of specific alloys with

a known relationship between temperature and voltage, depending on the applied temperature ranges and working environment. Therefore, the temperature of the object can be determined from the induced voltage gained from the measurement.
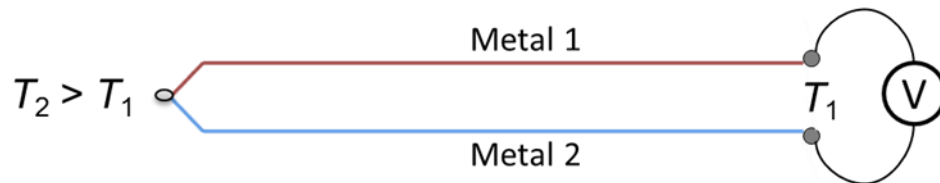
Figure 1.2   Schematic description of thermocouples.

One of the best applications of thermoelectric materials may be in automotive industry. Since, around 40% of the combustion energy in a gasoline engine is released as waste heat, leading to the temperature of the exhaust gas in excess of 500°C. Utilizing the temperature gradient between the exhaust gas and the cooling system (100°C) to generate power for the accessories can improve the fuel economy. Such thermoelectric devices are currently being tested on different cars and trucks by companies such as General Motors.

For space exploration missions, the electric power is provided to the spacecraft by converting the heat from the natural decay of a Plutonium-238 source into electricity using Radioisotope Thermoelectric Generators (RTG). These generators have been used by NASA for various missions, such as Apollo, Viking, Pioneer, or Voyager.[16] The Multi Mission Radioisotope Thermoelectric Generators (MMRTG) is the latest RTG model, allowing the Curiosity Mars rover (Figure 1.3b) to properly operate in cold environments, which is currently providing scientists valuable data about the planet Mars.[17]

Figure 1.3   Curiosity Mars rover using a MMRTG to generate electric power (Courtesy NASA/JPL-Caltech.).

Thermoelectric cooling devices are highly reliable thanks to their solid construction with no moving parts. Moreover, they are light weighted and small sized, and produce no noise or harmful emission. IBM has expressed its interest in thermoelectric cooling since early times, and developed several cooler models for memory arrays and chips on wafers.[18] Nowadays, Peltier coolers are widely used for CPU coolers and laptop cooling pads, climate control seats, cool boxes and refrigerators, which brings massive profits to the refrigeration industries.

1.5 State-of-the-Art Materials

1.5.1 Materials for room temperature applications (300 K - 400 K)

Bi_2Te_3-based materials are the leading thermoelectrics for room temperature applications. The energy gap of undoped Bi_2Te_3 is 0.16 eV at 300 K with a carrier concentration of 8×10^{18} cm^{-3} and 5×10^{18} cm^{-3} for holes and electrons, respectively.[19] The energy gap of Bi_2Se_3 is approximately 0.08 eV with the carrier concentration in the order of 10^{19} cm^{-3},[20] while the values of Sb_2Te_3 are 0.28 eV and 10^{20} cm^{-3}.[21] The p-type compound Sb_2Te_3 operates in the same temperature range as Bi_2Te_3 with a peak *ZT* of approximately 1.0 around 300 K.[22] The solid solutions $Bi_2(Te_xSe_{1-x})_3$ and $(Bi_{1-x}Sb_x)_2Te_3$ crystallize in the same crystal structure type in the space group $R\bar{3}m$. The figure of merit of $Bi_2(Te_xSe_{1-x})_3$ was

7

approximately 0.6 for randomly orientated polycrystalline material, while an enhanced value of 0.9 was obtained for the aligned conformation.[23] The large-grained material $(Bi_{1-x}Sb_x)_2Te_3$ reached a maximum *ZT* of 1.0 at 300 K, which was significantly improved via nanostructuring, achieving a *ZT* of 1.4 at 300 K for the $Bi_{0.48}Sb_{1.52}Te_3$ nanocomposites.[24] The Currently highest *ZT* reached 1.5 at 390 K for *p*-type Bi_2Te_3-based materials,[24] and the maximum value of the *n*-type compounds was around 1.2 at 423 K.[25]

1.5.2 Materials for intermediate temperature applications (400 K - 800 K)

The silver antimony telluride $AgSbTe_2$ has recently been considered as a prospective thermoelectric material in the moderate temperature range 400 K – 700 K owing to its low thermal conductivity and high Seebeck coefficient. This material has a cubic rock salt structure with random occupation of Ag and Sb at the cationic sites. A bandgap of 0.35 eV was revealed by diffuse reflectance measurements,[26] with a carrier concentration of 1.6×10^{19} cm^{-3}.[27] Evidently doping is an effective approach to improve thermoelectric performance of *p*-type $AgSbTe_2$ through reducing its thermal conductivity and adjusting the carrier concentration. The Se containing material achieved a high *ZT* of 1.4 at 565 K for the composition $AgSbSe_{0.02}Te_{1.98}$.[27]

The LAST materials, implying Lead-Antimony-Silver-Telluride formulated as $Pb_{2-x-y}Ag_ySb_xTe_2$, which are roughly solid solutions between silver antimony telluride ($AgSbTe_2$) and lead telluride (PbTe), are promising candidates for thermoelectric generators. The family of bulk cubic compounds with general formula $Ag_nPb_mM_nTe_{m+2n}$, where M = Sb or Bi, possesses desirable properties for thermoelectric materials, such as isotropic morphology, low thermal conductivity, and tunable carrier concentration. The structure is described as an average rock salt crystal, where Ag, Pb, and M atoms disorderly occupy the Na sites, and the chalcogen atoms fill the Cl sites. The $AgPb_mSbTe_{m+2}$ series can be prepared for a range of m, in which the cell parameters smoothly change with m. In particular, the composition $AgPb_{10}SbTe_{12}$ showed low electrical conductivity and high Seebeck coefficient at room temperature. The power factor was further enhanced by departing from the stoichiometry, and the $Ag_{1-x}Pb_{10}SbTe_{12}$ compound revealed a low value of thermal conductivity comparable

with Bi_2Te_3. When n = 1 and m = 18, a very high ZT of 2.1 was reached at 800 K for $Ag_{1-x}Pb_{18}SbTe_{20}$.[28] When gradually replacing the Pb atoms in the LAST system with Sn atoms, the LASTT alloys, representing Lead-Antimony-Silver-Tellurium-Tin $Ag(Pb_{1-y}Sn_y)_mSbTe_{m+2}$, were obtained. The Sn replacements resulted in *p*-type semiconductors with a high ZT of 1.5 at 627 K depending on the compositions and morphologies.[29] However, the transport properties in the LASTT materials are not as easily tuned by varying the Ag or Sb concentrations as in the case of the Sn-free *n*-type compounds.[30] The Ag-free SALT system, signifying Sodium-Antimony-Lead-Tellurium $Na_{1-x}Pb_mSb_yTe_{m+2}$, has also achieved impressive ZT values caused by its remarkably low thermal conductivity. The figure of merit of $Na_{0.95}Pb_{20}SbTe_{22}$ significantly outperformed that of *p*-type TAGS and PbTe-based materials at 300 K, raised dramatically with increasing temperature, and reached 1.7 at 650 K.[31]

The skutterudite name was derived from a cobalt arsenide mineral containing nickel and iron substitutions at Co sites $((Co,Ni,Fe)As_3)$, found in Skutterud Mines, Modum, Buskerud, Norway. The structure is comprised of a large unit cell, where the constituent atoms have heavy masses, and similar electronegativity. Moreover, skutterudites form covalent frameworks with relatively large voids in which incorporated atoms are able to rattle, which reduces the lattice thermal conductivity due to phonon scattering.[32] Among different compounds of the binary skutterudite family, cobalt triantimonide $(CoSb_3)$ has attracted a lot of interest for its transport properties. This material possesses *p*-type characteristics with an indirect gap of 0.57 eV,[33] a carrier concentration of 4×10^{17} cm^{-3}, and an exceptionally high carrier mobility approaching 3445 cm^2 $V^{-1}s^{-1}$ at room temperature.[34] Cobalt triantimonide operates in the moderate temperature range up to 700 K with the ZT reaching 0.8 at around 600 K.[22] Recently, filled skutterudite antimonides have been identified as a potential class of thermoelectric materials. Compounds with the filled skutterudite structure, having the general formula $R_xM_4X_{12}$, whit R = La, Ce, Pr, Nd, or Eu, M = Fe, Ru, or Os, and X = P, As, or Sb, were discovered in 1977.[35] The Fe-based skutterudites, such as $CeFe_4Sb_{12}$ and $CeFe_{4-x}Co_xSb_{12}$, have been extensively studied by several research groups, resulting in a large ZT of 1.4 at 873 K.[36] Partial filled skutterudite $Yb_{0.19}Co_4Sb_{12}$ also

9

exhibited a high *ZT* of approximately 1.0 at 600 K.[37] Moreover, the *ZT* of double and multiple filled $CoSb_3$-based skutterudites reached a competitive high value of 1.4 at 800 K,[38] and 1.7 at 850 K,[39] respectively.

Among different compounds in the Zn-Sb system, the *β*-Zn_4Sb_3 phase, which is stable in the temperature range from 263 K to 765 K under inert atmosphere and ambient pressure, is a potential *p*-type thermoelectric material. This material possesses a relatively complex structure, which results in a low thermal conductivity, owing to the disorderly distribution of Zn atoms at various lattice positions.[40] An optical gap between 1.2 eV and 1.5 eV has been experimentally determined, with the carrier concentration of 9×10^{19} cm^{-3}.[41] The maximum *ZT* value of 1.3 has been achieved at 670 K.[42] However, the decomposition into ZnSb and Zn at above 373 K due to the loss of Zn under dynamic vacuum makes pure samples difficult to obtain for industrial applications.

Thallium-containing compounds have attracted a lot of attention as new thermoelectric materials due to their low thermal conductivity, which results in high thermoelectric performance. Among the ternary compounds of the Tl_2Te-Ag_2Te pseudo-binary system, the Ag_9TlTe_5 composition has a high *ZT* value of 1.2 at 700 K owing to its relatively low resistivity.[43] The materials $Tl_9Bi_{1-x}Te_6$, $Tl_{9-x}Bi_{1+x}Te_6$, $Tl_{10-x}Sn_xTe_6$, and $Tl_{10-x}Pb_xTe_6$ are ternary substitution variants of Tl_5Te_3. These compounds are *p*-type semiconductors with a narrow energy gap. High *ZT* values were reported to be 1.1 for $Tl_9Bi_{0.98}Te_6$ and 0.90 for $Tl_{8.98}Sb_{1.02}Te_6$ at 500 K,[44] while a large figure of merit in excess of 1 has been obtained to reach 1.3 for $Tl_{8.05}Sn_{1.95}Te_6$ and 1.5 for $Tl_{8.10}Pb_{1.90}Te_6$ at approximately 680 K.[45] However, the high toxicity of thallium limits the practical applications of these materials despite of their high thermoelectric performance.

1.5.3 Materials for high temperature applications (above 800 K)

Silicon germanium ($Si_{1-x}Ge_x$) alloys are the TE materials used for RTGs by NASA for space missions, e.g. in Voyager 1 and 2. Both Si and Ge adopt the diamond structure with similar lattice parameters of 5.43 Å and 5.66 Å, respectively. Consequently, $Si_{1-x}Ge_x$ solid solutions are able to form continuously over the whole compositional range. The optimum

doping level in $Si_{1-x}Ge_x$ system varies with composition and temperature in the range of 1×10^{20} cm^{-3} to 3×10^{20} cm^{-3} for n-type and 2×10^{20} cm^{-3} to 4×10^{20} cm^{-3} for p-type materials.[46] $Si_{1-x}Ge_x$-based devices can operate at high temperatures from 600 K to 1300 K without significant degradation. $Si_{0.8}Ge_{0.2}$ is among the best n-type thermoelectric materials, reaching a ZT of 1 at 900 K.[47] For p-type materials, boron and the III-V compounds have been used to tune the transport properties of $Si_{1-x}Ge_x$ alloys. The achieved ZT of p-type materials remained at approximately 0.6 at 900 K.[47] The maximum possible efficiency of $Si_{1-x}Ge_x$-based thermoelectric generators could be around 23% if the minimum thermal conductivity is approached without disturbing the electrical properties.[48]

Lead telluride (PbTe) and its related materials, lead-tin telluride ($Pb_{1-x}Sn_xTe$), belong to the IV-VI semiconductors, crystallizing in the cubic rock salt crystal structure, and possessing high thermoelectric performance in the intermediate temperature range (500 K – 900 K).[49] The energy gap of intrinsic PbTe is approximately 0.32 eV at 300 K with the carrier concentration in the range from 2×10^{18} cm^{-3} to 1.7×10^{19} cm^{-3}. The lead-tin telluride system forms continuous solid solutions obeying Vegard's law, whose energy gap at a certain temperature is a function of the compositions with the carrier concentration in the range from 10^{18} cm^{-3} to 10^{21} cm^{-3}. The commonly used dopants consist of PbI_2 or $PbBr_2$ for p-type, and Na_2Te or K_2Te for n-type PbTe-based compounds. Both n-type and p-type PbTe-based materials have been used in the early RTG designs of NASA for over 50 years in the Apollo and Viking 2 missions.[50] The n-type $PbTe_{1-x}I_x$ reveals a significantly high ZT of 1.4 in the temperature range of 700 K – 850 K,[51] while the p-type $Na_xPb_{1-x}Te$ also has a large ZT of approximately 1.4 at 750 K.[52] An alternative analog is lead selenide (PbSe), whose atomic and electronic structures are very similar to those of lead telluride. The thermoelectric efficiency ZT of PbSe is superior to PbTe at high temperature, which was estimated to reach 2.0 at 1000 K,[53] and experimentally achieved to be 1.2 at 850 K.[54]

A replacement for the p-type PbTe, is the Tellurium-Antimony-Germanium-Silver, Te-Sb-Ge-Ag, system (TAGS), which possesses low thermal conductivity in the temperature range from 300 K to 900 K. This has been studied extensively to avoid the presence of lead due to its toxicity. These materials are formed by alloying silver antimony telluride

11

(AgSbTe$_2$) with germanium telluride (GeTe), in which a structural transformation from a rhombohedral structure to a cubic structure at room temperature exists between 75% and 90% GeTe content.[55] Among the (AgSbTe$_2$)$_{1-x}$(GeTe)$_x$ materials, the alloys containing 80% (TAGS-80) and 85% (TAGS-85) GeTe have minimum lattice thermal conductivity of less than 0.8 W m^{-1}K^{-1} over the whole temperature range.[56] The TAGS-80 composition is preferred considering its better thermoelectric properties, while the TAGS-85 alloy has high potential for thermoelectric generators owing to its high mechanical strength and stability. A large *ZT* of 1.8 was reached at 773 K for TAGS-80,[56] and about 1.5 was achieved at 730 K for Dy-doped TAGS-85.[57] TAGS-85 has been applied successfully in several space missions, including the Pioneer 10 and Pioneer 11 spacecraft, and the Viking Landers 1 and 2, and in SENTINEL generators for terrestrial applications.[58]

The XYZ half-Heusler compounds, where X is an electropositive element, e.g. Ti, Zr, or Hf, Y is a later transition metal, e.g. Co or Ni, and Z is a main group element, e.g. Sn or Sb, have attracted considerable interest as potential thermoelectrics above 700 K. The half-Heusler structure consists of a face-centered cubic lattice of the Z element, in which the X metals occupy all octahedral sites and the Y transition metals fill half of the tetrahedral sites. Nowadays, the thermoelectric research mainly focuses on two half-Heusler systems, i.e. TiNiSn for *n*-type and TiCoSb for *p*-type materials. The band structure of these compounds can easily be changed using various dopants to achieve an optimum power factor. This is then combined with novel approaches for reducing thermal conductivity through enhancing phonon scattering, leading to significantly improved figure of merit.[59] A considerably large *ZT* has been reported for the Ti$_{0.5}$(Zr$_{0.5}$Hf$_{0.5}$)$_{0.5}$NiSn$_{0.998}$Sb$_{0.002}$ compound, reaching 1.5 at 700 K,[60] while a sufficiently high *ZT* of 0.8 at 973 K has also been achieved for the *p*-type Zr$_{0.5}$Hf$_{0.5}$CoSb$_{0.8}$Sn$_{0.2}$ material.[61]

1.6 Magnesium Silicide Based Thermoelectric Materials

Magnesium as an alkaline earth metal can form Mg$_2$*E* antifluorite structure with the elements of group 14 (*E* = C, Si, Ge, Sn, Pb). The unit cell of these compounds is formed

through Mg atoms occupying eight tetrahedral positions located at (¼, ¼, ¼) in a face centered cubic (FCC) lattice constructed by group 14 elements (Figure 1.4).[62] Since Mg_2C is thermodynamically stable only at high pressure (more than 15 GPa) and proven to be mainly ionic,[63] and Mg_2Pb is a semimetal with an indirect band gap of -0.15 eV,[62,64] our main focus in this chapter is on the $Mg_2(Si, Ge, Sn)$ compounds and their solid solutions that have semiconducting character, which makes them a potential material for thermoelectric applications.
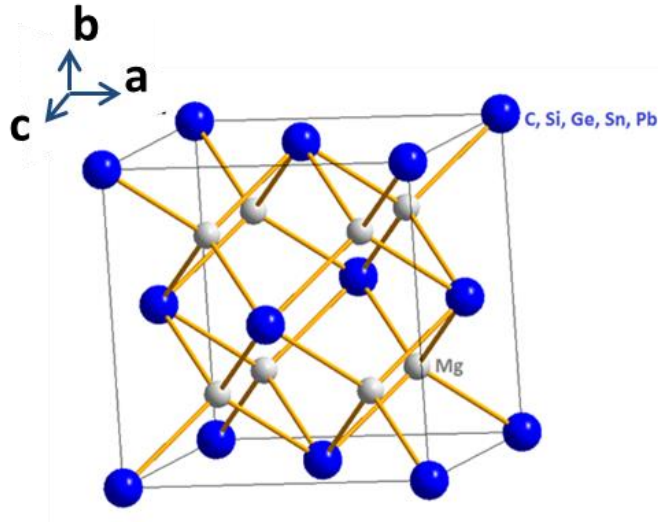
Figure 1.4   Antifluorite unit cell of Mg_2E compounds (E = C, Si, Ge, Sn, Pb).

Mg_2Si has been prepared by quite different methods such as liquid encapsulated vertical gradient freezing,[65] combustion synthesis,[66] ball milling,[67,68] microwave assisted synthesis,[65,69] vertical Bridgman,[70] metathesis reaction of NaSi and $MgCl_2$,[71] melt grown[72] and vacuum plasma thermal spray.[73] Although the iconicity of the bonding in Mg_2Si was believed to be high,[74] the nature of bonding is mostly covalent with up to 10% iconicity,[75] which is in good agreement with the obtained results from X-ray photoelectron spectroscopy (XPS) measurements. To better visualize the directions in the band structure plot, the Brillouin zone of the face-centered cubic (FCC) lattice is shown in Figure 1.4.
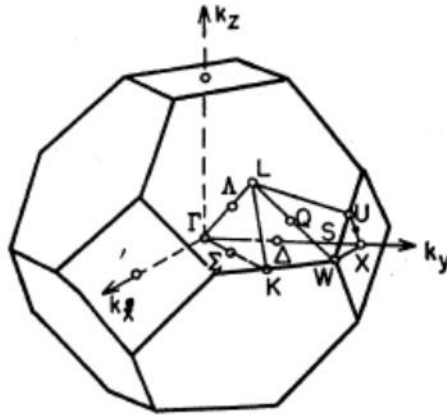
Figure 1.5   Brillouin zone of FCC lattice[†].[76]

The band structure of Mg_2Si is shown in Figure 1.5; the chosen pathway for calculation was $L{\rightarrow}\Gamma{\rightarrow}X{\rightarrow}W{\rightarrow}K{\rightarrow}\Gamma$. From the simple band diagram point of view it can be considered that the four s electrons of two Mg atoms together with the four s and p electrons of the group 14 atom would provide the eight electrons per formula unit that fill the valence band.[76] Before discussing the character of bonding in Mg_2Si, our main region to focus on is the top of valence band that starts as $L_3^|$ and finishes as Γ_{15}, and the bottom of conduction band that would be from L_1 to Γ_1. The calculated energy gap is around 1.3 eV, which is higher than the experimentally measured and generally accepted value of 0.77 eV.[77]
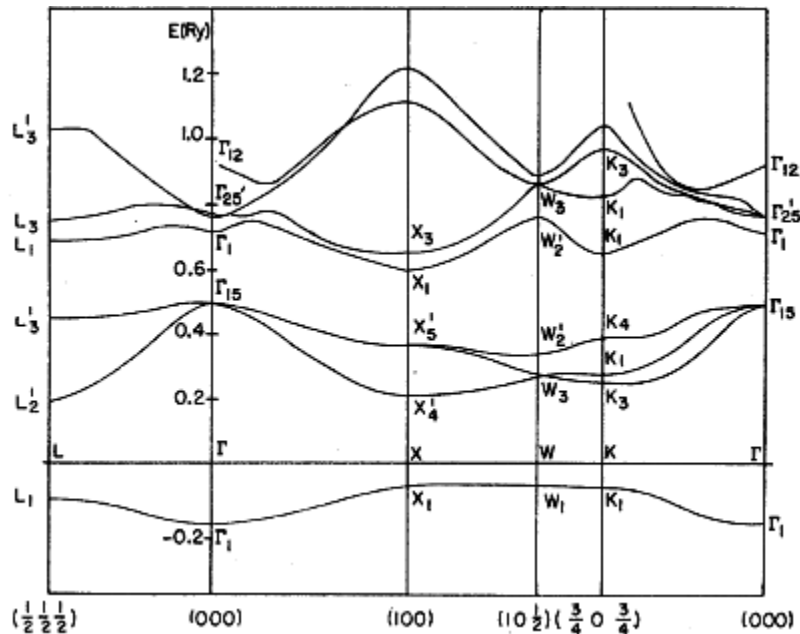
Figure 1.6   The band structure of $Mg_2Si^{\ddagger}$.[76]

In contrast to the top of the valence band that has mainly *p* bonding character, the bottom of the conduction band has *s* antibonding character. The band structure of Mg_2Ge and Mg_2Sn is nearly the same with the maximum of the valence band at the Γ point and the minimum of the conduction band at *X*. By moving down in the periodic table from Si to Ge and Sn, the indirect energy gap is reduced from 0.77 eV to 0.74 eV and 0.36 eV, respectively.[77] The reduction in the energy gap is related to the filling of higher energy (level) *p* orbitals of Ge and Sn which form the top of valence band. Since the electronegativity of Si (1.90 on the Pauling scale) is close to Ge (2.01) and Sn (1.96), no major difference is expected in the covalent character of the bonding. Although the covalency of the bonds does not get affected that much, increasing the atomic radius of the group 14 element increases the unit cell. This reduces the overall orbital overlap and the bond strength, which leads to a dramatic decrease in the melting point of Mg_2(Sn, Pb) compared

with $Mg_2(Si, Ge)$ (Table 1.1). The change in the band structure of Mg_2Si through substitution of Si with Ge/Sn will be discussed later in the solid solution section of this chapter.

Table 1.1   Lattice parameter and melting points of Mg_2E (E= Si, Ge, Sn, Pb).

Compound	Unit cell parameter (Å)	Melting point (°C)
Mg_2Si	6.338[78]	1102[64]
Mg_2Ge	6.385[79]	1115[64]
Mg_2Sn	6.770[80]	778[64]
Mg_2Pb	6.907[81]	550[64]

1.6.1 Nature of intrinsic defects in Mg_2(Si, Ge, Sn) compounds

In general point defects in Mg_2(Si, Ge, Sn) compounds can be divided into intrinsic and extrinsic defects. In this section, our main focus is on the nature of intrinsic defects in Mg_2E semiconductors under stoichiometric, Mg rich and Mg poor conditions. The possibilities for the type of point defects are as follows:[82]

- Occupying Interstitial (I) sites (e.g. Mg^I,…)

- Mono/multi vacancy (V) of certain sites (e.g. V^{Si}, V^{MgSi},…)

- Antisite defects e.g. Mg atom occupying Si position (Mg^{Si},…)

The undoped Mg_2Si is intrinsically *n*-type. First principles[83] and ab initio[84] studies showed the favorable defect in stoichiometric and Mg rich Mg_2Si is Mg occupying the interstitial site (Mg^I), which also acts as an electron donor state. This agrees well with the experimental results.[85] In Mg poor condition, Kato *et al.* showed the Mg^I is still the major defect but with lower concentration. This could be the reason why undoped Mg_2Si never shows *p*-type character. Other calculations for Mg poor condition[82,84] showed higher stability in terms of formation energy for V^{Si}, V^{MgSi} and Si^{Mg}. From the empirical point of view,

16

silicon vacancy could compensate for the lack of Mg to stabilize the structure, but antisite Si in Mg position might not be practical with respect to the larger radius of Si^{4-} compared to Mg^{2+}. In contrast to Mg_2Si, the synthesis of pure Mg_2Ge single crystals[86] revealed that in stoichiometric condition, V^{Mg} is energetically favorable to other types of defect that could also be due to Mg loss stimulated by high synthesis temperature. The addition of excess Mg during the synthesis governs the change from Mg poor to Mg rich condition. Then, the Mg^I defect dominates, and as a result the material would demonstrate a transition from *p*-type to *n*-type;[86] the obtained experimental results are in good agreement with the predictions from first principles calculation. Electronic structure calculations[87] on Mg_2Sn both in Mg rich and Sn rich limits suggested V^{Mg} as a favorable defect, which could be one of the reasons for the undoped Mg_2Sn[88,89] to exhibit the observed *p*-type behavior. First principles calculation by Viennois *et al.* also found the V^{Mg} more favorable than Sn^{Mg} and Mg^I. This could be due to the fact that Sn^{4-} could not easily occupy the Mg^{2+} position due to the size difference and the larger size of the interstitial site compared to Mg_2Si could destabilize the Mg^I.

1.6.2 Thermoelectric properties of Mg_2E (E = Si, Ge, Sn, Pb) and their solid solutions

As discussed in the last section, magnesium silicide itself is a very poor electrical conductor due to its fairly wide indirect bandgap. One of the most promising ways to enhance the conductivity of a semiconductor is through introducing extrinsic point defects or so called "doping". Depending on the chemical properties, structure and bonding nature of the host material the dopant can be chosen to either add or remove an electron to provide the desired type of conductivity. Up to this point, scandium (Sc),[90] yttrium (Y),[90] cobalt (Co),[69,91,92] copper (Cu),[93] zinc (Zn),[94] lanthanum (La),[95,96] boron (B),[97] aluminum (Al),[93,98–103] phosphorus (P),[104] antimony (Sb),[92,96,98,100,105–126] bismuth (Bi),[93,103,112,116,127–142] selenium (Se),[143] and tellurium (Te)[143,144] were examined as *n*-type doping and sodium (Na),[145] potassium (K),[146] lithium (Li),[146–150] silver (Ag),[133,150–152] and gallium (Ga)[153,154] were used to generate *p*-type conduction. Calcium (Ca),[155] germanium (Ge),[72,97,112,114,140,156–158] tin (Sn)[102,108,111,113,123–126,129,131,135,136,138,140,141,150,159–181] and lead (Pb)[182] were also used as a substitution for making the solid solution to tune the band structure of Mg_2Si. Except for Ca all other isoelectronic substitution atoms occupy the Si position. Due to the small size of

Mg^{2+}, the structure is less flexible to accept larger ions such as Ca^{2+}. This can be observed from the extra side phase peaks in the $Mg_{2-x}Ca_xSi$ material.[155] Based on the fact that not all the Ca went into the structure, the effect of Ca on the reduction of thermal conductivity is negligible.

One of the advantages of Mg_2Si is that it can form a wide range of solid solution with Ge and Sn, because all the $Mg_2(Si,Ge,Sn)$ form an antifluorite structure. In the case of Ge, the whole range of solid solution can form, but for Sn it was long believed that there is a miscibility gap (Figure 1.7) from $Mg_2Si_{0.4}Sn_{0.6}$ to $Mg_2Si_{0.6}Sn_{0.4}$.[183] Chen *et al.* observed a shift to lower Si content based on their synthesis method.[184]
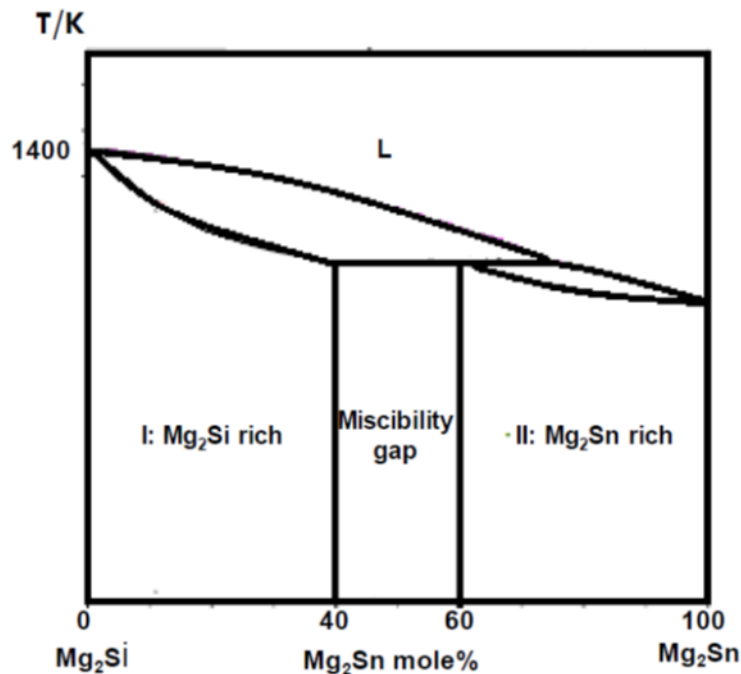
Figure 1.7   Miscibility gap in $Mg_2Si_{1-x}Sn_x$ solid solution (adopted from[95]).

By shifting the miscibility gap depending on the synthesis method, one can deduce that the gap mainly stems from a kinetic barrier rather than the thermodynamic one. Applying the proper synthesis methods[121,185] could effectively overcome this barrier to be

able to synthesize the compositions that are supposed to be in the miscibility range. Up until now, solid solution is one of the most potent ways in reducing the thermal conductivity of Mg_2Si. Introducing the distortion in the lattice by heavier and larger elements such as Sn can generate the anharmonicity that is responsible for disorder scattering of acoustic phonons, which are majorly responsible for carrying the heat.[186] The lattice thermal conductivity of a disordered alloy (solid solution) is usually in the shape of a deformed parabola, such as in this case (Figure 1.8).
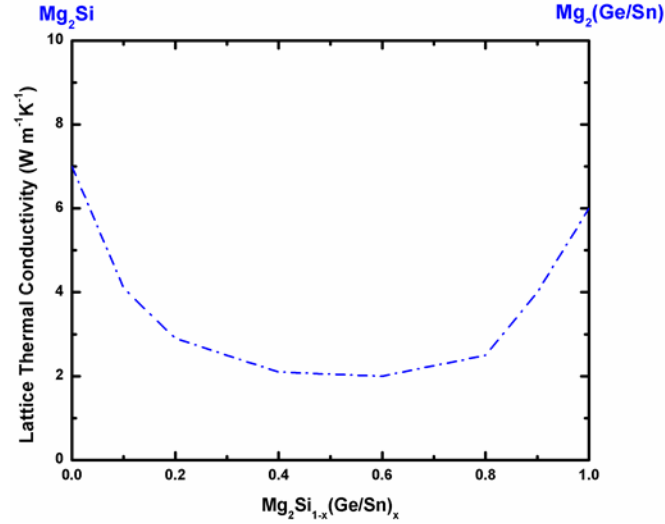
Figure 1.8   Room temperature lattice thermal conductivity of $Mg_2Si_{1-x}(Ge/Sn)_x$ solid solution.

Another pivotal role of adding Sn into the structure is the ability to tune the band structure. The conduction band minimum (CBM) around the Γ point, in $Mg_2Si_{1-x}Sn_x$ consists of both a heavy (H_{CB}, red) and a light (L_{CB}, blue) band. At a certain Sn level (x = 0.625-0.7)[187,188] these two bands overlap (Figure 1.9), which then simultaneously causes an equalization of the Si and Sn character of the CBM and the effective mass of the band to reach its maximum value, as a consequence the sample exhibit a large S.[187] Furthermore, the

19

induced lattice distortion due to the Si/Sn ratio causes the lowest lattice thermal conductivity among other compositions.[187]
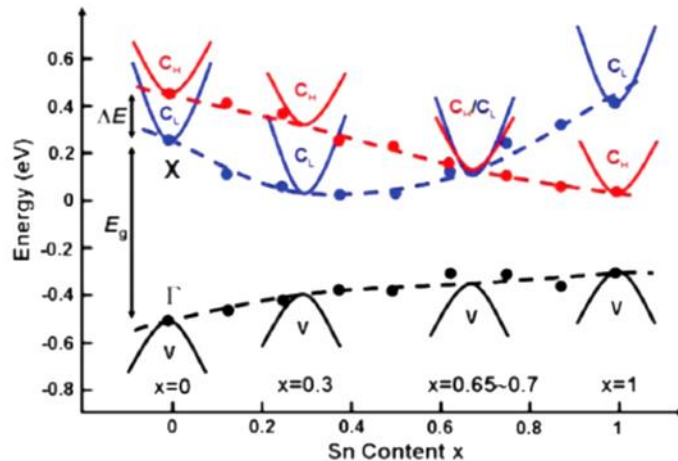
Figure 1.9   Band overlap in $Mg_2Si_{1-x}Sn_x$ solid solution[§].[188]

p-type dopants can be categorized into two groups. The first group includes the elements substituting Mg which are Na, K, Li, Ag; and the second group consists of the only element substituting Si, namely Ga. Among the elements substituting Mg, Li shows the highest p-type electrical conductivity of around 1100 $\Omega^{-1}cm^{-1}$.[146] Comparing the crystal radius of the cations in tetrahedral coordination, one notices that Li^+ (0.73 Å) in contrast to Na^+ (1.13 Å), K^+ (1.51 Å) and Ag^+ (1.16 Å), has the closest value to Mg^{2+}(0.71 Å).[189] The same argument is also valid when considering the covalent radius of these elements.[190] Replacing Mg with larger elements could promote occupying the octahedral position by Mg or the dopant, which can eventually decrease the hole concentration through generating a donor state. The calculation on Ag doping showed that the structure would energetically be more favorable to generate interstitial Mg,[151] which could be the reason for lower conductivity and carrier concentration of Ag-doped Mg_2Si based materials.[93,150] A band

structure calculation showed introducing Ga into Mg_2Si would move the Fermi level close to the valence band edge which is in agreement with the observed *p*-type character of Ga containing Mg_2Si and $Mg_2Si_{1-x}Ge_x$.[153] The first principles calculation[191] indicated that Ga has the lower formation energy for occupying the Si position than the Mg position, despite having crystal radius of 0.61 Å as Ga^{3+}, which is close to Mg^{2+}. Liu *et al.* also observed the formation of Mg_5Ga_2 upon increasing the Ga concentration.[154] All in all, the hole concentration was improved up to ~ 4.9×10^{20} cm^{-3} for the Li doped sample.[146] The drawback of doping with Li is the instability of the samples at high temperature which originates from the movement of Li ions possibly through vacant octahedral holes.

Unquestionably, among all the *n*-type dopants, Sb and Bi were the most successful ones in increasing carrier concentration, thereby improving the electrical conductivity of the Mg_2Si based materials. One of the main issues that most of the high performance *n*-type variants have in common,[107,113,135,165,192–195] is the existence of MgO as a side phase in an amount that is detectable by powder X-ray diffraction, PXRD. Even though the small concentration of MgO at the grain boundaries might increase boundary scattering[196] to reduce thermal conductivity, MgO due to its high thermal conductivity (~ 30 W $m^{-1}K^{-1}$ at 400 K) [197] and low electrical conductivity could attenuate the performance of the material through decreasing the mobility and thereby electrical conductivity.[198]

Along with doping, incorporating extra Mg seemed to be a reliable strategy to increase the carrier concentration of $Mg_2Si_{1-x}Sn_x$ solid solutions.[113,173,193,194,199–201] In some cases, the extra Mg that occupies the interstitial sites could also reduce the lattice thermal conductivity especially at high temperature by means of point defect scattering.[113,173,199] In the $Mg_2Si_{1-x-y}Ge_xSn_y$ system, Ge rich inclusion regions were found that can alleviate the thermal conductivity and improve *ZT* up to 1.3 at 773 K for both Sb and Bi doped materials [135,195]. The other constructive effect of Ge in higher concentration is to broaden the energy gap to restrain the bipolar contribution that can reduce the high temperature figure of merit.[202]

Recently Ning *et al.* reported the maximum *ZT* value of 1.63 at 615 K for an Sb doped $Mg_2Si_{0.5}Sn_{0.5}$ sample made by pressure-less spark plasma sintering (SPS). Since the enhancement of *ZT* was made through porosity, and the best sample has a relative density of only 63%, there are a couple of issues that need to be considered for any application. Porosity not only reduces thermal and electrical conductivity but also decreases the mechanical strength of the sample, which is very important from the engineering point of view. Applying the heating cycles on the porous sample can change the porosity hence changing the properties of the sample. After all, no result was shown regarding the reproducibility of the samples, which can be due to the challenging process of achieving the exact same porosity for the sample. Despite showing *ZT* of 1.63 at 615 K, a drastic reduction in *ZT* due to bipolar effect led to a *ZT* of 0.84 at 770 K. This led to an average *ZT* ~ 1.[203]

1.7 Alkaline Earth Silicides for Thermoelectric Application

Undoubtedly, magnesium silicide is the best studied compound in alkaline earth silicide system. All the elements in the group 2 except radium (Ra), which is significantly radioactive and carcinogenic, can be considered for thermoelectric applications. Starting from the top of the group, beryllium (Be) cannot form a single phase binary silicide with silicon ,and the solid below 1373 K consists of two separate phases, α Be and Si.[204]

Calcium (Ca) could form Ca_2Si, Ca_5Si_3, $CaSi$, Ca_3Si_4 and $CaSi_2$ as binary silicides,[205] which all are thermodynamically stable compounds.[206] $CaSi_2$ that can be synthesized through a peritectic reaction at 1303 K demonstrated a decent stability to moisture, which makes it easier to handle for thermoelectric measurements. Under high pressure (15 GPa) $CaSi_2$ would go through a phase transformation that showed the low temperature superconducting transition at 14 K. Ca_2Si (Figure 1.10a) with a congruent melting point of 1543 K was estimated to have a direct band gap between 0.3 eV to 0.362 eV.[206–209] Thermoelectric properties of Ca_2Si showed a *p*-type semiconducting character with a room temperature conductivity of around 0.018 $\Omega^{-1}cm^{-1}$ and carrier concentration of 3.1×10^{16} per cm^3.[210] The sodium (Na) addition seemed to act as an acceptor and improved the *p*-type conductivity by

increasing the carrier concentration to around 1.3×10^{18} per cm^3. The positive characters of Ca$_2$Si from thermoelectric point of view are its low room temperature thermal conductivity of 2.31 W m^{-1}K^{-1} and high Seebeck coefficient (S) of ~ 200 μV K^{-1}.[210] It is worth to mention that all the measured samples of Ca$_2$Si had a relative density below 90%, which could significantly affect their transport properties. Ca$_3$Si$_4$ with a decomposition temperature of 1183 K can also be a good candidate for medium temperature range thermoelectrics. The ab initio[211] and first principles[212] calculation revealed a semiconducting character of this compound with an indirect band gap ranging from 0.35 eV to 0.598 eV.[206,212] Due to the comparable indirect gap of Ca$_3$Si$_4$ to Mg$_2$Si, it could be worthwhile to investigate the effect of doping on its thermoelectric properties. CaSi that has CrB type structure possessed a metallic behavior with a high electrical conductivity (σ) of around 4000 Ω^{-1}cm^{-1} at 323 K.[213] The disadvantage of CaSi for thermoelectric application is its high room temperature thermal conductivity (κ) (~10 W m^{-1}K^{-1}). Although Ca$_5$Si$_3$ (Figure 1.10b) has almost zero band gap with a pseudogap of 0.1 eV, it showed more promising thermoelectric behavior than CaSi. The higher room temperature Seebeck coefficient of 40 μV K^{-1} with nearly half the thermal conductivity value (~5 W m^{-1}K^{-1}) of CaSi, makes the Ca$_5$Si$_3$ one of the potential *p*-type materials that can be investigated for thermoelectric applications up to 1000 K.[213,214]
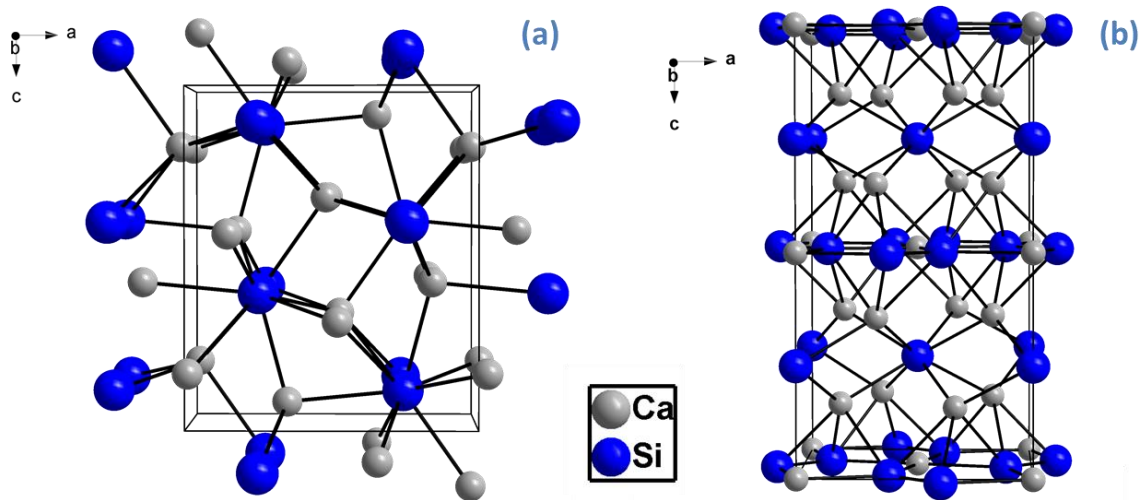
Figure 1.10 (a) Crystal structure of Ca_2Si (anti-$PbCl_2$ type structure, with tricapped trigonal prismatic Ca coordination for every Si atom) (b) Ca_5Si_3 (Cr_5B_3 type structure, with $[Si^{4-}]$ monomers and $[Si-Si]^{6-}$ dimers in alternative layers along c axis)

Like Ca, strontium (Sr) forms a variety of silicides ranging from Sr_2Si to $SrSi_2$.[215] In spite of the fact that Sr_2Si has a decomposition temperature higher than 1273 K and first principles calculation[216–218] predicted a direct band gap of around 0.4 eV, no thermoelectric property measurements were carried out on this compound to date. Pure SrSi and Sr_5Si_3 could not be considered as good thermoelectric materials due to their nearly metallic character.[219] $SrSi_2$ with a congruent melting point of 1393 K and a narrow band gap of 0.035 eV [220] is the most studied compound in the Sr-Si system. The structure has a low temperature cubic α phase and a high temperature tetragonal β phase; the phase transformation from β to α was reported to be between 673 K and 963 K.[215] The cubic α phase has the space group of $P4_332$ with Sr occupying the (1/8, 1/8, 1/8) position (Figure 1.11). The Si–Si distance is ~ 2.40 Å, and the Sr–Si distance is ~ 3.25 Å. Each Si atom is connected with three other Si atoms with a threefold symmetry in the structure.[221] Although most of thermoelectric properties of $SrSi_2$ based materials were measured up to 300 K, no unusual behavior was detected on the high temperature data that can be attributed to the phase transformation.

Undoped $SrSi_2$ demonstrated a decent room temperature figure of merit (*ZT*) value of 0.1, unfortunately increasing the temperature from 300 K to 1000 K would decrease the Seebeck coefficient from 125 μV K^{-1} to around 60 μV K^{-1} without affecting its high thermal conductivity (~5 W $m^{-1}K^{-1}$), causing a reduction in *ZT* at higher temperatures.[222] So far the effect of aluminum (Al),[223] Ge,[224] yttrium (Y),[225] Ca and barium (Ba),[226] on the low temperature thermoelectric properties of $SrSi_2$ were investigated. The addition of Al seemed to consistently increase the electrical conductivity and decrease the Seebeck coefficient without notably reducing the thermal conductivity, since the material has already exhibit low *S* this strategy could not be effective in improving the TE properties. Substituting the heavier isoelectronic elements such as Ge and Ba resulted in reducing the thermal conductivity without considerably affecting the thermopower which could be due to mass fluctuation effect; Ca despite being isoelectronic was shown to improve both electrical conductivity and Seebeck coefficient. One of the best TE properties at 300 K belong to Y doped $SrSi_2$ with the *ZT* value of 0.4, which therefore should be investigated for high temperature applications. Another possibility is to study the effect of simultaneously adding Y and tin (Sn) or Ge on the TE properties of $SrSi_2$.
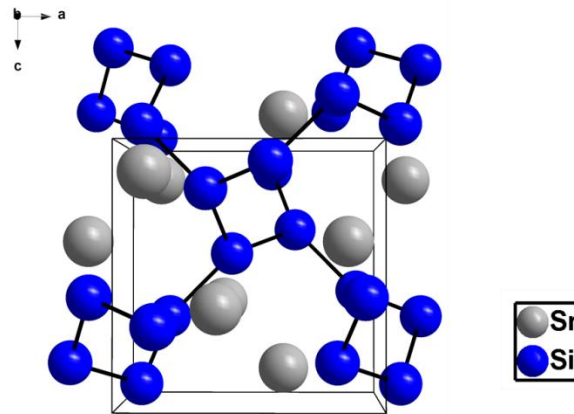
Figure 1.11   Crystal structure of cubic $SrSi_2$ with each Si connected to three nearby Si.

Although barium (Ba) forms various stable binary silicides[227] like Ca and Sr, only the thermoelectric properties of $BaSi_2$ were studied so far. $BaSi_2$ with the energy gap of 0.8 eV [228,229] possessed a large S of -700 $\mu V K^{-1}$ at 323 K, which is not desirable for TE application. Even the addition of lanthanum (La) could not decrease S, possibly because of the formation of side products such as $LaSi_2$.[230] $BaSi$, Ba_5Si_3 and Ba_3Si_4 all are metallic,[231] and Ba_2Si has a fairly large band gap that would not be suitable for TE application.

1.8 Future Thermoelectric Materials

BiCuSeO oxyselenides are new promising thermoelectric materials in the middle temperature range owing to their extremely low thermal conductivity, which is less than 0.7 W $m^{-1}K^{-1}$ at room temperature. BiCuSeO crystallizes in the ZrCuSiAs structure type containing fluorite like Bi_2O_2 layers stacking alternatively with Cu_2Se_2 layers along the c-axis. The Cu_2Se_2 layer is the reverse version of the Bi_2O_2 one, where the Cu and Se positions are the same as those of the O and Bi atoms, respectively. All the derivatives of BiCuSeO, where Bi is substituted by Sr, Cu by Fe, Se by Te, and O by F, revealed the p-type conducting mechanism.[232]

The natural minerals of the tetrahedrite ($Cu_{12-x}M_xSb_4S_{13}$) and tennantite ($Cu_{12-x}M_xAs_4S_{13}$) systems, where M is a transition metal, are potential candidates for thermoelectric applications due to their intrinsically low lattice thermal conductivity. These materials possess a cubic sphalerite-like structure, where the metal atoms substitute at the Cu sites. This mineral family is the most widespread sulfosalt on Earth, which is the main source of copper and silver worldwide. All the Zn-substituted compounds have a lattice thermal conductivity less than 0.5 W $m^{-1}K^{-1}$, which is close to the theoretical limit owing to their highly anharmonic behavior of phonon scattering. The maximum ZT approaching 1.0 at 720 K to date was achieved for the $Cu_{11.5}Zn_{0.5}Sb_4S_{13}$ compound.[233]

Chapter 2
Experimental procedures

2.1 Introduction

In this chapter, the synthesis techniques and characterization methods used for TE materials are described. Since experimental synthesis and characterizations are the major parts of thermoelectric research, it is important to not only understand the basic principles behind the techniques but also to aware of the errors associated with each them. Also, the experimental precautions will be pointed out to assure the quality of the obtained data.

2.2 Reaction synthesis

Solid state and solid liquid mix reactions are among the most common ways to synthesize bulk TE materials. In a solid state reaction solid reactants would come into contact with each other and create interfaces; then the product will form at the interface through the reaction between reactants (Figure 2.1a). The reaction rate is directly proportional to the nucleation rate and the completion of the reaction depends on how fast the ions in the reactants can diffuse inside the interface. The diffusion rate strongly relies on the temperature and diffusion path length. Since at low temperature ions/atoms in the solid have low tendency to move, most of solid state synthesis happen at fairly high temperature. Increasing the temperature would increase the probability of generating defects that ease the ion movement. To expedite a solid state reaction, it is important not only to increase the reaction rate but also to decrease the diffusion length. One of the suitable ways to shorten the diffusion length is through mixing and grinding the samples to form fine powder before heat treatment. In some cases, to achieve the highest purity and homogeneity, it is necessary to grind the product after the heat treatment and reheat it in a step that is often referred to as "annealing". Another way to obtain the desired product in a shorter time is by melting one of the reactants to have a solid liquid mixture (Figure 2.1b).[234]
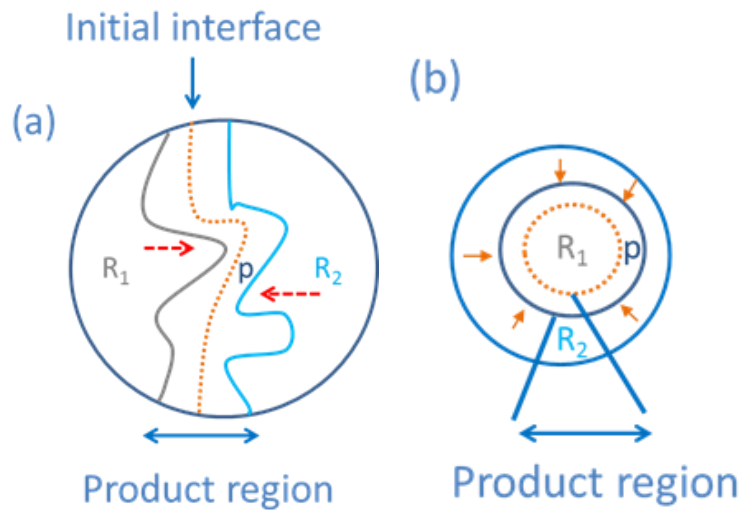
Figure 2.1   (a) Formation of product (P) at the interface of solid reactants R_1 and R_2; (b) solid reactant R_1 and liquid reactant R_2.[234]

Advantages of having a liquid phase in the mixture are both producing more interfaces (more active surfaces) and facilitating the ion movement (faster diffusion), both of which can dramatically reduce the reaction time. Another important factor that can affect the formation of the product is the reaction container (crucible). Depending on the temperature and chemical nature of the elements, various types of crucibles can be used for the synthesis. Some reactions can happen in a fused silica (Figure 2.2a) or carbon coated fused silica tube (Figure 2.2b) without any crucible, but others need crucibles such as graphite crucibles (Figure 2.2c), alumina crucibles (Figure 2.2d) or tantalum crucibles (Figure 2.2e).
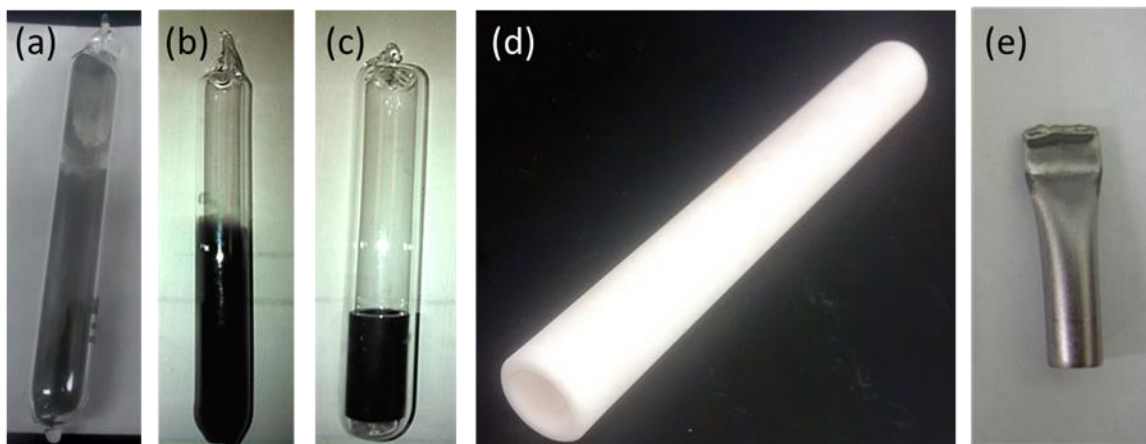
Figure 2.2   (a) sealed silica tube; (b) with graphite coating; and (c) graphite crucible; (d) unsealed alumina and (e) tantalum crucible.

An advantage of using a Ta crucible is not only that it can withstand high temperature, but also it can be sealed through an arc melting process, which is very crucial for the reactions containing volatile elements such as magnesium. Arc melting is a technique using a high voltage arc generated by applying a high current (from 30 A to 150 A) passing through a tungsten electrode to heat up the specimen to a very high temperature (e.g., 3000°C, depending on the applied current) in couple of seconds (Figure 2.3).

Figure 2.3   Homemade arc melting setup**.**

The usage of powders is not recommended for an arc melting experiment because the sparkling powders can cover the whole reaction chamber causing the loss of stoichiometric compositions, and the risk of oxidation is high due to large surface areas. The mixture of powders can be cold-pressed into pellets placed in a copper sample holder cooled down by circulating cooling water to prevent an overheating of the specimens. The process is carried out under a continuous argon flow. Due to the high vapor pressure of Mg it is not possible to apply these procedures to the samples containing Mg. So all the elements need to be placed in the Ta crucible first in an oxygen free environment that can be achieved in an argon filled glove box (Figure 2.4), and then the closed crucible can be transferred into the arc melter for sealing. A zirconium ingot is commonly arc melted before the actual sample to remove any remaining oxygen in the system.

Figure 2.4   Ar atmosphere glove box with oxygen and moisture level of less than 2 ppm.

After the Ta tube is sealed, the crucible is put into the silica tube (Figure 2.2a), and the silica tube is evacuated through connecting to the vacuum line (Figure 2.5a) until the tube reaches a pressure below 2.5×10^{-3} mbar. The evacuated tube will then be fused by using O_2/H_2 torch (Figure 2.5b).
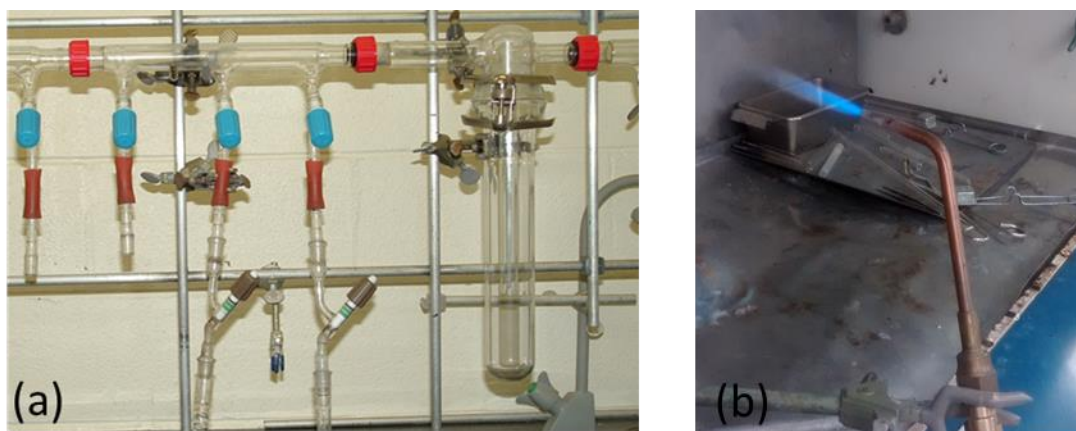
Figure 2.5   (a) Vacuum line and (b) O_2/H_2 flame torch.

At this stage the fused tube is ready for the heat treatment, which can be done by means of resistance furnaces. Based on the complexity of the heating profile, manual (Figure 2.6a) or programmable furnaces (Figure 2.6b) can be used to assure the completion of the reaction.
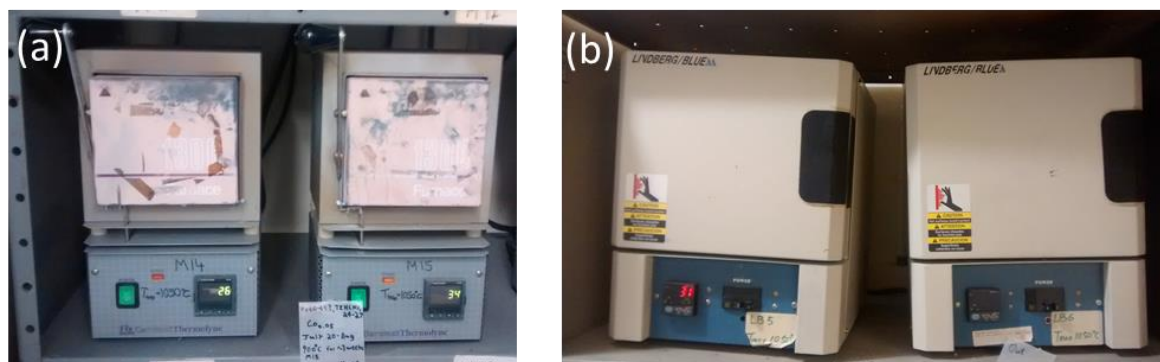
Figure 2.6   (a) Manual and (b) programmable resistance heating furnaces.

After the heat treatment, the product is ground to powder and the phase purity of the powder checked by powder X-ray diffraction analysis.

2.3 Powder X-ray diffraction analysis (P-XRD)

P-XRD is a characterization technique extensively utilized in material science and related fields. The here used P-XRD apparatus is an INEL powder diffractometer with a position-sensitive detector using Cu Kα1 radiation (λ = 1.540598 Å) (Figure 2.7). The X-rays are created through the bombardment of the Cu anode with high speed electrons. Tungsten filament is used as the electron source; by heating the filament, electrons will be emitted. Trough applying a high voltage (30 kV), the accelerated electrons collide with anode and emit a broad energy spectrum of X-ray radiation (Bremsstrahlung) as a result of energy loss. In addition to that, high energy electrons can knock out an electron from the inner shell of the bombarded material (Cu) to generate a vacancy, which then will be filled by an electron from the outer shell. To conserve the energy, an X-ray will be emitted as a consequence of this process that has the energy equal to the energy difference of inner and outer electron shells. The wavelength of generated X-ray is thus unique for each material. Since the temperature of the anode will increase because of the partial energy loss that manifests itself as waste heat, the anode is continuously cooled down by cooling water. To obtain monochromatic and focused beams, X-rays go through a Ge single crystal and a collimator before interacting with the powders.[235,236]
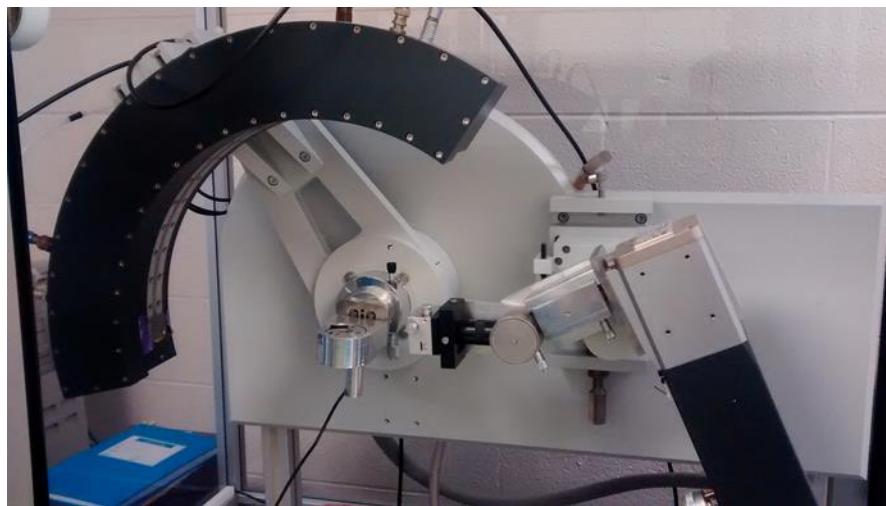
Figure 2.7 INEL powder diffractometer with a position-sensitive detector.

X-rays can interact both constructively and destructively with the electrons of the atoms. According to Bragg's law (Equation 2.1), if the difference in the path length of two diffracted rays equals to an integer multiplication of the wavelength (Figure 2.8), the interaction is constructive and a diffraction peak can be observed.

$$n\lambda = 2d\,sin\theta$$ Equation 2.1
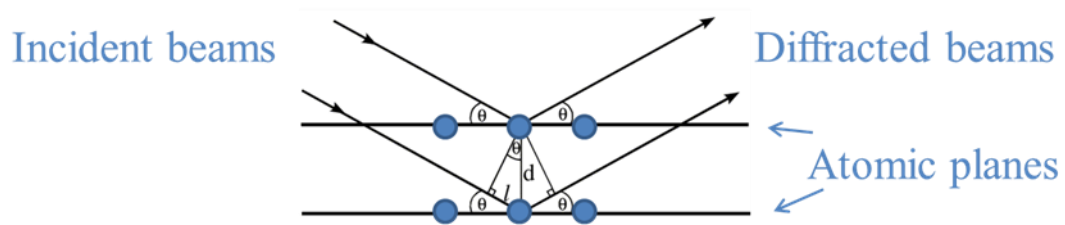
Figure 2.8   Bragg's condition for constructive interference.

Another important parameter that can be obtained from powder diffraction pattern is the crystallite size which is more accurate for the samples with crystallite size less than 200 nm. According to the Scherrer equation(Equation 2.2),[237] the peak width (B) is inversely proportional to the size of crystallite (l) at the peak angle (θ).

$$B = K\lambda\,(cos\theta)^{-1}$$ Equation 2.2

In the above equation K is referred to as proportionality (Scherrer) constant and can vary from 0.62 to 2.08,[237] but for spherical crystals with cubic symmetry it is approximately 1. It is important to mention that the peak width must be in radian and is the full width at half maximum (FWHM). λ is the wavelength of the X-ray used to obtain the pattern. Since part of

the broadening could come from instrument and micro-strain in the sample, it is important to consider those effects while calculating the crystallite size.

2.4 Densification process

The next step after verifying the purity via P-XRD is the sintering. Sintering is the densification process by using heat/pressure of the solid state material without going to its melting point. During the sintering process particles in the powder will fuse together to achieve a high density solid form. The densification of the thermoelectric materials in this work is done by Oxy-Gon hot press instrument (Figure 2.9a). For the sintering, the ground powder was placed into a graphite die and then inserted into the instrument, where it was heated under a certain pressure (Figure 2.9b). The radiation heating of the tungsten heating element will transfer to the sample through conduction from graphite die and the sample will gradually reach the temperature close to the desired set point. Simultaneously uni-axial pressure is applied to the sample to enhance the densification process. The applied force can vary between 400 kg to 30 tons. The hot press process can be performed under vacuum, inert ultra-high pure (UHP) Ar atmosphere and Ar balanced H_2 atmosphere to eliminate unwanted oxides. The consolidated sample after pressing is in the form of a cylindrical pellet with 12.7 mm in diameter.
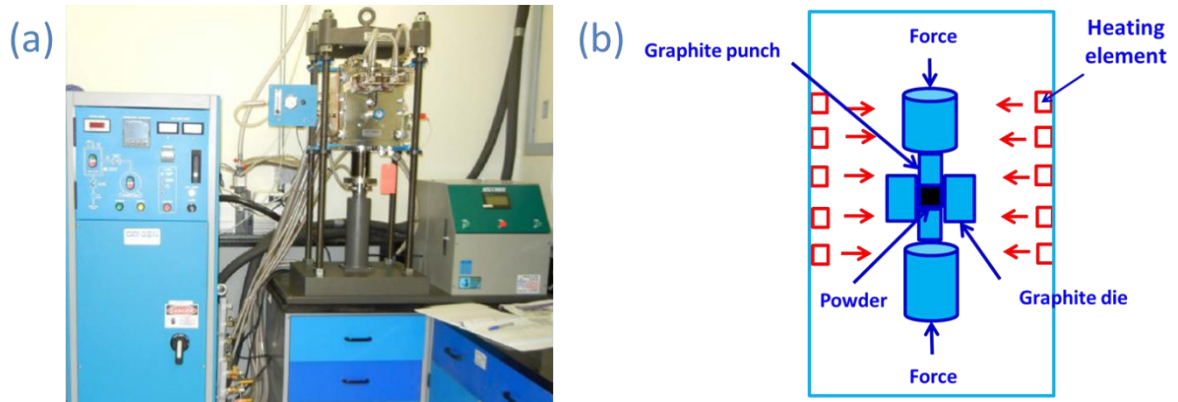
Figure 2.9   (a) Hot pressing Oxy-Gon instrument; (b) Schematic representation of operation.

2.5 Archimedes' density measurement

The Archimedean principle is used to determine the specific gravity of a solid immersed in a liquid. The Sartorius YDK01 density determination kit is commonly used for the solid with its specific gravity higher than that of the reference liquid. The buoyant force acting on the solid is proportional to the weight of the liquid displaced by the volume of the solid. The density of the solid, d_{solid}, can be calculated from the weight of the solid in air and liquid, m_{air} and m_{liquid}, respectively, measured by a hydrostatic balance, and the density of the liquid causing buoyancy, d_{liquid} (Equation 2.3).

$$d_{solid} = \frac{m_{air} \times d_{liquid}}{m_{air} - m_{liquid}}$$ Equation 2.3

This formula is sufficient to achieve an accuracy in the density of one percent. However, several errors and allowance factors need to be considered depending on the required accuracy, including temperature dependence of liquid density, air buoyancy, immersion level of the holder containing sample, liquid adhesion on the assembly, and air bubbles on the sample.

The temperature of the reference liquid needs to be measured carefully, and its density should be corrected accordingly. The change in the density per degree is in the range of 0.02% for distilled water, and 0.1% for alcohols and hydrocarbons. Consequently, distilled water is preferable due to its wide availability and temperature independent density, while alcohols and hydrocarbons are usually employed for the samples sensitive to water.

The density of air under standard conditions, $d_{air} = 0.0012$ g/cm^3, is included in the formula to correct the errors of air buoyancy (Equation 2.4).

$$d_{solid} = \frac{m_{air} \times (d_{liquid} - d_{air})}{m_{air} - m_{liquid}} + d_{air} \qquad \text{Equation 2.4}$$

The wires of the sample holder or sieve are submerged deeper when the sample is in the sample holder. Therefore, a correction factor of 0.99983 for the errors from changing the immersion depth of the assembly is determined exclusively from the geometry of the measuring device setup (Equation 2.5).

$$d_{solid} = \frac{m_{air} \times (d_{liquid} - 0.0012)}{0.99983 \times (m_{air} - m_{liquid})} + d_{air} \qquad \text{Equation 2.5}$$

In order to eliminate the errors of liquid adhesion, the balance is unloaded at the beginning of each measuring step to disregard the effect of the meniscus, and the weight is read off immediately after the stability symbol is displayed. To reduce the surface tension and liquid friction, some surfactants can be added to the reference liquid. Large air bubbles on the sample must be removed with a fine brush or other utensils, and the sample can be wetted in a separate container before weighing.

2.6 Laser flash thermal diffusivity measurement

The first measurement after sintering is thermal diffusivity measurement. This experiment is carried out by Anter Flashline 3000 apparatus (Figure 2.10a) under inert Ar flow to avoid any oxide formation. During the measurement the pellet will be exposed to intense short pulse xenon flash light (Figure 2.10b) from the bottom side. The heat will then dissipate through the conduction process inside the pellet and reach the top surface. The temperature increase at the top surface is detected by an InSb infra-red (IR) detector.[238–240]

As can be seen in Equation 2.6, the diffusivity (α) is related to sample thickness (l) and the time that the top surface needs to gain half of the maximum temperature rise ($t_{0.5}$). The exact value of α can be obtained by using the desired proportionality constant (c), based on the type of heat loss. As an example the value of c assuming no heat loss (Parker model[241]) is equal to 0.139.

$$\alpha = c \times l^2 \times t_{0.5}^{-1}$$

Equation 2.6

It is important to have a pellet with the uniform thickness of ≤ 2 mm for the measurement. To increase the uniform heat absorption and to prevent reflection, both top and bottom surfaces are coated with graphite prior to the measurement. For calculating the thermal conductivity (κ), the density (d) of the pellets is measured via the Archimedes method, and the Dulong-Petit approximation is applied for determining specific heat (C_P) values. In selected cases, C_P was also experimentally determined by our collaborators at General Motors. The thermal conductivity is then calculated according to $\kappa = \alpha \, d \, C_P$. After the measurement, the pellet will be cut into a rectangular bar with an approximate size of $2 \times 2 \times 12$ mm^3 to be used for electrical resistivity and Seebeck coefficient measurements.
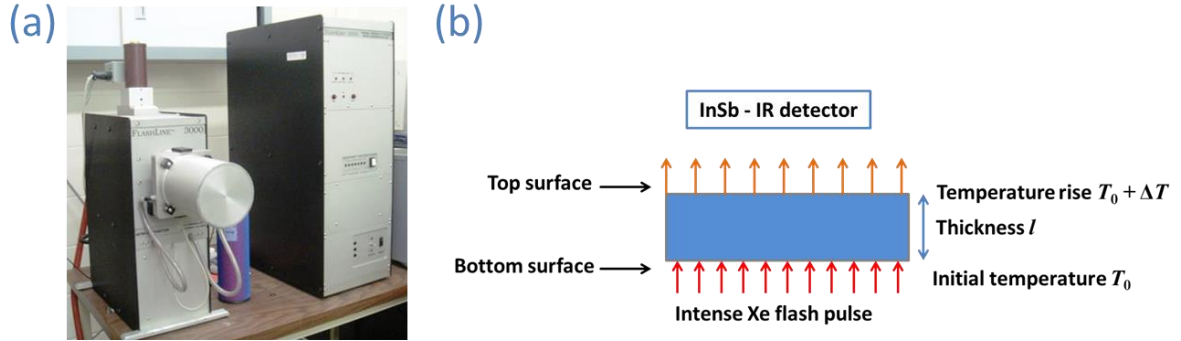
Figure 2.10   (a) Anter Flashline 3000; (b) Schematic representation of Xe flash method.

2.7 Electronic property measurements

Electrical resistivity and Seebeck coefficient of the sample is measured by ZEM 3 (ULVAC-RIKO) instrument (Figure 2.11). For this thesis, the measurements are performed under helium atmosphere between 300 K and 800 K. The sample geometry for the measurement can be either rectangular or cylindrical. Before the measurement, it is important to be sure that not only the sample facets are parallel but also the top and bottom surfaces of the sample are flat to make a good contact with the Ni electrodes.

Figure 2.11   ZEM-3 (ULVAC-RIKO) electrical resistivity and Seebeck coefficient measurements instrument.

The sample is sandwiched between two Ni electrodes and R-type lateral thermocouples come into contact with the sample. To confirm the proper ohmic contact a *V-I* plot was measured prior to measurement.

The temperature increase for the measurement is done through radiation process by using IR furnace; before the resistance measurement the temperature gets stabilized in every step and a fixed current passes through the sample from the top and bottom electrodes to eliminate contact resistance. The voltage is being measured by the lateral probes and the resistance (R) can be obtain through the Ohm's law (Equation 2.7).

$$\Delta V = R.I$$ Equation 2.7

Since the cross sectional area (A) of the sample and the distance between the lateral thermocouples (d) are inserted into the software before the measurement, the resistivity (ρ) can be calculated by the software from Equation 2.8.

$$R.A = \rho.d$$ Equation 2.8

The Seebeck coefficient, S, is obtained by measuring the induced voltage between the lateral probes ΔV, which is produced when a temperature gradient (ΔT) is generated between the two probes at T_1 and T_2 through heating the bottom block (Equation 2.9, Figure 2.12).

$$S = \frac{\Delta V}{T_1 - T_2}$$ Equation 2.9
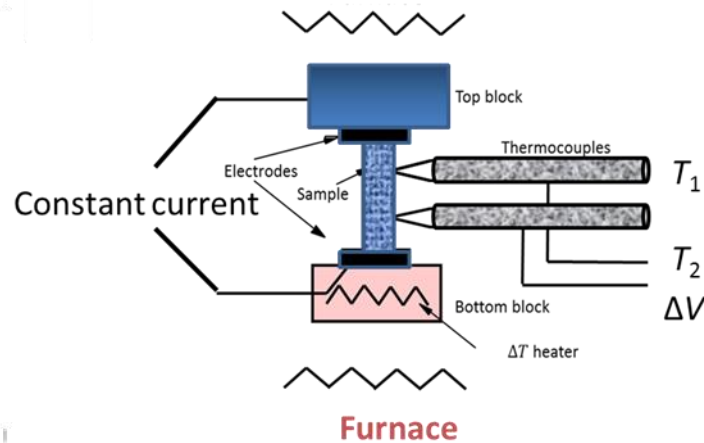
Figure 2.12   Schematic demonstration of measurement principles in ZEM-3.

2.8 Thermal analysis

Thermal analysis is the measurement of changes occurring in physical or chemical properties of a substance during a controlled heat treatment.[242] A typical instrument for thermal analysis includes a furnace controlled through a temperature programmer where the test sample is held. The furnace is placed in a closed chamber under a controlled atmosphere, but the chamber can be connected to evolved gas detection if the physical or chemical process involves gas or vapor emission. Thermal analysis measurements result in a thermal analysis curve, the features of which i.e. peaks, discontinuities, slope changes, relate to different thermal events in the test sample. Various types of measurement can be carried out depending on interest, such as the absolute values of the property, the difference in the property of the test sample compared to that of a reference material, or the changing rate of the property with temperature. The thermal events consist of phase transition, melting, sublimation, decomposition, glass transition, oxidation, tarnishing, combustion, volatilization, heterogeneous catalysis, or addition.

Differential scanning calorimetry (DSC) is a power-compensated technique, in which the test sample and a reference material are maintained at an identical temperature through

the controlled temperature programme. The energy is independently supplied to the sample and the reference, and the difference between the energy supplied is recorded against the corresponding temperature. The deviations from the DSC baseline occur in either an endothermic or exothermic direction, depending upon whether more or less energy has to be supplied to the sample compared to the reference during thermal events.

Thermogravimetric analysis (TGA) is the technique measuring the mass changes in the test sample with temperature using a thermo-balance. Actual TG curves appear under various forms depending on the involved materials and processes. A record of derivative thermogravimetric (DTG) curves can help to resolve the stages of complex TG curves. Because not all thermal events are accompanied by a mass change, TG is mostly applicable for desorption, decomposition, and oxidation, i.e. to measure the accurate conditions (temperature, atmosphere) for a physical or chemical process to occur, to indicate the thermal stability range of materials, to identify minerals and polymers, to determine the corresponding reactions, to act as a complementary technique for determining the mechanism of a process, and to define the kinetic of a reaction or vapour pressure of a sample.

A small amount of sample, spreading thinly and evenly inside the crucible, is required to ensure uniform and fast heat transfer, to prevent self-heating or self-cooling as reaction occurs, to reduce gas exchange with surrounding environment, and to protect the instrument in case of explosion or deflagration, which leads to irreproducibility. The sample containers, made of aluminum, gold, or graphite, are commercially available. The reference materials can be an empty crucible or sapphire, and samples can be liquid, powder, disk, flock, or fiber. The lid should be pierced onto the crucibles, especially when volatile products are generated during the process.

2.9 Electron microscopy

Interaction of an incident electron with the sample (Figure 2.13) can be both elastic and inelastic, which can provide different information from the sample. Once the incident beam penetrates through the sample and is elastically scattered by the atomic nucleus or outer

41

electrons it can deflect and leave the specimen as backscattered electrons (BSE). Backscattered electrons can supply compositional and topographic information. BSEs typically have energy higher than 50 eV, and due to their more interaction with heavier atoms can supply atomic number contrast in SEM. Interaction of the primary electrons with the surface of the specimen can result in the ionization of atoms, which can emit weakly bound electrons (secondary electrons). Secondary electrons (SE) with an average low energy of 3 to 5 eV can escape from sample surface (few nm) and provide topographic information regarding the roughness and texture of the surface. By knocking out a secondary electron from the inner shell another electron from the outer shell can occupy the vacancy and generate a characteristic X-ray. Characteristic X-rays can give chemical information and are used in energy dispersive X-ray spectroscopy (EDX). The excess energy from filling an inner shell vacancy by an outer shell electron can result in knocking out another electron from the outer shell which referred to as auger electron. Auger electrons have low energy and supply chemical information about the specimen. If the sample is thin enough (typically less than 1μ) some of the electrons can pass through and be analyzed for transmission electron microscopy (TEM). The evaluated error for EDX measurement is considered to be few atomic percent.[243]
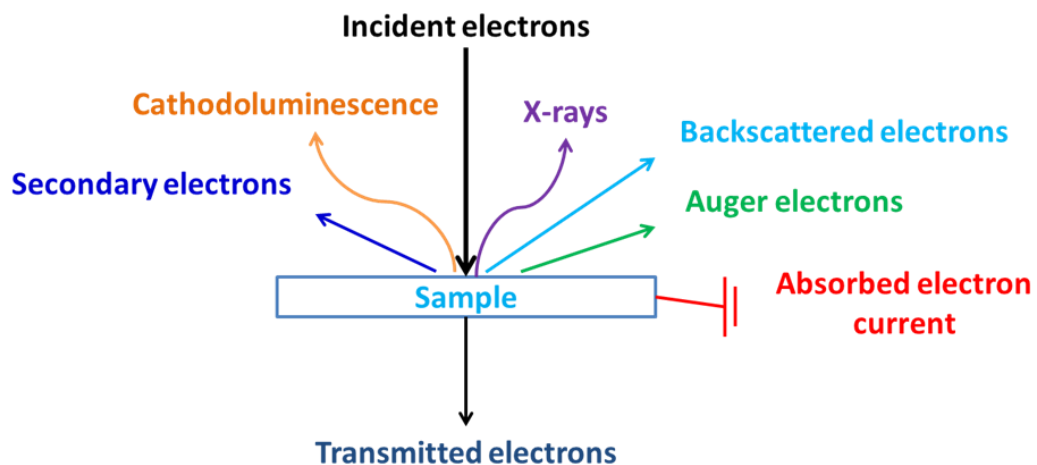
Figure 2.13   Interactions of electrons with specimen.

42

2.10 Thermoelectric Measurements precautions

To obey the following rules while working in the thermoelectric field is useful and to some extent necessary to avoid any data misrepresentation.

- It is important to achieve the highest purity possible for the powder before proceeding to consolidation process.
- Consolidation process should be devised in a way not only to achieve the highest relative density (depending on the compound, but typically higher than 95%) but also to assure no change in the purity of the sample. For this purpose XRD can be done on the pellet after the sintering.
- For thermal diffusivity measurement, all the graphite from pressing process needs to be removed from the sample surface and the sample should have appropriate uniform thickness. Measurement temperatures should be in the stability range of the compound. After cutting the sample for ZEM measurement, part of the pellet can be ground and XRD can be performed to verify the purity of the sample.
- In addition to the above mentioned parameters, the rectangular bar for the electrical resistivity and Seebeck measurements needs to have right dimension and flat parallel surfaces to provide a decent contact with both electrodes and thermocouples. It is important to measure the sample cross section area and lateral probe distance accurately to minimize errors of the resistivity value.
- All the obtained data need to be repeatable and reproducible on the same sample as well as a second sample synthesized by the same method. It is necessary to repeat 2 to 3 measurement points to confirm the stability and reproducibility of the data.[244]
- No measurement should be performed on a cracked, low purity, low density and deformed sample.
- In case of obtaining unusual results, it is highly recommended that the sample be measured by other colleagues in the same laboratory or other laboratories.

Like any other experimental measurements, thermoelectric measurements are entangled with experimental errors and standard deviations. It is important to be aware of those errors while analyzing the data. The commonly accepted errors based on the instrument

used in this thesis are 5%, 3% and 5% for electrical conductivity, Seebeck coefficient and thermal diffusivity measurement, respectively. The estimated error in density measurement is around 2%. Based on the aforementioned values the approximate error for the figure of merit *ZT* can be evaluated (Equation 2.10)[245] to be around 10%. To better understand the standard deviation of the data, round robin measurements were performed in the past[246–248] and the standard deviations based on the 2σ method were around, ±7%, ±6.5%, ±3.5% and ±14% for electrical resistivity, Seebeck coefficient, thermal diffusivity and *ZT*, respectively.[246]

$$\frac{dZ}{Z} = \sqrt{(2\frac{dS}{S})^2 + (\frac{d\sigma}{\sigma})^2 + (\frac{d\kappa}{\kappa})^2} \qquad\qquad \text{Equation 2.10}$$

Chapter 3

Effect of Bi and Sb doping on Mg$_2$Si

3.1 Introduction

In this chapter, the effect of Bi and Sb doping on the thermoelectric properties of Mg$_2$Si is studied. Doping is a major problem in Mg$_2$Si, as *p*-type doping has thus far not produced competitive efficiencies, and *n*-type doping is problematic because of the low solubility of the typically used dopants Sb and Bi. This investigation shows experimentally that these dopants can indeed replace Si in the crystal lattice, and excess Sb and Bi atoms are present in the grain boundaries in form of Mg$_3$Sb$_2$ and Mg$_3$Bi$_2$. As a consequence, the carrier concentration is lower than the formal Sb/Bi concentration suggests, and the thermal conductivity is significantly reduced. To further shine light onto the thermoelectric properties of Sb- and Bi-doped Mg$_2$Si, comprehensive detailed studies are presented here about the location of the dopants, both with respect to the crystallographic location and the macrostructure.

3.2 Material Synthesis

The Mg (99.8%, Alfa Aesar, -20+100 mesh), Si (99.9%, Alfa Aesar, -100 mesh), Sb (99.5%, Alfa Aesar, -100 mesh) and Bi (99.5%, Alfa Aesar, -325 mesh) powders were mixed according to the stoichiometry ratio in a glove box under Argon atmosphere. Excess Mg (4%) was used to counter the effect of magnesium evaporation during the reaction; thus the starting ratios were 2.08 Mg : (1 − x) Si : x Sb and 2.08 Mg : (1 − x) Si : x Bi, respectively. The reaction mixtures were put into alumina crucibles, which were then placed into fused silica tubes. The tubes were then heated at 823 K in a resistance furnace for 3.5 days. The products were crushed and reheated at around 873 K for 5 days, and then cooled down to room temperature naturally by switching off the furnace. For x = 0.02, the samples appeared to contain only Mg$_2$Si$_{1-x}$Sb$_x$ and Mg$_2$Si$_{1-x}$Bi$_x$, respectively, with traces of MgO, i.e. no unreacted Si, Sb or Bi were detected. Larger amounts of Sb or Bi resulted in noticeable formation of Mg$_3$Sb$_2$ or Mg$_3$Bi$_2$. The doped Mg$_2$Si samples were ground and then consolidated in an argon atmosphere under a pressure of 32 MPa at 973 K. The pressure was

released after heating for 2 hours to eliminate strain on the pellets during the cool-down procedure. Additional powder X-ray diffraction experiments on Mg_2Si and $Mg_2Si_{0.98}Bi_{0.02}$ were performed at the CMCF-II beamline at the Canadian Light Source. Synchrotron radiation from a bending magnet port was monochromatized to 18 keV (0.68801 Å) with a double crystal monochromator and focused to the sample with a toroidal mirror. Powder diffraction patterns were measured in the Debye-Scherrer configuration with a versatile ACCEL MD2 micro-diffractometer and MarMosaic mx300 CCD X-ray detector. These experiments confirmed the results obtained from the Inel diffractometer, and showed evidence for a small unit cell expansion upon doping with Bi, namely from a = 6.33504(5) Å to a = 6.34227(6) Å, as shown in Figure 3.1. The EDX results confirmed the existence of Sb and Bi in the samples with some Sb- and Bi-rich regions, respectively; the analysis of different crystals resulted in an average ratio of 2.05 Mg : 0.94 Si : 0.01 Bi. Differential scanning calorimetry (DSC) was used to examine the thermal stability of the samples with x = 0.02.
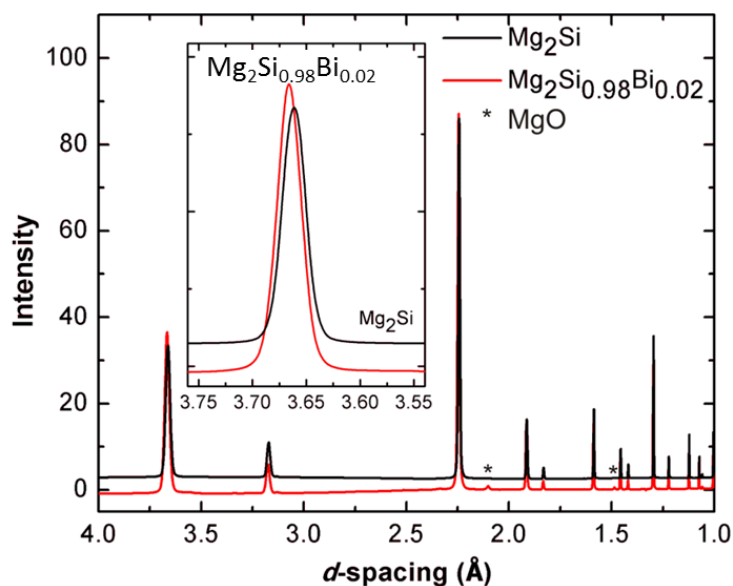
Figure 3.1   Experimental powder diagrams of Mg_2Si and $Mg_2Si_{0.98}Bi_{0.02}$.

The DSC measurement was performed under argon flow by using the NETZSCH STA 409PC Luxx instrument with a heating rate of 10 K min^{-1} from 300 K to 1073 K. No phase transition was detected, and the weight loss was < 2%, possibly within experimental error. The plots are presented in Figure 3.2.
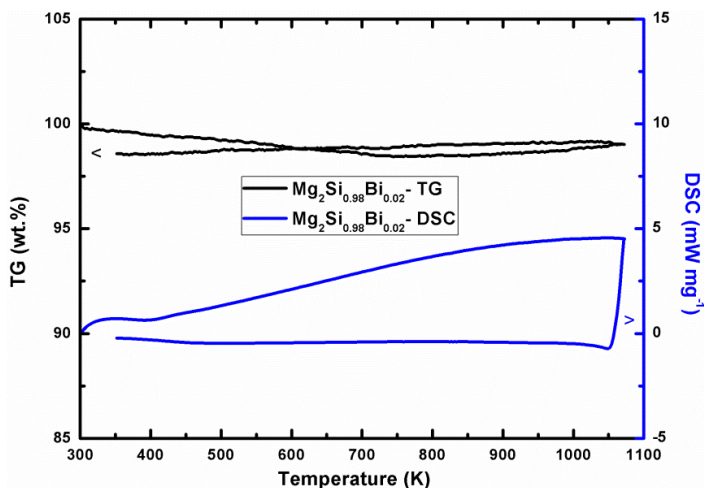
Figure 3.2　　TG and DSC of $Mg_2Si_{0.98}Bi_{0.02}$.

3.2.1 Transmission electron microscopy

Atomic-scale structural characterization and elemental analyses were performed using scanning transmission electron microscopy (STEM) operating in a high-angle annular dark-field imaging (HAADF) mode and the Energy dispersive X-ray Spectrometry (XEDS). Conventional TEM is primarily a broad-beam based technique, wherein all the scattered electrons, upon interacting with the specimen, are collected over a large illumination area on the specimen. In these conditions, images are strongly dependent on the thickness of the sample and objective lens-focus conditions. As opposed to this, STEM-HAADF employs a raster scanning electron probe to collect electrons that are elastically scattered at high angles. Upon converging the electron beam into a sub-angstrom probe, an atomic-scale image of materials can be obtained. The high angle annular dark field (HAADF) detector, as the name suggests, is a detector designed in an annular geometry and placed in a diffraction plane

below the sample so as to collect electrons emerging from the specimen at high scattering angles. Since the intensity of these high-angle scattered electrons is directly related to the atomic number of scattering atoms under the electron beam, the resulting STEM-HAADF image provides an atomic number "Z"-contrast image with intensities proportional to $Z^{1.6}$. For instance, in the case of the Mg_2Si sample doped with Bi, the atomic columns containing Bi ($Z = 83$) is expected to appear significantly brighter compared to the bulk of the matrix crystal.

Atomically-resolved STEM-HAADF images were acquired using a FEI-Titan cubed TEM, equipped with two hexapole-design spherical aberration correctors of the probe and image forming lenses. The microscope was operated in STEM mode at an accelerating voltage of 300 kV and the images were acquired using a Fischione Instruments HAADF detector. Image simulations were carried out with the multislice method by implementing the Kirkland code[249] in order to validate the structural model and deductions of the dopant site preference. For STEM characterization, the samples were thinned by mechanical polishing to 180 μm thickness, then dimple-ground with a diamond paste to a central thickness of 20 μm and finally ion milled (using Gatan PIPS model) to electron transparency.

3.2.2 Electronic structure calculations

The electronic structure calculations were performed using density functional theory (DFT) with the Perdew-Burke-Ernzerhof (PBE) generalized gradient approximation (GGA)[250] as implemented in the Vienna *ab initio* simulation package (VASP) code.[251–254] To obtain a more accurate band gap, additional calculations were performed via the GW approximation (GWA), which utilizes the one-particle Green's function and the screened Coulomb interaction W.[255,256] For the GGA calculation, the projector-augmented wave (PAW)[257,258] method was adopted with $2p^63s^2$ and $3s^23p^2$ as valence electrons for the Mg and Si atoms, respectively. An energy cut-off of 332 eV and an appropriate Monkhorst-Pack scheme was employed for the Brillouin zone with a dense k-mesh of $25 \times 25 \times 25$ for the Seebeck coefficient calculation. The band structure was calculated with the VASP code with

a $16 \times 16 \times 16$ k-point set. For doping with Sb and Bi, a $2 \times 2 \times 2$ supercell was created from the Mg_2Si crystal structure, where one out of 32 Si atoms was replaced either with an Sb or a Bi atom. The stoichiometry of the doped model is thus approximately $Mg_2Si_{0.97}Pn_{0.03}$ ($Pn =$ Sb, Bi). For the Bi case, spin-orbit coupling was included in the calculation. By using VASP output and symmetry, the V2Boltz program[259] was applied on the basis of semiclassical Boltzmann transport theory to calculate the temperature-dependent Seebeck coefficient for n-doped Mg_2Si-based thermoelectric materials within the rigid band approximation.[260]

3.2.3 Band gap measurements

To verify the band gap, an infrared transmission spectrum was obtained from a ground sample of undoped Mg_2Si at room temperature using a Fourier transform IR spectrometer, utilizing the Mid Infrared (560 - 8000 cm^{-1}) Spectromicroscopy beamline at the Canadian Light Source Inc. The sample was loaded on the 300 μm culets of a Sintek mini type IIa diamond anvil cell. The spectra were recorded on a Hyperion 3000 IR microscope with a liquid nitrogen cooled MCT detector. For the measurement, the diamond was firstly measured as background spectrum. After extracting the background, the sample with ~100 μm was focused by microscopy and measured. Spectral data collection employed a resolution of 4 cm^{-1} and 512 scans.

The mid and far infrared reflectance spectra of undoped Mg_2Si and Mg_2Si doped with Bi or Sb were measured at the National Synchrotron Light Source, Brookhaven National Laboratory. The sample preparation procedure was the same as described above. Far-infrared reflectivity experiments were performed at the side-station of the U2A beamline. Mid-infrared reflectivity was measured with a Bruker Vertex 80v FTIR spectrometer and a Hyperion 2000 IR microscope attached with a liquid nitrogen cooled HgCdTe detector. A conventional globar source was used to minimize any intensity fluctuation during the measurements. The intensity of the source was calibrated against the synchrotron ring current using a gold foil. A KBr beam splitter was used to cover the mid-IR region, and the spectral resolution of 4 cm^{-1} applied to all spectra. The reflectance was converted to absolute

reflectivity by normalization to the reflectance diamond substrate measured under identical experimental conditions. Optical conductivity was obtained by Kramers-Kronig (K-K) analysis of data obtained from normal incidence reflectivity measurements, then fit using a variational K-K constrained dielectric function, as implemented in the REFFIT code.[261] The dc conductivity is obtained from a Drude model by extrapolation to zero frequency. Since the mid and far infrared spectra were recorded on different detectors, the reflectances in the two regions were connected manually by matching to the mid-infrared reflectance at 600 cm^{-1} (0.75 eV).

3.2.4 Hall measurement

The Hall measurements were made from 5 K to 300 K using a cryostat equipped with a 5 T magnet and a linear research AC resistance bridge. Ohmic contacts were made by using silver paint. The Hall mobility, μ_H, was calculated from the relation $\mu_H = \sigma \, n^{-1} \, e^{-1}$ with $n = $ carrier concentration and $e = $ electron charge.

3.3 Results and Discussion

3.3.1 Micro- and Nanostructure

Low-magnification TEM imaging revealed the polycrystalline nature of the sample with grain sizes in the order of 7 μm. We did not observe any formation of Bi-rich precipitates in the matrix. Further, STEM-HAADF characterization was performed at an atomic-resolution to locate the doped Bi atoms. The principal regions of interest included the bulk of the sample, and the grain boundaries. Figure 3.3a and Figure 3.3b show the atomic-resolution STEM-HAADF image from the bulk of the $Mg_2Si_{0.98}Bi_{0.02}$ sample, oriented along the [110] zone axis. A significant number of atomic columns with brighter intensity are distributed randomly over the lattice. Due to the Z-dependence in these imaging conditions, we infer that these bright atomic columns correspond to columns containing Bi dopant atoms located on original Si atoms; deduced from the image simulations discussed further below.

The relative variation in the intensities among the bright atomic columns indicates that these columns could be containing single Bi dopants or possibly more Bi atoms. However, due to the lack of information on the location of the Bi atoms in the thickness of the sample, we cannot extract further quantitative information on the number of atoms within one column due to the sensitivity of the image intensity upon the precise location of the scattering atoms.
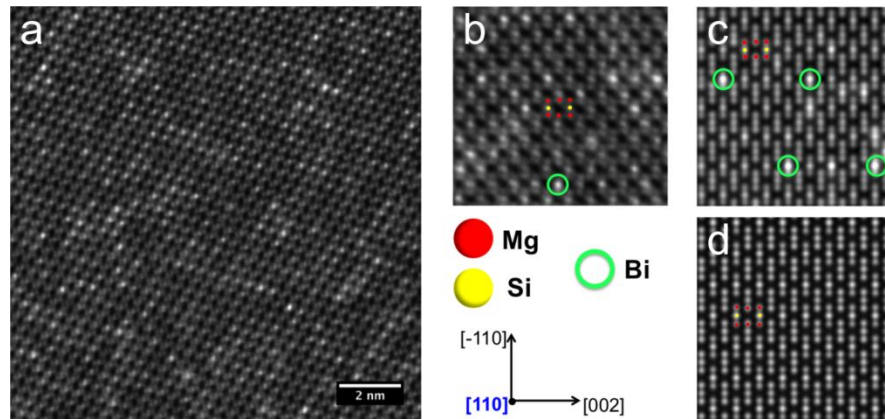
Figure 3.3   (a) and (b) STEM-HAADF image of $Mg_2Si_{0.98}Bi_{0.02}$. (c) and (d) Multi-slice simulation results obtained on $Mg_2Si_{0.98}Bi_{0.02}$ and Mg_2Si along the [110] zone axis, respectively.

In order to further confirm these deductions, we performed multi-slice image simulations for the $Mg_2Si_{0.98}Bi_{0.02}$ bulk matrix and pure Mg_2Si. These simulations utilized atomic models created from a ($10 \times 10 \times 10$ atoms) supercell viewed along [110] zone axis, in which the Bi dopants were randomly included as substitutional atoms on the Si sites. The resulting images obtained upon entering this structural model into the multi-slice simulations are shown in Figure 3.3c and **Error! Reference source not found.**d. Therein, the atomic olumns with brighter intensities correspond to those containing Bi-dopants. Unlike $Mg_2Si_{0.98}Bi_{0.02}$ (Figure 3.3c), the bulk of pure Mg_2Si (Figure 3.3d) does not reveal strong intensity fluctuations within the matrix, confirming our dopant atom deductions derived from the experimental STEM-HAADF image shown in Figure 3.3a.

From the STEM-HAADF images acquired from grain boundaries (Figure 3.4a and Figure 3.4b), it is clear that the Bi dopants also segregate - most likely in form of Mg_3Bi_2 as sometimes found in the X-ray diagrams - at grain boundaries as deduced from the increased intensity of the image. This is further confirmed from XEDS line scans recording the signal of the Bi $L\alpha_1$ peak as a function of position (Figure 3.4c).
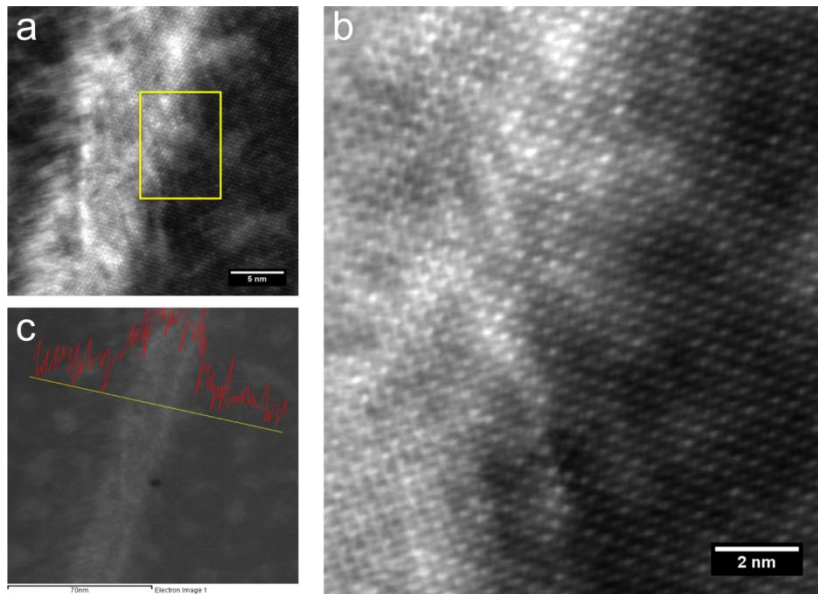
Figure 3.4　(a) Atomic-resolution STEM-HAADF image of $Mg_2Si_{0.98}Bi_{0.02}$ demonstrating Bi segregation at the grain boundary (GB). (b) STEM-HAADF image acquired from the yellow marked region in (a). (c) EDX line-scan for Bi (red) over the same yellow marked area illustrating the GB segregation of the Bi atoms.

3.3.2 Electronic structure

The density of states calculated via the GGA vs. the GW approach are depicted in Figure 3.5 (left). In each case, a narrow gap separates the valence band, mostly comprised of Si-p states from the conduction band, dominated by Mg states. The use of the screening correction (GW) did not change the valence band, but shifted the empty states uniformly towards higher energies. As a result, the calculated band gap increased from 0.2 eV to 0.67

eV, ultimately in agreement with experimental data.[262] The IR transmission spectrum of undoped Mg_2Si is shown in Figure 3.5 (right). The two arrows in the IR transmission spectrum indicate energies of creation and annihilation of a phonon associated with the gap excitation. The sloping feature of the transmittance indicates that the band gap is indirect with an energy of 0.65 eV, confirming the results of the GW modified DFT calculations discussed above. The phonon energy is estimated to be 0.06 eV. This can be compared to the maximum IR absorption frequency of a lattice vibration of Mg_2Si of 0.04 eV.
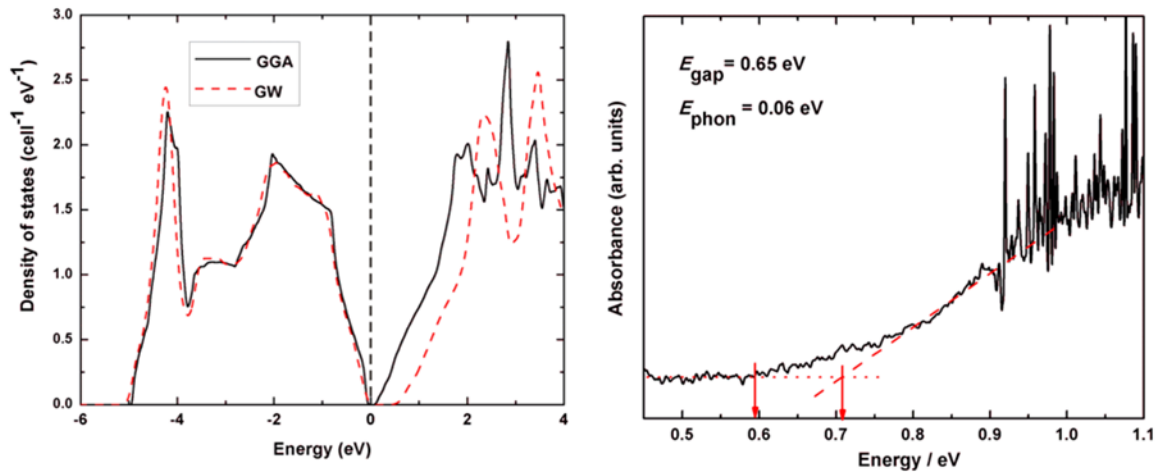
Figure 3.5   Density of states (left) and absorbance spectrum (right) of Mg_2Si.

The band structures are shown in Figure 3.6, revealing the indirect band gap. Similarly, a computed (indirect) band gap of 0.6 eV [263] was obtained after employing the modified Becke-Johnson local density functional (mBJLDA),[162,264] and applying the GW corrections to selected k-points yielded a computed gap of 0.65 eV.[265]
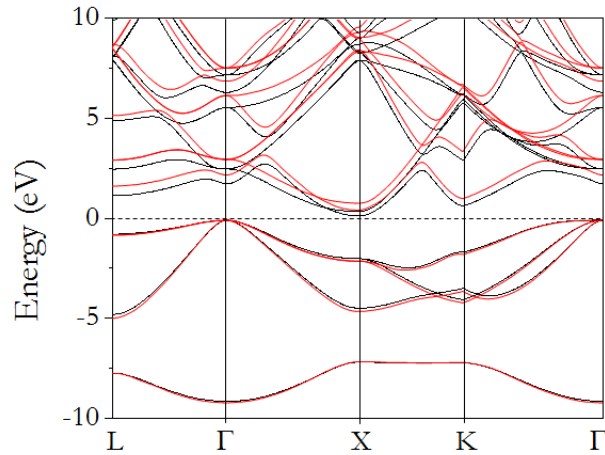
Figure 3.6   Band structure of Mg$_2$Si. Black: GGA, red: GW method.

The density of states of Sb- and Bi-doped Mg$_2$Si are compared in Figure 3.7. The composition is Mg$_{64}$Si$_{31}$*Pn* (*Pn* = Sb, Bi), which corresponds approximately to Mg$_2$Si$_{0.97}$*Pn*$_{0.03}$, i.e. a 3% doping level of *Pn* on the Si site. The total densities of states for both systems are very similar to that of pure Mg$_2$Si shown in Figure 3.5. The most significant observation is that even with a localized defect atom (*i.e.* Sb or Bi), the density of states projected to the *Pn* states shows the electrons from the dopant's electron is spread over the entire crystal and not localized in the band gap region. This observation confirms that one can apply the rigid band approximation for calculating the Seebeck coefficient. The relatively sharp peaks below −5 eV can be attributed to the interaction between the *Pn* atoms and the surrounding Mg and Si atoms. At a 3% dopant concentration, the excess electron occupied the conduction band orbitals up to 0.5 eV above the valence band edge. The thermopower can be estimated from the ground state band structure using the rigid band model by simply shifting the energy of the Fermi level according to the number of electrons donated by the dopants.
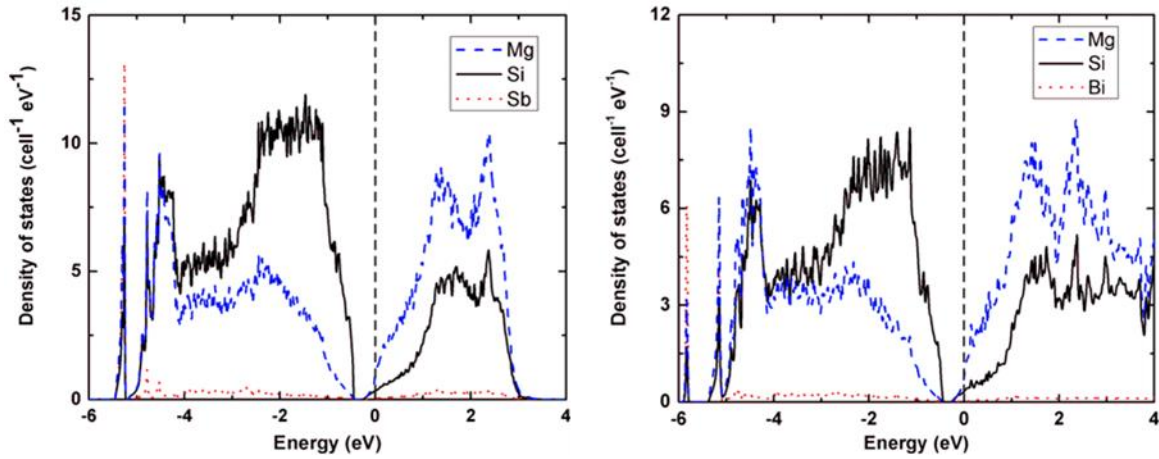
Figure 3.7   Density of states of $Mg_{64}Si_{31}Sb$ (left) and $Mg_{64}Si_{31}Bi$ (right).

Calculations on pure Mg_2Si and at several Sb doping concentrations of Sb have been performed (Figure 3.8). The negative Seebeck coefficient of doped Mg_2Si is simply a consequent of *n*-doping. The absolute magnitudes of the Seebeck coefficients were found to decrease with dopant concentration. At a given dopant concentration, the absolute value increases smoothly with increasing temperature, e.g. for the $Mg_2Si_{0.98}Sb_{0.02}$ model from −60 µV K^{-1} at 300 K to −150 µV K^{-1} at 800 K, and for the $Mg_2Si_{0.99}Sb_{0.01}$ model from −80 µV K^{-1} at 300 K to −170 µV K^{-1} at 800 K. The large Seebeck coefficient at low dopant concentration is due to the very sharp slope at the bottom of the conduction band indicating that the electron bands are fairly flat. At higher dopant concentrations the dopant electrons must populate the more free-electron like parabolic conduction bands, and therefore reduce the Seebeck coefficient.

55
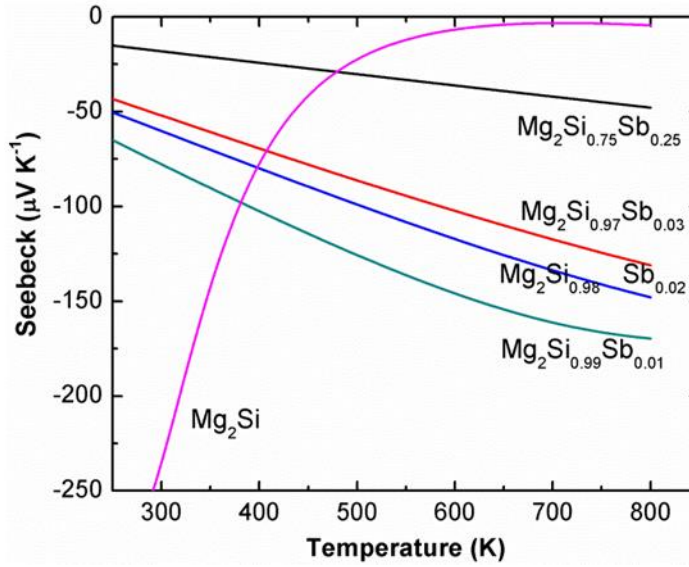
Figure 3.8   Calculated Seebeck coefficient of $Mg_2Si_{1-x}Sb_x$.

3.3.3 Physical Properties

The reflectivity spectra and the optical conductivity are shown in Figure 3.9. As an undoped, narrow gap semiconductor, Mg_2Si has lower reflectivity than the doped samples. The extrapolated zero frequency reflectivities for Mg_2Si, Sb-doped and Bi-doped samples are 0.5, 0.6 and 0.7, respectively. The dc conductivity obtained from K-K analysis is 166 $\Omega^{-1}cm^{-1}$ for the Sb and 177 $\Omega^{-1}cm^{-1}$ for the Bi case. These values are significantly lower than the ones obtained from four-probe measurements on the hot-pressed pellets (discussed below), most likely because the IR's limited penetration depth and spot size (about 400 μm^2), and is thus more influenced by the surface character.
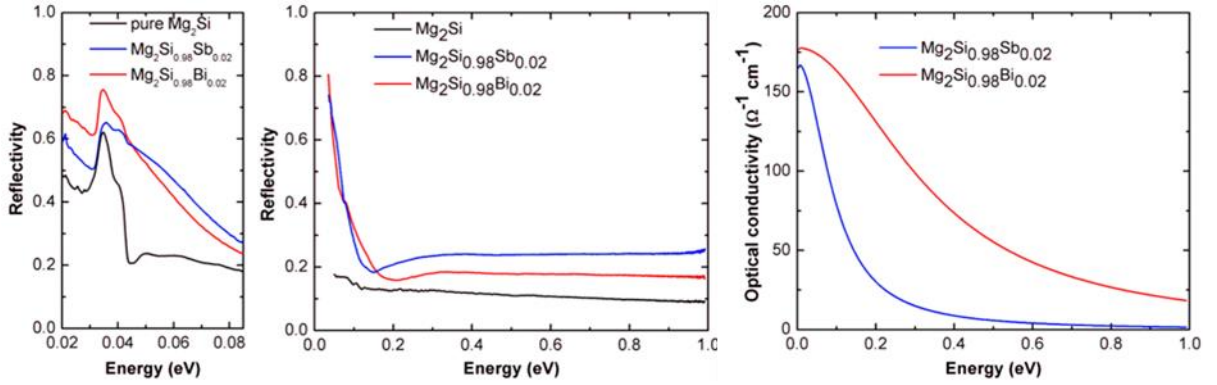
Figure 3.9   Reflectivity spectra (left and center) and optical conductivity (right) of
$Mg_2Si_{0.98}Sb_{0.02}$ and $Mg_2Si_{0.98}Bi_{0.02}$.

A unique feature in the reflectivity curves of the doped samples is the occurrence of a "dip" in their IR spectra. The minimum in the reflectivity is characteristic for a doped semiconductor and is known as the plasma reflection edge. According to the Drude model, the energy at the minimum corresponds to the plasma frequency, ω_P, which is related to the carrier concentration, n, and the effective mass, m^*, via $\omega_P^2 = n\ e^2\ \varepsilon^{-1}\ m^{*-1}$, where ε is the dielectric constant of the material.[266] The observed plasma energies for Sb- and Bi-doped Mg_2Si are 0.15 eV and 0.21 eV, respectively. The effective mass of the Bi-doped Mg_2Si may be twice as high, e.g. determined to be 1.1 m_e[267] vs. 0.47 m_e[268] with m_e = electron mass. Thus, the carrier concentration in the Bi-doped Mg_2Si is estimated to be roughly four times as high as that of the Sb-doped sample. The high quality of the IR measurement is reflected in the observation of reflectivity at the longitudinal-optical (LO) and transverse-optical (TO) phonon absorption branch in the far-IR region. The peak at 0.036 eV with a shoulder on the high energy side is caused by the *Reststrahlen* band due to the zone center LO and TO phonon absorptions. The result is in good accord with a previous measurement on a single crystal.[269] From the envelope of the band, the TO-LO splitting can be estimated.[270] For undoped Mg_2Si, the LO-TO splitting is 71.4 meV or 58 cm^{-1}. This is comparable to the previously measured value on a single crystal of 60 cm^{-1}. The *Reststrahlen* bands of Bi and Sb doped Mg_2Si samples are somewhat broader, giving splitting energies of 63 cm^{-1} and 67

cm^{-1}, respectively. Furthermore, the frequency of the TO vibration in $Mg_2Si_{0.98}Bi_{0.02}$ is 8 meV (6.6 cm^{-1}) lower than the pure sample.

The carrier concentration, mobility and electrical conductivity are depicted in Figure 3.10 for both $Mg_2Si_{0.98}Sb_{0.02}$ and $Mg_2Si_{0.98}Bi_{0.02}$. Between 5 K and 300 K, no noticeable temperature dependence of the Hall coefficient, R_H, (and thus the carrier concentration) was detected, e.g. for Bi-doped Mg_2Si, R_H ranged from –0.0677 cm^3 C^{-1} at 5 K to –0.0658 cm^3 C^{-1} at 300 K, the negative sign being indicative of the expected n-type character of the carriers. The carrier concentrations of $n = 3.5 \times 10^{19}$ electrons per cm^3 and 9.5×10^{19} electrons per cm^3 for Sb and Bi-doped Mg_2Si, respectively, are in qualitative agreement with our TEM and electronic structure studies: replacing Si with Pn = Sb or Bi increases the valence electron count, but not all Pn atoms replaced Si, as we found Mg_3Pn_2 in the grain boundaries. Nominally, replacing 2% of Si with Pn would result in extrinsic charge carriers of $n = 3.1 \times 10^{20}$ cm^{-3}, considering that each Pn atom comprises one more valence-electron than Si. Furthermore, this is in good agreement with the estimated ratio of the carrier concentration from the reflectance spectroscopy experiments, where the Bi sample appeared to have much higher carrier concentration.
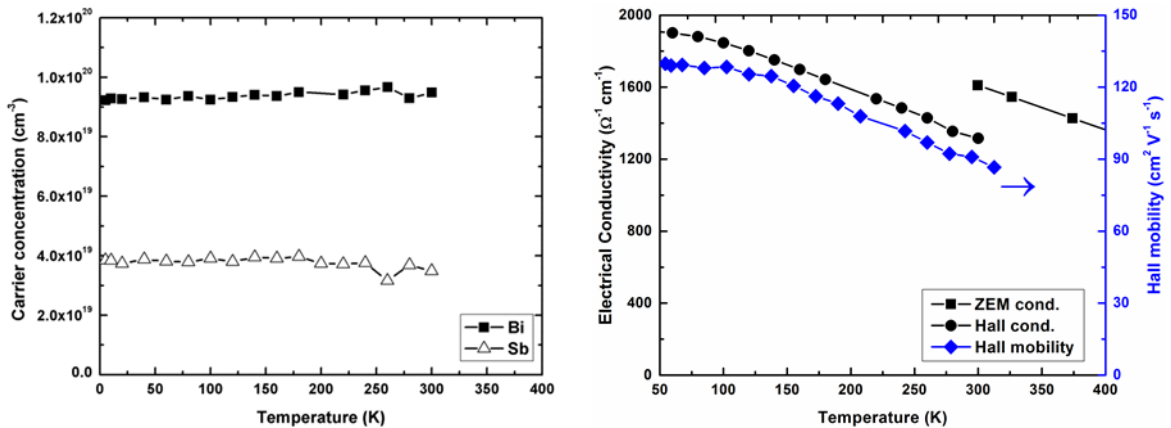
Figure 3.10   Carrier concentration (left) and Hall mobility and electrical conductivity (right) of $Mg_2Si_{0.98}Sb_{0.02}$ (white symbols) and $Mg_2Si_{0.98}Bi_{0.02}$ (black symbols).

Similarly, Nolas et al. determined $n = 1.5 \times 10^{20}$ cm^{-3} for the same Sb content,[268] and Tani et al. found $n = 1.5 \times 10^{20}$ cm^{-3} for the same Sb[119] and $n = 1.1 \times 10^{20}$ cm^{-3} for the same Bi concentration,[127] while Bux et al.[271] were able to use all extra electrons from Bi after ball-milling, followed by spark-plasma-sintering, resulting in $n = 3.2 \times 10^{20}$ cm^{-3} (Table 3.1 and Table 3.2).

Table 3.1   Thermoelectric properties of Mg$_2$Si$_{0.98}$Sb$_{0.02}$ at 300 K - 320 K (first value) and at ≈800 K (second value).

Property	our work	Nolas et al.[268]	Tani et al.[119]	Ioannou et al.[105]
σ/(Ω^{-1}cm^{-1})	493 – 217	1000	1980 – 650	2850 – 1200
α/(μV K^{-1})	116 – 229	75	90 – 195	62 – 130
κ/(W m^{-1}K^{-1})	n/a	6.7	6.58 – 3.72	8.53 – n/a
n/(cm^{-3})	3.5×10^{19}	1.2×10^{20}	1.5×10^{20}	2.5×10^{20}
μ/(cm^{2}V^{-1}s^{-1})	n/a	50	83	72
ZT	n/a	0.03	0.006 – 0.51	0.05-0.32

Table 3.2   Thermoelectric properties of Mg$_2$Si$_{0.98}$Bi$_{0.02}$ at 300 K - 320 K (first value) and at ≈800 K (second value).

Property	our work	Bux et al.[271]	Tani et al.[127]	Choi et al.[272]
σ/(Ω^{-1}cm^{-1})	1610 – 640	3125 – 1520	1150 – 540	1985 – 850
$-\alpha$/(μV K^{-1})	94 – 198	72 – 130	100 – 240	88 – 190
κ/(W m^{-1}K^{-1})	7.26 – 2.95*	6.51 – 4.18	6.35 – 3.58	6.15 – 4.05
n/(cm^{-3})	9.5×10^{19}	3.2×10^{20}	1.1×10^{20}	n/a
μ/(cm^{2}V^{-1}s^{-1})	87	58	64	n/a
ZT	0.08 – 0.56*	0.05 – 0.46	0.05 – 0.78	0.05 – 0.64

*: Properties at 660 K.

As expected, the mobility, μ, decreases with increasing temperature, and therefore the electrical conductivity, σ, decreases in parallel. Around 300 K, we obtained $\mu = 87$ cm^2 V^{-1}s^{-1} and thus $\sigma = 1315$ Ω^{-1}cm^{-1}. The slope of the electrical conductivity determined from the Hall data matches nicely the one obtained from the same pellet using the ULVAC ZEM-3, and the absolute value at 300 K of $\sigma = 1610$ Ω^{-1}cm^{-1} differs by 22%. Tani and Bux found lower values for the mobility, e.g. at 300 K in case of Bi doping $\mu = 64$ cm^2 V^{-1}s^{-1} (Tani) and $\mu = 58$ cm^2 V^{-1}s^{-1} (Bux). The mobilities of the Sb-doped samples are of the same order of magnitude, ranging from 50 cm^2 V^{-1}s^{-1} (Nolas) to $\mu = 83$ cm^2 V^{-1}s^{-1} (Tani).

Figure 3.11 compares electrical conductivity (left) and Seebeck coefficient (right) of Mg$_2$Si$_{0.98}$Sb$_{0.02}$ and Mg$_2$Si$_{0.98}$Bi$_{0.02}$ from 300 K to 840 K, measured using the ZEM-3. The electrical conductivity of Mg$_2$Si$_{0.98}$Bi$_{0.02}$ continues to decrease throughout this temperate range, as does σ of Mg$_2$Si$_{0.98}$Sb$_{0.02}$. The latter is significantly smaller ($\sigma = 490$ Ω^{-1}cm^{-1} at 300 K), mostly because of the smaller carrier concentration by a factor of roughly 3. This difference causes in turn the absolute Seebeck coefficient of the Sb-doped material to be larger, e.g. $S = -116$ μV K^{-1} vs. -94 μV K^{-1} at 300 K. The calculated Seebeck coefficient was smaller, because the calculation assumed that all extra electrons from Sb were available as charge carriers. That the carrier concentration is the main cause for these differences, is supported by the similarities of carrier concentration, electrical conductivity, and Seebeck coefficient of Mg$_2$Si$_{0.98}$Bi$_{0.02}$ with Tani's sample,[127] while Bux's sample has higher carrier concentration, electrical conductivity, and lower Seebeck coefficient.[271]
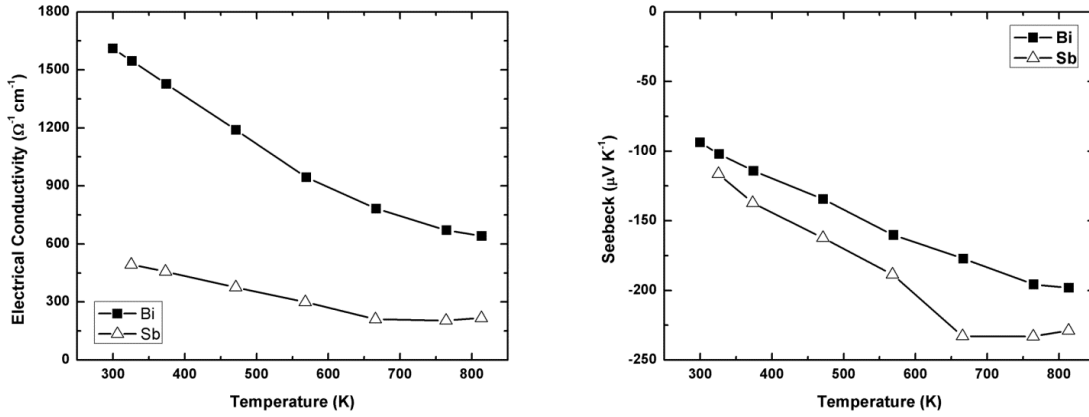
Figure 3.11   Electrical conductivity (left) and Seebeck coefficient (right) of $Mg_2Si_{0.98}Sb_{0.02}$ (white symbols) and $Mg_2Si_{0.98}Bi_{0.02}$ (black symbols).

From the Seebeck coefficient, one can derive the effective mass, if the carrier concentration is known, assuming energy-independent scattering and parabolic band, via $S = 8/3 \, \pi \, k_B^2 \, e^{-1} \, h^{-2} \, m^* \, T \, (1/3 \, \pi \, n^{-1})^{2/3}$.[273] At 300 K, this results in $m^* = 0.62 \, m_e$ for the Sb case and $m^* = 1.06 \, m_e$ for the Bi case, in qualitative agreement with Nolas' 0.50 m_e for Sb and Bux's 1.1 m_e for Bi. Relating this to the plasma frequencies discussed above with our experimental values for the carrier concentration, we calculate $m^*(Bi)/m^*(Sb) = n(Bi) \, \omega_P(Bi)^{-2} / \{n(Bi) \, \omega_P(Bi)^{-2}\} = 1.38$, compared to $1.06 / 0.62 = 1.71$ from the Seebeck data.

Finally, the thermal conductivity, κ, of a second $Mg_2Si_{0.98}Bi_{0.02}$ sample was determined up to 660 K, yielding decreasing values from 7.3 W $m^{-1}K^{-1}$ at 300 K to 3.0 W $m^{-1}K^{-1}$ at 660 K (Figure 3.12, left). These numbers, being significantly lower than those of undoped Mg_2Si, agree well with those of other authors working in this system (Table 3.2). Assuming these two Bi-doped materials have the same carrier concentration, as they were prepared the same way, this results in comparable (estimated) figure-of-merit values, e.g. ZT = 0.56 at 660 K (Figure 3.12, right), with the Bi sample from Tani (0.54 at 660 K),[127] which exhibited roughly the same carrier concentration. On the other hand, the Bi-doped material from Bux et al. with its higher carrier concentration exhibited smaller ZT values, e.g. 0.38 at 660 K.[271]
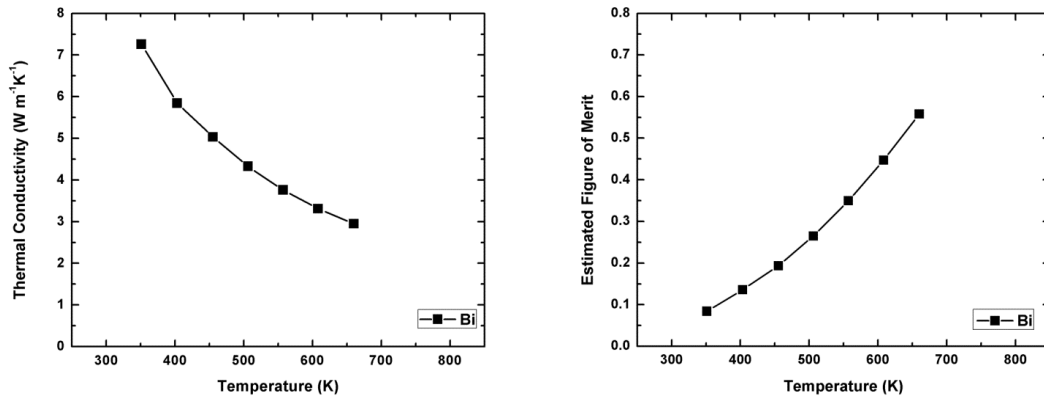
Figure 3.12 Thermal conductivity (left) and estimated figure of merit (right) of $Mg_2Si_{0.98}Bi_{0.02}$.

3.4 Conclusion

Sb- and Bi-doped Mg_2Si samples were prepared via annealing, followed by hot-pressing. Parts of the dopants replace Si, as shown via STEM-HAADF, while the rest forms Mg_3Sb_2 and Mg_3Bi_2, found between the grains of doped Mg_2Si particles. DFT calculations were performed both on pure and doped Mg_2Si models, resulting in the correct band gap size after GW correction, in accord with the results from the absorbance spectroscopy. These calculations also showed the validity of the rigid-band approximation for calculating the transport properties in dependence of the electron concentration. As the addition of Sb and Bi only partly led to Si substitution, the experimentally determined carrier concentration was lower than originally expected. These findings support the ones from Tani et al., who used a different synthesis and consolidation method (spark-plasma-sintering vs. hot-pressing), whereas Bux et al. obtained higher carrier concentration at the same nominal Bi concentration after incremental ball-milling. Therefore, Bux et al. found larger electrical conductivity and smaller Seebeck coefficient, yet ultimately smaller *ZT* values at the 2% doping level. In conclusion, the presence of Sb and Bi between the grains of doped Mg_2Si may well be advantageous with respect to the thermoelectric performance.

Chapter 4

Effect of Germanium Substitution on Thermoelectric Properties of Bi doped Mg$_2$Si

4.1 Introduction

In this chapter, the effect of germanium substitution for silicon in bismuth doped Mg$_2$Si is presented. To better understand the role of Ge, the doping level of bismuth was fixed at its optimum value, and the effects of the different Ge content on the band structure, thermoelectric properties as well as the micro- and nano-structure of Mg$_2$Si$_{0.977-x}$Ge$_x$Bi$_{0.023}$ ($0.1 \leq x \leq 0.4$) were investigated.

4.2 Experimental Procedures

Bismuth doped Mg$_2$Si$_{1-x}$Ge$_x$ samples were synthesized starting from the elements in a tantalum crucible according to the nominal stoichiometric ratio in an argon-filled glove box. We used Mg chips (99.98%, Sigma Aldrich, 4-30 mesh), Si powder (99.9%, Alfa Aesar, -100 mesh), Ge pieces (99.9999+%, Alfa Aesar, $\leq$ 2 cm) and Bi granules (99.99%, Sigma Aldrich). The tantalum crucibles were sealed under argon with an arc melter, and then placed into silica tubes. The sealed tubes were heated at 923 K for a week. Then the furnaces were switched off to allow for fast cooling down to room temperature. To obtain pure products, the samples were ground and then annealed at 1173 K for another week and thereafter cooled down by turning off the furnace. The purity of the synthesized samples was shown in the P-XRD pattern (Figure 4.1). All samples were pure, except for traces of MgO as also observed by others.[68,112,274] In the end, we settled on 0.023 Bi per formula unit, because using 0.03 or more Bi resulted in the formation of Mg$_3$Bi$_2$, as found in the X-ray powder diffraction patterns. Lattice parameter refinements yielded a smooth increase with increasing Ge content as expected based on the Si/Ge size ratio, resulting in a = 6.3670(2) Å (0.1 Ge), 6.37011(9) Å (0.2 Ge), 6.37363(4) Å (0.3 Ge), and 6.37648(6) Å (0.4 Ge).
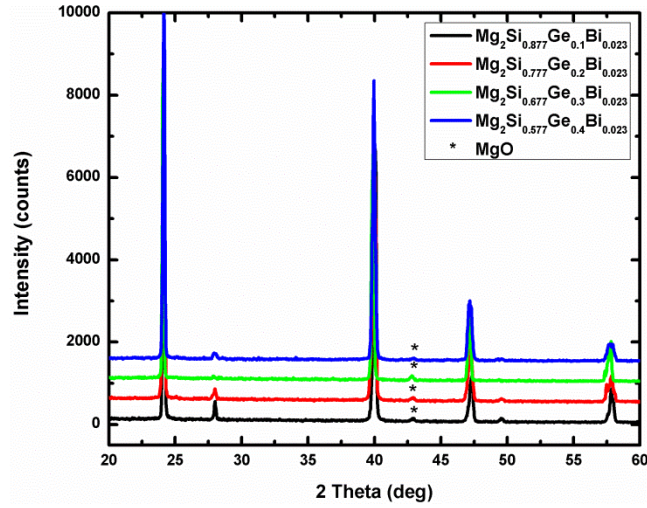
Figure 4.1   Experimental powder patterns of $Mg_2Si_{0.977-x}Ge_xBi_{0.023}$ ($0.1 \leq x \leq 0.4$).

For physical property measurements, the annealed powders were hot pressed for two hours at 973 K under 56 MPa in an argon atmosphere. The pressure was released after sintering to reduce strain and stress on the pellets during cooling. The hot-pressed pellets were 12.7 mm in diameter and 3 mm thick. These preparation methods are different from those used by Kim, who used 773 K for annealing for six hours, followed by hot-pressing for two hours at 1073 K under 70 MPa,[158] i.e. using a higher temperature and pressure in the last step.

To determine the thermal conductivity (κ) of the pressed samples, thermal diffusivity (α) measurements were carried out under flowing Ar. In order to verify the suitability of the Dulong-Petit approximation for thermal conductivity (κ) calculation, specific heat measurements were performed on the samples with high Ge content (Figure 4.2) using a NETZSCH 404C differential scanning calorimeter, and the measured values were in good agreement with our approximation.
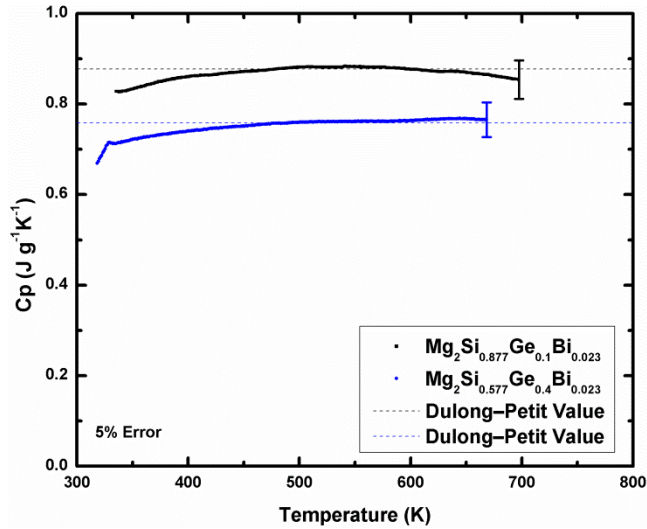
Figure 4.2   Specific heat of $Mg_2Si_{0.977-x}Ge_xBi_{0.023}$ (x = 0.1, 0.4).

The electrical conductivity (σ) and Seebeck coefficient (S) measurements were performed under a static helium atmosphere between 300 K and 800 K.The reflectance spectra were measured at the National Synchrotron Radiation Facility, at Brookhaven National Laboratory as described before.[116] The reflectance was converted to absolute reflectivity by normalization to the reflectance of a diamond substrate measured under identical experimental conditions. Optical conductivity was obtained by Kramers-Kronig (K-K) analysis of data collected from normal incidence reflectivity measurements, then fitted using a variational K-K constrained dielectric function, as implemented in the REFFIT code.[275] The DC conductivity was obtained from a Drude model by extrapolation to zero frequency.[276]

To examine the homogeneity of the samples at the micron level, energy dispersive X-ray (EDX) analysis was performed on parts of selected pressed pellets. For this analysis, the pellets were broken into smaller pieces, and the fracture surfaces were then analyzed without further treatments. The EDX results verified the existence of Bi in the samples with some Ge-rich regions. The analysis of different crystals resulted with $Si/Si_{nominal}$ and $Ge/Ge_{nominal}$ ratios of 92% to 100 % and 85 to 93%, respectively.

Atomic-scale structural characterization was performed on pieces of the hot-pressed pellets using aberration corrected scanning transmission electron microscopy (STEM) operating in a high-angle annular dark-field imaging (HAADF) mode.

Density functional theory (DFT) with the Perdew-Burke-Ernzerhof (PBE) generalized gradient approximation (GGA) [277] as applied in the Vienna *ab initio* simulation package (VASP) code was used for performing the electronic structure calculations.[251–254] For the GGA calculation, the projector-augmented wave (PAW) [257,258] method was selected with $2p^63s^2$ and $3s^23p^2$ as valence electrons for the Mg and Si atoms, respectively. A $4 \times 4 \times 4$ k-point mesh was used for the band structure calculation. For bismuth and germanium additions, a $2 \times 2 \times 2$ supercell was generated from the Mg_2Si crystal structure, where one out of 32 Si atoms was replaced with a Bi atom together with three, six, nine and twelve of 32 Si atoms replaced with Ge atoms. The compositions of the different models are thus $Mg_{64}Si_{31-x}Ge_xBi$ with x = 3, 6, 9 and 12.

4.3 Results and Discussion

Figure 4.3 shows the density of states (DOS) of the $Mg_2Si_{0.969-x}Ge_xBi_{0.031}$ ($0.094 \leq x \leq 0.375$) models. Because of the excess electron stemming from the Bi atoms, the conduction band is occupied to a small degree in each case. A slight reduction of the band gap with increasing Ge content confirms the same experimental observation of $Mg_2Si_{1-x}Ge_x$ in NMR studies.[274] Close to the Fermi level, the slope of the density of states of all the samples is very similar, which should result in comparable Seebeck coefficient values. The magnitude of the slope is indicative of a light band.
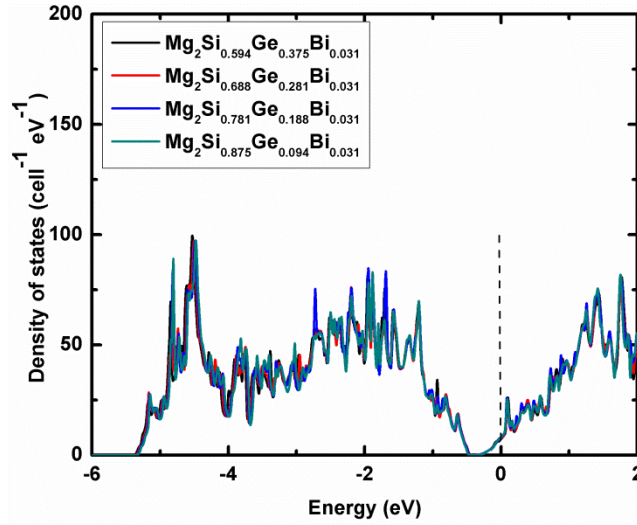
Figure 4.3   Density of states of $Mg_2Si_{0.969-x}Ge_xBi_{0.031}$ ($0.094 \leq x \leq 0.375$).

To better understand the nature of defects that could stem from the introduction of Ge, high resolution transmission electron microscopy (HRTEM, operating under scanning mode) was performed on the $Mg_2Si_{0.777}Ge_{0.2}Bi_{0.023}$ sample. Figure 4.4a displays a low magnification STEM (Scanning transmission electron microscopy)-HAADF (High-angle annular dark-field) image of the polycrystalline sample. Regions with bright intensities consist of atoms with higher atomic number (Ge: 32, Bi: 83) compared to the matrix (Mg: 14, Si: 12). The concentration of heavy atoms is higher near the outer edges of the grains, demonstrated in Figure 4.4b and Figure 4.4c that depict the areas marked red and green in Figure 4.4a, respectively. Because of the low Bi concentration (0.77 atomic-%) in the sample compared to Ge (6.67 atomic-%), it is postulated that the majority of the segregated atoms are Ge atoms, i.e. a Ge-rich domain is present at the edge of the Mg_2(Si,Ge,Bi) grains. The strain originating from the larger size of the heavier Ge atoms can be better accommodated along the grain boundaries, causing this concentration gradient. Figure 4.4d shows the STEM-HAADF image corresponding to the region marked in 2b. The image had a band-pass filter applied for enhanced visibility of segregated atoms. In addition to the Ge-rich domains, as shown by the blue lines, there are atoms, most likely Mg^{2+} because of its small size,

occupying interstitial sites as highlighted by the lines marked in red. Consequently, this affects the local strain distribution at the grain boundaries.
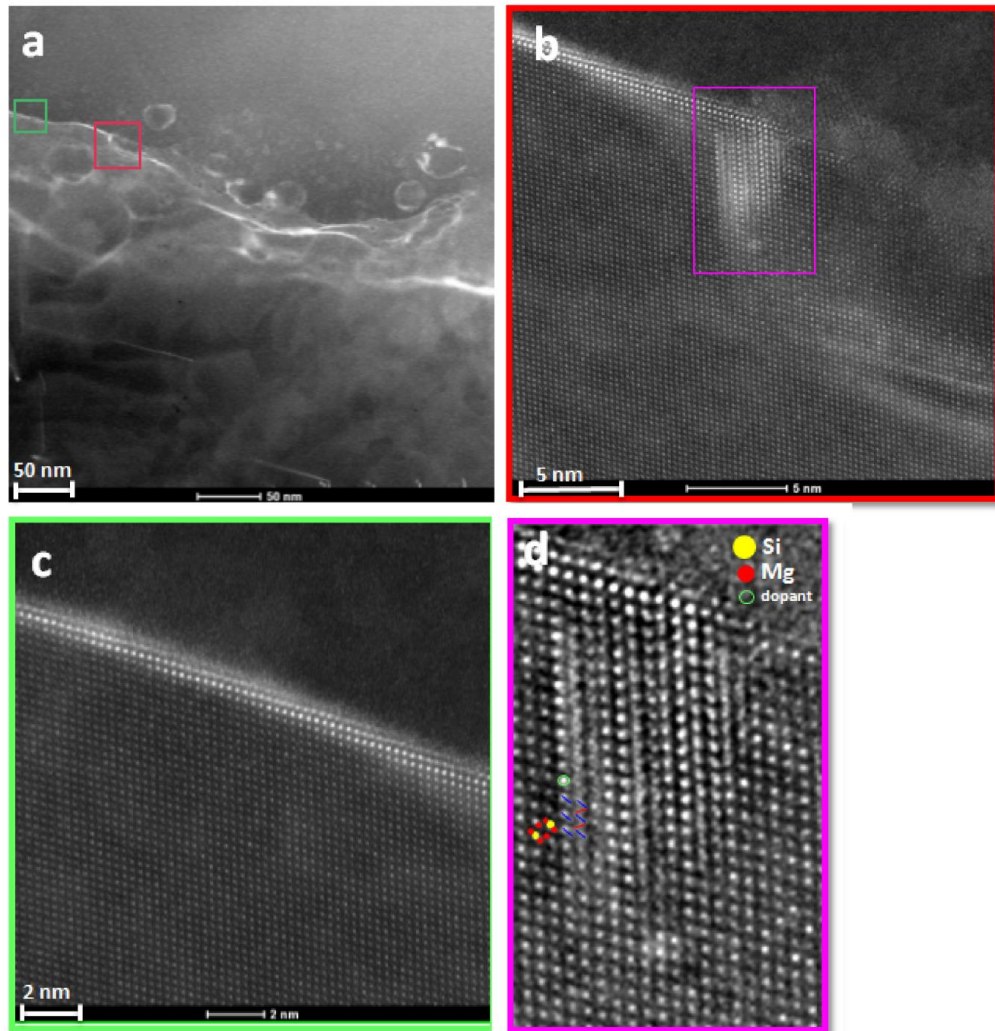
Figure 4.4   Low-magnification STEM-HAADF image of $Mg_2Si_{0.777}Ge_{0.2}Bi_{0.023}$. (b) and (c) STEM-HAADF image obtained from the red and green marked areas in (a) displaying the higher concentration of heavy atoms. (d) STEM-HAADF image corresponding to the region marked in (b) together with atomic simulation results showing the occupation of interstitial sites marked by red lines as well as the heavy atom segregation on Si sites marked by blue lines.

The thermal conductivity of all the samples decreases with increasing temperature due to acoustic phonon scattering (Figure 4.5). The $Mg_2Si_{0.677}Ge_{0.3}Bi_{0.023}$ sample showed the lowest thermal conductivity of $\kappa = 1.7$ W m^{-1}K^{-1}, compared to 3.9 W m^{-1}K^{-1} at 773 K obtained for Bi doped Mg_2Si.[127] Higher numbers of 2.5 W m^{-1}K^{-1}, 2.3 W m^{-1}K^{-1} and 2.3 W m^{-1}K^{-1} were obtained for $Mg_2Si_{0.7}Ge_{0.3}$, $Mg_2Si_{0.7}Ge_{0.3}$:$Sb_{0.02}$ and $Mg_2Si_{0.7}Ge_{0.3}$:$Bi_{0.02}$ by Kim et al., respectively.[114,158,278] All these values are drastically lower than the 7.3 W m^{-1}K^{-1} (at 320 K) to 3.0 W m^{-1}K^{-1} (at 660 K) we determined for the Bi-doped binary Mg_2Si.[116] Introducing germanium into the silicon position reduces the thermal conductivity especially at low temperatures, due to the increase in phonon scattering through mass fluctuation point defect scattering between these two elements[279,280] as well as the presence of Ge-rich domains. The decrease in κ with increasing mass contrast was also observed in other solid solutions such as $PbTe_{1-x}Se_x$ [281] and $Mg_2Si_{1-x}Sn_x$.[163,282]
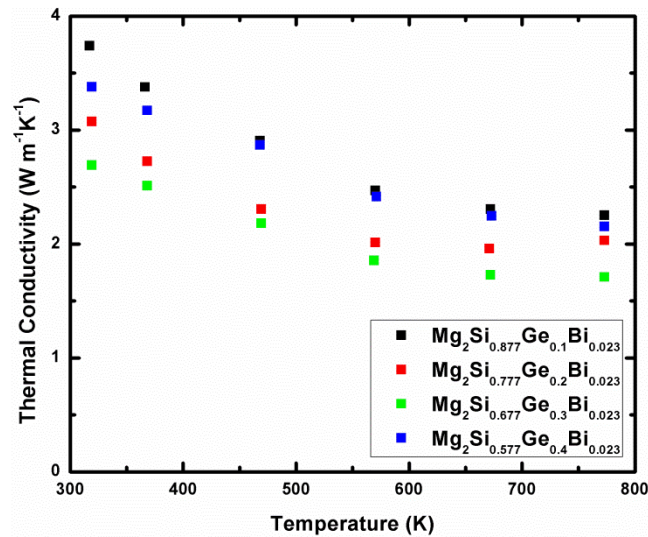
Figure 4.5   Thermal conductivity of $Mg_2Si_{0.977-x}Ge_xBi_{0.023}$ ($0.1 \leq x \leq 0.4$).

The higher thermal conductivity of the $Mg_2Si_{0.577}Ge_{0.4}Bi_{0.023}$ sample, compared to $Mg_2Si_{0.677}Ge_{0.3}Bi_{0.023}$, e.g. 2.2 W m^{-1}K^{-1} vs. 1.7 W m^{-1}K^{-1} at 773 K (Table 4.1), can in part

be explained by its higher relative density (98%, compared to 96% of the other samples), which facilitates both phonon and electron transportation. The extent of this effect may be estimated via the Maxwell-Eucken correction (Equation 4.1):

$$\kappa_P = \kappa_0 \frac{1-P}{1+\beta P} \qquad\qquad \text{Equation 4.1}$$

Table 4.1   Thermoelectric properties of $Mg_2Si_{0.977-x}Ge_xBi_{0.023}$ ($0.1 \leq x \leq 0.4$) at 773 K in comparison to literature data.

	x = 0.1	x = 0.2	x = 0.3	x = 0.4	$Mg_2Si_{0.7}Ge_{0.3}$: $Bi_{0.02}$ [158]	$Mg_2Si_{0.7}Ge_{0.3}$: $Sb_{0.02}$ [114]
$\sigma/(\Omega^{-1}cm^{-1})$	541	470	396	412	590	300
$S/(\mu V\ K^{-1})$	−190	−194	−200	−202	−189	−210
$\kappa/(W\ m^{-1}K^{-1})$	2.25	2.03	1.71	2.15	2.27	2.30
$L/(10^{-8}\ V^2K^{-2})$	1.63	1.63	1.62	1.62	1.61	1.64
$\kappa_L/(W\ m^{-1}K^{-1})$	1.57	1.44	1.22	1.64	1.54	1.92
$\mu/(cm^2V^{-1}s^{-1})*$	n/a	n/a	33	40	18	0.9
$n/(10^{19}\ cm^{-3})*$	n/a	n/a	6.9	6.8	14	220
ZT	0.67	0.67	0.71	0.60	0.71	0.48

Therein, κ_P is the measured thermal conductivity with a porosity P, and κ_0 the theoretical thermal conductivity at full density, i.e. $P = 0$. With porosities of 4% for the 0.3 Ge sample and 2% for the 0.4 Ge sample and setting $\beta = 2$ for spherical pores, we calculated κ_0 values of 1.9 W $m^{-1}K^{-1}$ and 2.3 W $m^{-1}K^{-1}$ at 773 K, respectively. Thusly, the different density cannot explain the large difference of 17% in κ alone; an additional explanation might be the possible existence of small amounts of unreacted Ge in the sample with the higher Ge amount, noting that elemental Ge has a thermal conductivity of the order of 60 W $m^{-1}K^{-1}$ (and that each measured κ value has an experimental error of the order of ±5%).

The lattice thermal conductivity, κ_L, was calculated through $\kappa_L = \kappa - \kappa_e$, where κ_e is the electronic thermal conductivity, which is derived from the measured electrical conductivity, σ, via the Wiedemann-Franz relationship $\kappa_e = L\sigma T$. The Lorenz numbers L were calculated by applying the single parabolic band and elastic carrier scattering approximation via Equation 4.2,

$$L = (\tfrac{k_B}{e})^2 \left\{ \frac{(1+\lambda)(3+\lambda)F_\lambda(\eta)F_{2+\lambda}(\eta)-(2+\lambda)^2 F_{1+\lambda}^2(\eta)}{(1+\lambda)^2 F_\lambda^2(\eta)} \right\} \qquad \text{Equation 4.2}$$

where $F_i(\eta)$ represents the Fermi integral of order i, the reduced Fermi energy (η) is equal to $E_F/(k_B T)$, where E_F is the Fermi energy, and it can be calculated as a function of temperature from measured values of the Seebeck coefficient using Equation 4.3. k_B is the Boltzmann constant and e the electron charge. Acoustical phonon scattering ($\lambda = 0$) can be assumed as the dominant factor limiting charge carrier mobility.[283]

$$S = \frac{k_B}{e}\left\{ \frac{(2+\lambda)F_{1+\lambda}(\eta)}{(1+\lambda)F_\lambda(\eta)} - \eta \right\} \qquad \text{Equation 4.3}$$

The calculated Lorenz numbers range from $L = 1.94 \times 10^{-8}$ $V^2 K^{-2}$ for the 0.1 Ge sample at 323 K to $L = 1.62 \times 10^{-8}$ $V^2 K^{-2}$ for the 0.4 Ge sample at 773 K, a complete list of all calculated values and their temperature dependence is shown in Figure 4.6. The calculated values for the lattice thermal conductivity are presented in Figure 4.7, which follow the same trends as the total thermal conductivity data. The lowest value of $\kappa_L = 1.2$ W m^{-1}K^{-1} occurs at 773 K for $Mg_2Si_{0.677}Ge_{0.3}Bi_{0.023}$.
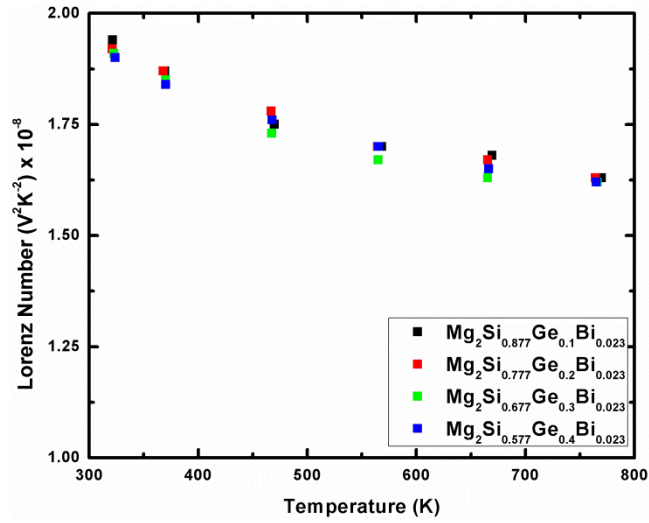
Figure 4.6   Calculated Lorenz number of $Mg_2Si_{0.977-x}Ge_xBi_{0.023}$ ($0.1 \leq x \leq 0.4$).
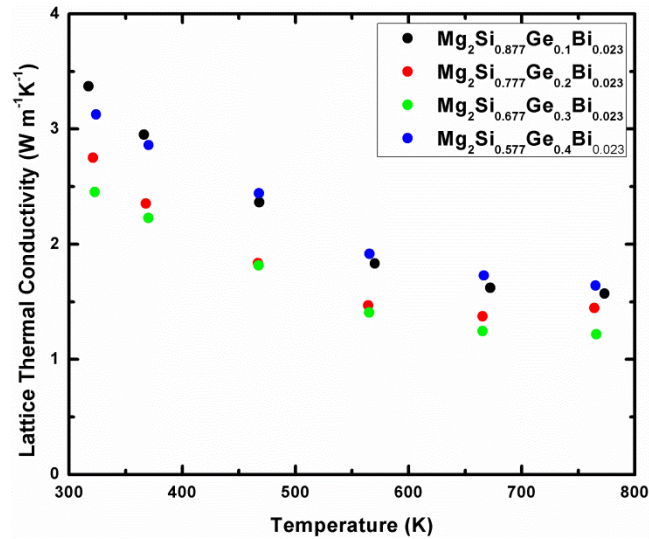
Figure 4.7   Lattice thermal conductivity of $Mg_2Si_{0.977-x}Ge_xBi_{0.023}$ ($0.1 \leq x \leq 0.4$).

The electrical conductivity data are shown in Figure 4.8. For all the samples, electrical conductivity increases with temperature up to around 500 K and then decreases. The reduction at higher temperature can be attributed to higher lattice vibration and an increase in acoustical phonon scattering via electron phonon interactions. Introducing germanium increases not only phonon scattering but also charge carrier scattering, which

results in a reduction in σ from 590 $\Omega^{-1}\text{cm}^{-1}$ (0.1 Ge) to 390 $\Omega^{-1}\text{cm}^{-1}$ (0.3 Ge) at room temperature. As was the case in the thermal conductivity data, the sample with 0.4 Ge stands out from this trend. Using again the Maxwell-Eucken correction (Equation 4.4) with $\beta = 2$, we find corrected values at 773 K for the hypothetical fully dense samples of 446 $\Omega^{-1}\text{cm}^{-1}$ instead of 396 $\Omega^{-1}\text{cm}^{-1}$ for the 0.3 Ge sample and of 437 $\Omega^{-1}\text{cm}^{-1}$ instead of 412 $\Omega^{-1}\text{cm}^{-1}$ for the 0.4 Ge sample. In contrast to the thermal conductivity, where the different porosities only explained part of the trend, the change in electrical conductivity from 0.3 to 0.4 Ge can thus be fully understood based on the decrease in porosity. This observation is in accord with the suspected trace amounts of unreacted Ge not increasing the electrical but the thermal conductivity.

$$\sigma_P = \sigma_0 \frac{1-P}{1+\beta P}$$
Equation 4.4

All the Bi doped samples presented here with values between $\sigma = 400$ $\Omega^{-1}\text{cm}^{-1}$ and 540 $\Omega^{-1}\text{cm}^{-1}$ at 773 K exhibit higher electrical conductivity than the one doped with Sb with $\sigma = 300$ $\Omega^{-1}\text{cm}^{-1}$, while Kim's $Mg_2Si_{0.7}Ge_{0.3}$:$Bi_{0.02}$ sample had higher electrical conductivity of $\sigma = 590$ $\Omega^{-1}\text{cm}^{-1}$ at 773 K (and smaller Seebeck coefficient) (Table 4.1).
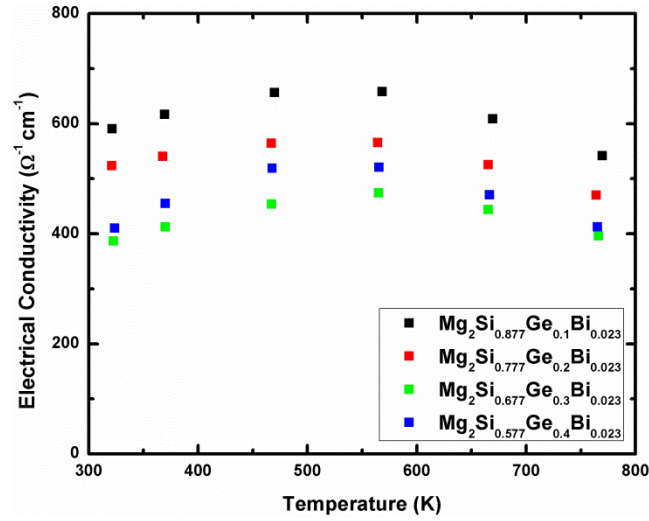
Figure 4.8   Electrical conductivity of $Mg_2Si_{0.977-x}Ge_xBi_{0.023}$ ($0.1 \leq x \leq 0.4$).

The reflectivity spectra of samples with 0.2 and 0.4 Ge are depicted in Figure 4.9. The dc conductivity values were calculated from the Kramers-Kronig analysis using the Drude model to be 170 $\Omega^{-1}cm^{-1}$ for the sample with 0.2 Ge and 99 $\Omega^{-1}cm^{-1}$ for 0.4 Ge. These calculated values are drastically lower than the ones measured on the pressed pellets via four point-probe measurements, and the reason or the discrepancy is most likely due to the limited spot size (about 400 μm^2) and penetration depth of the infrared radiation. The result of these instrumental limitations is that the signal used to extract the dc conductivity values is overly influenced by the character of the surface states.

One of the characteristics of a doped semiconductor is the plasma reflection edge, which is seen as a minimum in the reflectivity. Based on the Drude model, the corresponding energy at the reflectivity minimum is related to the plasma frequency, ω_P, which can be expressed as $\omega_P^2 = ne^2\varepsilon^{-1}m^{*-1}$, where n, m^* and ε are carrier concentration, effective mass and dielectric constant of the material, respectively.[276] We obtained a plasma frequency of 1460 cm^{-1} for 0.2 Ge sample, and 1165 cm^{-1} for 0.4 Ge, corresponding to energies of 0.18 eV and 0.14 eV, respectively. Earlier we reported 0.21 eV for $Mg_2Si_{0.98}Bi_{0.02}$.[116] The different values for the two Ge samples are likely caused by a different effect mass (thus mobility), as the nominal dopant concentrations are equivalent. Higher frequency/energy correlates with

74

lower effective mass, thus higher mobility, in accord with the higher room temperature conductivity of the 0.2 Ge sample as compared to 0.4 Ge.
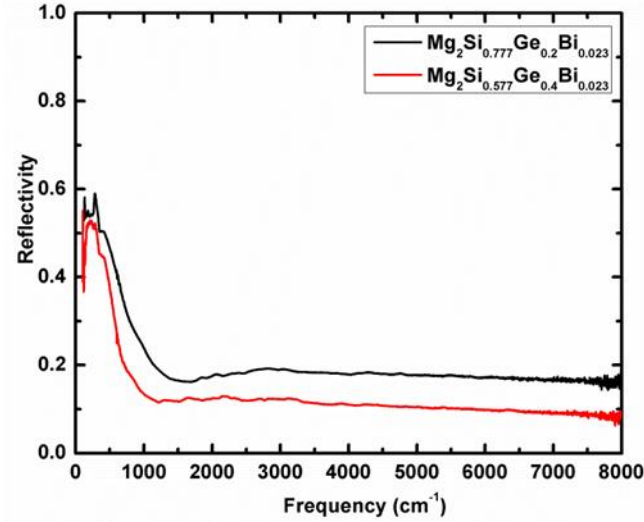
Figure 4.9   Reflectivity spectra of $Mg_2Si_{0.977-x}Ge_xBi_{0.023}$ (x = 0.2, 0.4).

To gain more understanding of the transport properties, Hall measurements were carried out on the samples with high Ge content (0.3 and 0.4 Ge per formula unit). The carrier concentrations (n) of both samples are nearly the same, $n \sim 7 \times 10^{19}$ per cm^3, consistent with them both having the same doping level, and are both nearly temperature independent (Figure 4.10). Interestingly, these concentrations are significantly lower than the one determined by Kim et al. on $Mg_2Si_{0.7}Ge_{0.3}$:$Bi_{0.02}$ (1.4×10^{20} cm^{-3}), which is also consistent with their higher electrical conductivity and lower Seebeck coefficient.[158] The different carrier concentration may be a consequence of the lower temperature and pressure used in the consolidation process, which might have resulted in less efficient Bi doping. For example, 0.023 Bi per formula unit would hypothetically add 3.6×10^{20} electrons per cm^3, while we found only 6.9×10^{19} cm^{-3}, compared to Kim's 1.4×10^{20} cm^{-3}. On the other hand, Kim's Sb-doped sample exhibited an unexplained high carrier concentration of 22×10^{20} cm^{-3}, i.e. 6 times higher than expected based on the nominal composition.
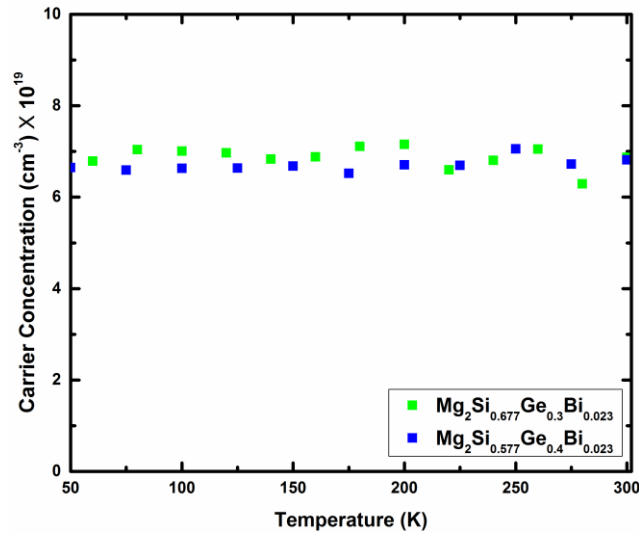
Figure 4.10 Carrier concentration of $Mg_2Si_{0.977-x}Ge_xBi_{0.023}$ (x = 0.3, 0.4).

Figure 4.11 shows an increase in the mobility (μ) of both samples with temperature. This temperature dependence of the mobility was also observed in Sb-doped Mg_2Si, where this effect was attributed to an activated process, which originated from the presence of MgO at the grain boundaries.[198] The increasing mobility at constant carrier concentration (as measured up to 300 K) causes the electrical conductivity to increase up to about 500 K. The slightly higher mobility of the sample containing 0.4 Ge per formula unit, e.g. $\mu = 40$ cm^{2}V^{-1}s^{-1} vs. 33 cm^{2}V^{-1}s^{-1} for 0.3 Ge at 300 K, is most likely a consequence of the higher relative density as above-mentioned. Kim's $Mg_2Si_{0.7}Ge_{0.3}{:}Bi_{0.02}$ exhibited only $\mu = 18$ cm^{2}V^{-1}s^{-1},[158] likely caused by the higher carrier concentration.
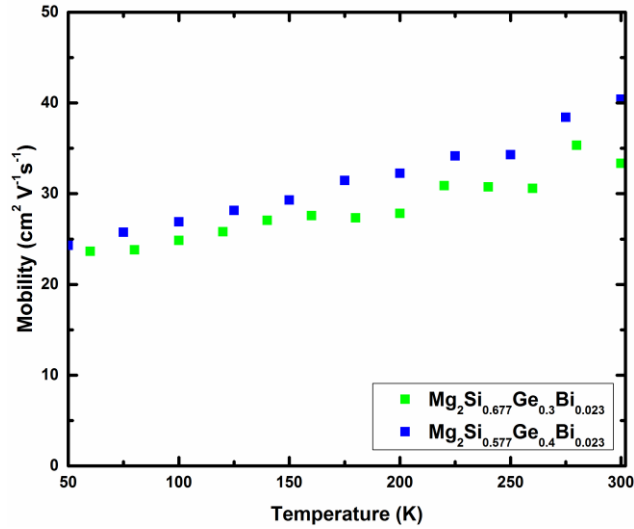
Figure 4.11   Hall mobility of $Mg_2Si_{0.977-x}Ge_xBi_{0.023}$ (x = 0.3, 0.4).

The Seebeck coefficient as a function of temperature for all the samples is shown in Figure 4.12. Replacing one Si atom with one Bi will add one electron per atom to the system, which results in a negative Seebeck coefficient. The room temperature Seebeck coefficient is around $S = -100$ µV K^{-1} for all the Bi-doped samples investigated here, in accord with the similar slope of the DOS around the Fermi level, and similar carrier concentration for at least the 0.3 Ge and 0.4 Ge samples. The S increases with temperature reaching a maximum value of -200 µV K^{-1} at 773 K behavior typical for a degenerate semiconductor.
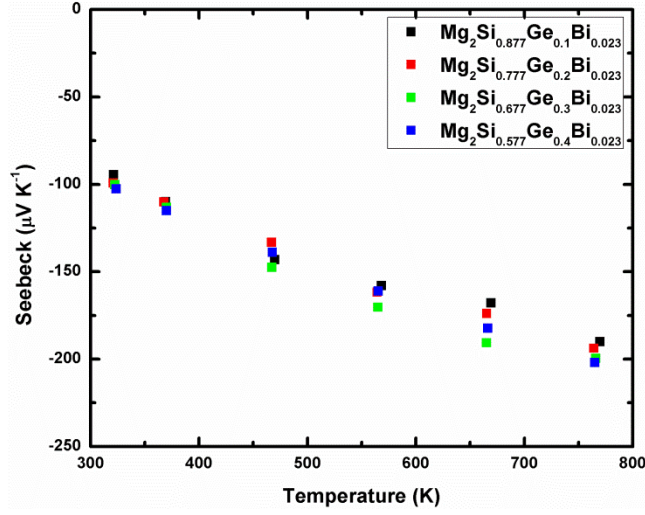
Figure 4.12   Seebeck coefficient of $Mg_2Si_{0.977-x}Ge_xBi_{0.023}$ ($0.1 \leq x \leq 0.4$).

The similarities of all Seebeck coefficient values also indicate that the carrier concentrations are nearly the same for all the samples. Assuming energy-independent scattering and carriers from a single parabolic band, we calculated the effective mass from the Seebeck coefficient and the carrier concentration via Equation 4.5,

$$S = \frac{8\pi^2 k_B^2}{3eh^2} m^* T \left(\frac{\pi}{3n}\right)^{2/3} \qquad \text{Equation 4.5}$$

with k_B = Boltzmann constant, h = Planck constant. We obtained $m^* = 0.83\ m_e$ for 0.3 Ge and $m^* = 0.85\ m_e$ for 0.4 Ge (m_e = electron mass). Effective mass values on the order of m_e are common for n-type Mg_2Si materials: for example, Kim et al. found $m^* = 1.1\ m_e$ for $Mg_2Si_{0.7}Ge_{0.3}$:$Bi_{0.02}$.[158]

The thermoelectric figure of merit ZT was calculated from the data discussed above, and compared to Kim's $Mg_2Si_{0.7}Ge_{0.3}$:$Bi_{0.02}$ and $Mg_2Si_{0.7}Ge_{0.3}$:$Sb_{0.02}$ (Figure 4.13). In each case, ZT increases with increasing temperature, and the $Mg_2Si_{0.677}Ge_{0.3}Bi_{0.023}$ sample culminates in the highest value of 0.7 at 773 K. This ZT_{max} value is around 50% higher than the $ZT = 0.48$ of its Sb-doped counterpart. The $Mg_2Si_{0.677}Ge_{0.3}Bi_{0.023}$ sample is also superior

to $Mg_2Si_{0.7}Ge_{0.3}:Bi_{0.02}$ over the entire temperature range with the exception of our last data point at 773 K, where both 0.3 Ge samples equally exhibit $ZT = 0.71$: the averaged ZT values over the measured temperature range are $ZT_{ave} = 0.35$ for $Mg_2Si_{0.677}Ge_{0.3}Bi_{0.023}$ and 0.30 for $Mg_2Si_{0.7}Ge_{0.3}:Bi_{0.02}$.[158]
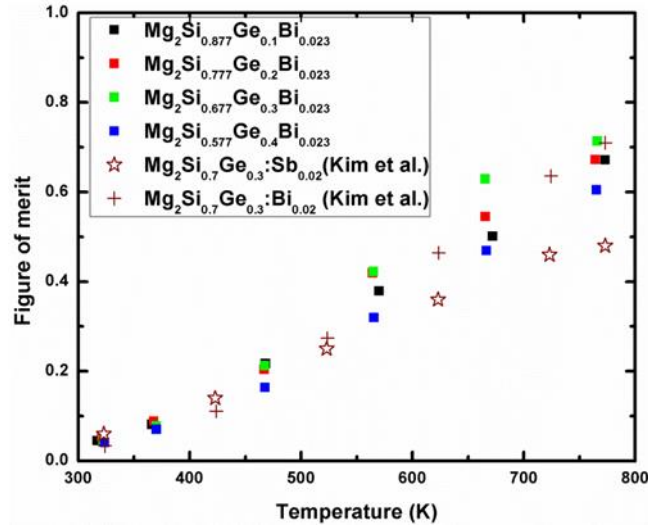
Figure 4.13   Figure of merit of $Mg_2Si_{0.977-x}Ge_xBi_{0.023}$ $(0.1 \leq x \leq 0.4)$.

4.4 Conclusion

By adding germanium to Mg_2Si doped with Bi, the thermal conductivity of alloyed magnesium silicide was reduced from about $\kappa > 7$ W m^{-1}K^{-1} down to values below 4 W m^{-1}K^{-1} at room temperature. The lowest κ was obtained for $Mg_2Si_{0.677}Ge_{0.3}Bi_{0.023}$ with a value of 1.7 W m^{-1}K^{-1} at 773 K, and a lattice thermal conductivity of $\kappa_L = 1.2$ W m^{-1}K^{-1}. TEM results indicate interstitial sites partly occupied with Mg as well as the presence of Ge-rich domains within the $Mg_2(Si,Ge,Bi)$ particles, which further contribute to a lower thermal conductivity in addition to the alloying effect/increased mass fluctuation. A significant decrease in the electrical conductivity also occurred with increasing Ge content, but the net effect to the thermoelectric figure of merit is positive.

79

All in all, bismuth appears to be a more effective dopant than antimony in this system, reflected in a significant enhancement (~48% higher) of the thermoelectric figure of merit *ZT* at 773 K, compared to Kim's Sb-doped sample. The same trend exists between Kim's Bi- and Sb-doped samples, which were both prepared by the same methods (though different than ours, as above-mentioned).

Further optimization can be performed on this system by changing the doping level, the pressing conditions, adding tin and studying the effect of nano-structuring, e.g. via ball milling or forming composites.

Chapter 5

Effect of MWCNT Inclusion on Thermoelectric properties of $Mg_2Si_{0.877}Ge_{0.1}Bi_{0.023}$

5.1 Introduction

Carbon nanotubes, due to their spectacular electronic properties and robustness, can be considered as potential candidates for nano-inclusions in thermoelectric materials.[284–288] Even though CNTs had a positive effect on the thermoelectric properties of Bi_2Te_3 [289] and $Bi_2(Se,Te)_3$ [290] by achieving $ZT \sim 1.5$ at 350 K as compared to $ZT \sim 1$ for the sample without nanotubes, the presence of rare and toxic tellurium would not fulfill the criteria for large scale industrial applications, further the temperature at which these materials are most efficient are well below those of most targeted waste heat recovery applications. The goal of this chapter is to demonstrate the effect of CNTs on the thermoelectric properties of more cost effective and eco-friendly materials. Magnesium silicide based materials, in this regard, are conspicuous as next generation high efficiency TE materials that are suitable for auto industry applications.[291].Thus far, single-wall carbon nanohorns (SWCNH),[137] TiO_2 [292] and Si nanoparticles[293] were studied as nano-inclusions in Mg_2Si materials. The lack of similar investigations of $Mg_2Si_{1-x}Ge_x$ solid solutions motivated this study.

5.2 Experimental Section

$Mg_2Si_{0.877}Ge_{0.1}Bi_{0.023}$ samples were synthesized by the method discussed in Chapter 4. All samples were pure except for small traces of MgO (Figure 5.1), which is a common side product in Mg_2Si based compounds.[68,274] The powders were manually mixed and divided into four batches. Different amount of carbon nanotubes (Sigma-Aldrich, Carbon nanotube, multi-walled; >90% MWCNT basis, outer diameter 10 - 15 nm, inner diameter 2 - 6 nm, length 0.1 - 10 μm) were then added to each batch and mixed for 3 to 5 minutes using a Fisher Scientific vortex mixer until no MWCNT agglomerations were detected.
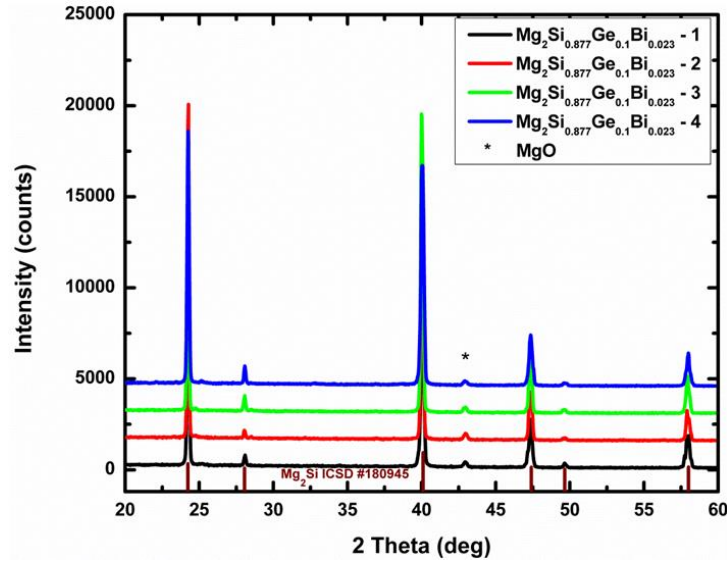
Figure 5.1   Powder XRD patterns of $Mg_2Si_{0.877}Ge_{0.1}Bi_{0.023}$ samples.

To verify the existence and examine the distribution of nanotubes within the samples at the micron level, scanning electron microscopy (SEM) analysis was performed on parts of selected pressed pellets (Figure 5.2) the nanotubes are totally visible in the picture with a fibre like shape. All other preparation and measurement methods such as hall effect, hot pressing, electrical resistivity and thermal diffusivity are similar to the ones discussed in previous chapters. The obtained densities together with the calculated specific heat of all the samples for calculating thermal conductivity, κ, are available in Table 5.1. Our previous measurements of the specific heat of $Mg_2Si_{0.977-x}Ge_xBi_{0.023}$ samples validated the accuracy of Dulong-Petit approximation for this system.[294] Since adding CNT only changed the Dulong-Petit value of C_p by 2%, within the error range of the measurement, the calculated values were used to obtain the thermal conductivity. Theoretical densities of the composite (d_C) were calculated using the mixture rule (Equation 5.1).

$$\frac{1}{d_C} = \frac{w_{MWCNT}}{d_{MWCNT}} + \frac{w_{Matrix}}{d_{Matrix}}$$

Equation 5.1

Table 5.1　　Densities and specific heat of the $Mg_2Si_{0.877}Ge_{0.1}Bi_{0.023}$/MWCNT samples.

Sample	Density (g cm^{-3})	Relative density	C_p (J g^{-1}K^{-1})
$Mg_2Si_{0.877}Ge_{0.1}Bi_{0.023}$	2.10	96%	0.877
$Mg_2Si_{0.877}Ge_{0.1}Bi_{0.023}$ - 0.5 wt.-% MWCNT	2.10	96%	0.882
$Mg_2Si_{0.877}Ge_{0.1}Bi_{0.023}$ - 1.0 wt.-% MWCNT	2.04	93%	0.888
$Mg_2Si_{0.877}Ge_{0.1}Bi_{0.023}$ - 1.5 wt.-% MWCNT	2.06	94%	0.894
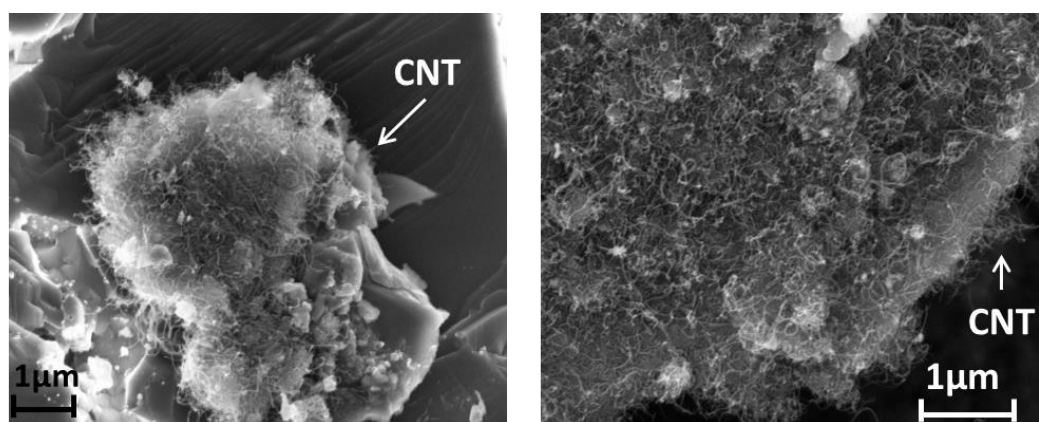
Figure 5.2　　SEM images of the $Mg_2Si_{0.877}Ge_{0.1}Bi_{0.023}$/1 wt.-% MWCNT sample.

5.2.1 Raman spectroscopy

Dispersive Raman microscope (Renishaw Invia Raman Microscope) equipped with a Fourier transform infrared (FTIR) detector for sequential analysis at the same spot was used to measure pure multi-wall carbon nanotube and $Mg_2Si_{0.877}Ge_{0.1}Bi_{0.023}$ samples with additions of 0.5%, 1%, and 1.5% weight-% MWCNTs. The Raman spectroscopy was operated with a 514 nm argon ion laser (Modu-Laser Stellar Pro laser) and a 1800 line/mm grating. The laser power used was 10%, yielding 0.36 mW at the sample. The laser was focus on the flatten powder sample using a 20× objective, and the Raman signal was collected at 10 s. The measurement was calibrated by using Si (110), which was measured at 520 cm^{-1}. Data

processing and analysis were accomplished using software Wire 3.4 (Renishaw, Inc.). The collection wave number range for Raman spectrum was from 100 cm^{-1} to 2000 cm^{-1}.

5.3 Results and Discussion

From EDX mapping, we deduce that the additions of Ge and Bi are not localized in the form of precipitates, but are present in the form of a solid solution in the Mg$_2$Si matrix. Figure 5.3 illustrates EDX elemental mapping carried out over a selected region (the pink box) within the grain with Ge (red) and Bi (green) color coded maps. Atomic-level characterization work was carried out to confirm this as discussed later. The elemental maps corresponding to Ge (red) and Bi (green) indicate that the Ge and Bi atoms are alloyed with the Mg$_2$Si matrix in the form of solid solution. Low-magnification STEM imaging as shown in Figure 5.4a revealed the polycrystalline nature of the sample with larger grain sizes (< 12 μm). In addition, the grain-boundaries can be seen as brighter as compared to the bulk of the grain. The brighter intensities are consistent with the segregation of elements with higher Z (in this case, Ge and/or Bi). EDX mapping performed on the area highlighted as a rectangle, i.e. including three different grains and their grain boundaries, revealed a mostly homogenous presence of Mg, Si, and Bi within the grains, while Ge was accumulated along the grain boundaries, but with higher concentration in some of the grains (the top grain in the particular case shown in the map of Figure 5.4). To further analyze this, additional line scans were performed, as highlighted on the left of Figure 5.4b and Figure 5.4c. Going from the left grain to the bottom grain (Figure 5.4b), the Ge concentration peaked in the boundary between these two. On the other hand, the line scan from the top to the bottom grain (Figure 5.4c) revealed a higher Ge concentration in the top grain, while Bi stayed constant within error of the method.
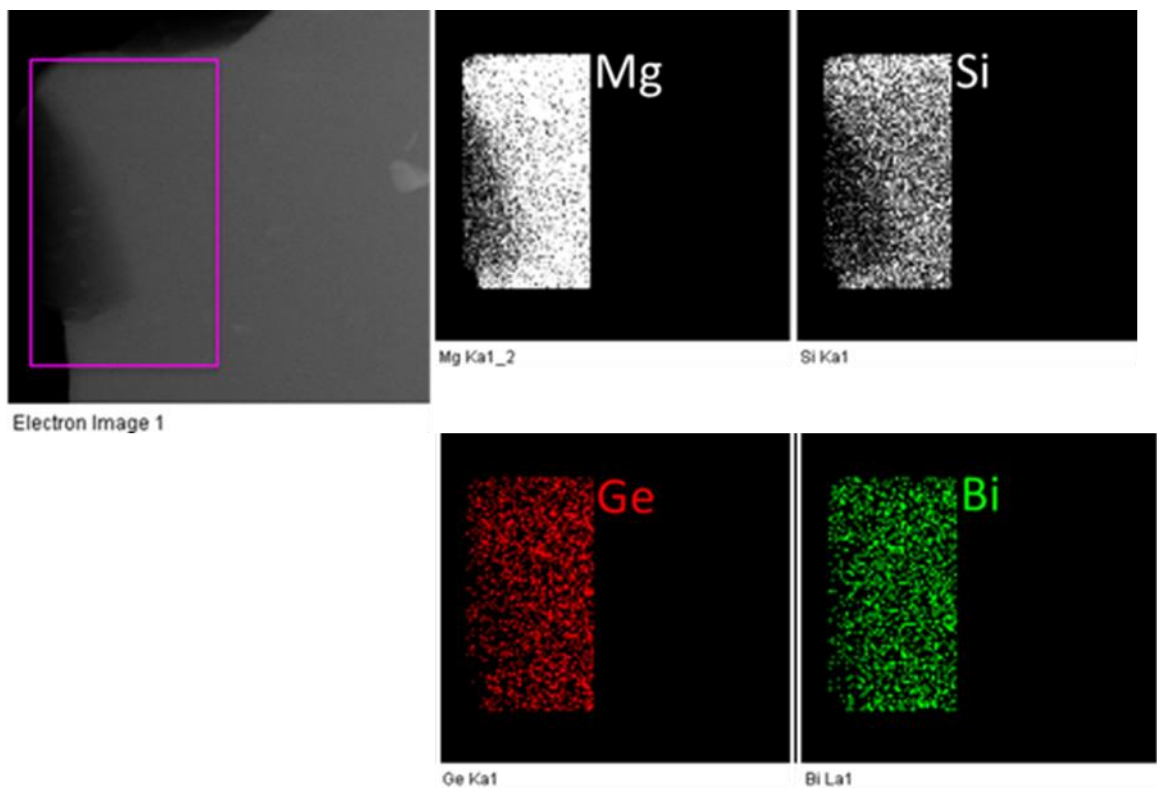
Figure 5.3   Low-magnification structural (STEM-HAADF imaging) and compositional (EDX elemental mapping) analyses of a selected region within a grain. EDX elemental mapping shows the distribution of Mg, Si, Ge and Bi.
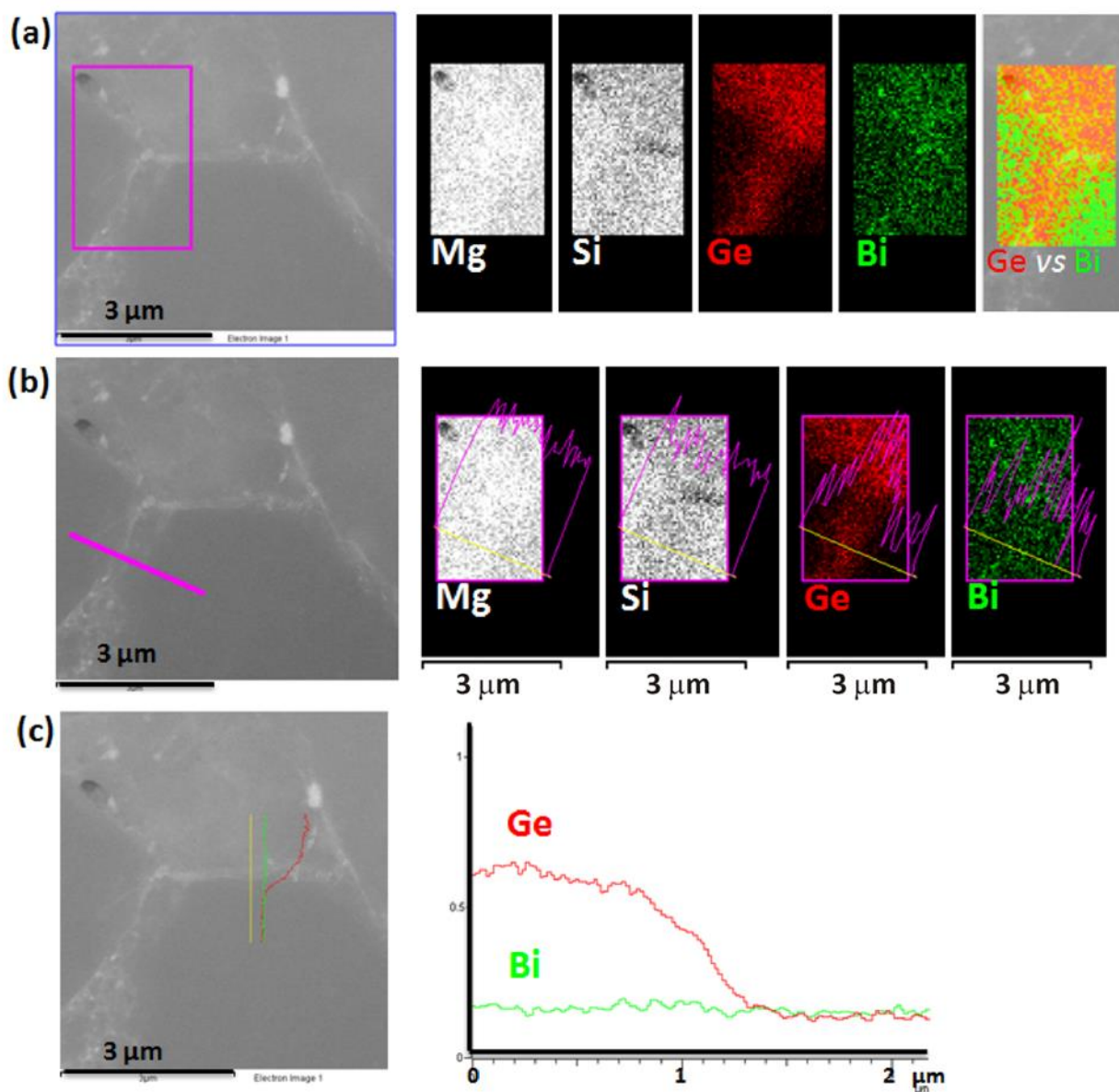
Figure 5.4   (a) Left: low-magnification STEM-HAADF image; right: EDX elemental maps of Mg, Si, Ge and Bi in the area marked with a rectangle; (b), (c) line profiles of Ge-K and Bi-L lines along the boundary between different grains. The profiles in red and green correspond to Ge and Bi, respectively.

The low-magnification STEM-HAADF image shown in Figure 5.5a illustrates an area along the edge of the specimen. The Kikuchi diffraction patterns obtained on two

different spots (Figure 5.5b and Figure 5.5c) confirm the presence of two grains with different orientations and, hence, a grain boundary at the interface. In fact, the grain boundary is visible as a bright stripe midway between the spots where the Kikuchi patterns are obtained. EDX line scans were performed for Ge and Bi as shown in the Figure 5.5d and Figure 5.5e to examine the distribution of heavy elements. From the line profile of Ge, it is evident that Ge is segregating along the grain boundary, consistent with the findings discussed above. Again in contrast to Ge, the EDX intensity in the line profile of Bi does not reveal any such segregation, but possibly slightly different concentrations in the two grains. The apparent large width of the Ge segregation profile (Figure 5.5e) can be explained by the fact that, in this particular region and sample tilt, the grain boundary might not be perfectly parallel to the electron beam. The segregation of Ge at the grain boundaries together with the homogenous distribution of Bi in the grain boundaries could be helpful in blocking the phonons while allowing the electrons to pass. To obtain better statistics, other grain boundaries were analyzed (not shown), and were found to be consistent over all observed ones. Compared to our earlier work (Mg_2Si with Bi and no Ge), the Bi atoms were found to extensively segregate along the grain boundaries.[116,294] Here the segregation, if at all present, would be very small compared to the previously studied samples. This implies that it is possible to tune the segregation/distribution behaviors of dopants by increasing the unit cell through alloying.

87
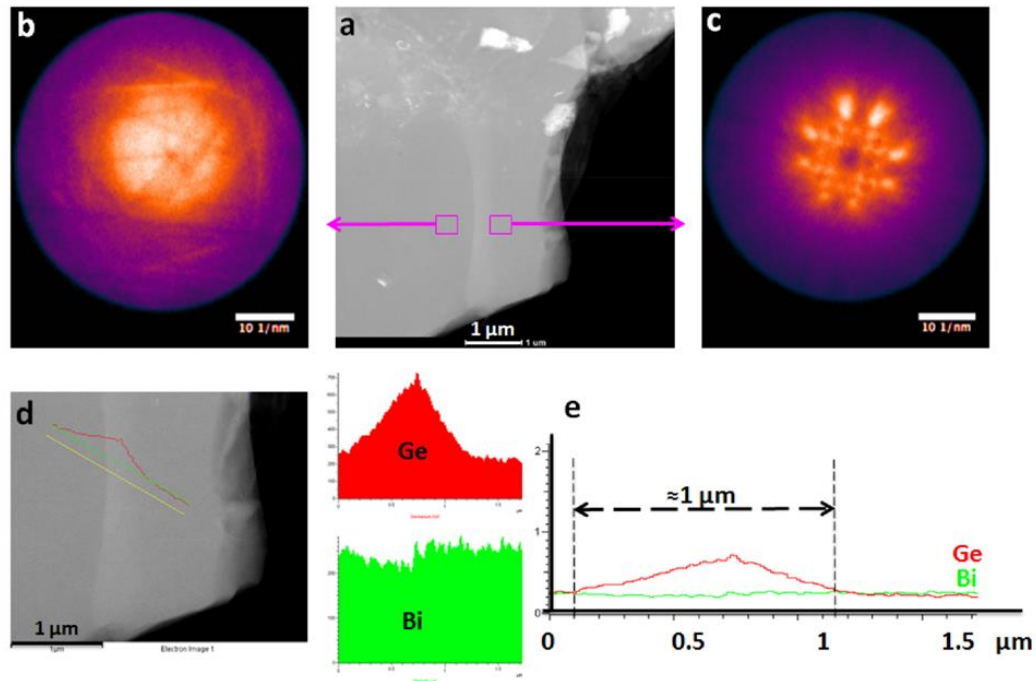
Figure 5.5   Low-magnification STEM-HAADF image; (b) and (c) Kikuchi patterns confirming two different grains separated by a grain boundary; (d) EDX line scans of Ge-K (red) and Bi-L (green) lines along the grain boundary; (e) line profiles of Ge (red) and Bi (green) along the grain boundary as shown in (d).

In addition to EDX line scans as well as low-magnification imaging illustrated above, the distribution of dopants within a grain was understood better using STEM-HAADF imaging performed at an atomic resolution, as shown in Figure 5.6a. For better visibility, a selected region is magnified and shown in Figure 3b. Individual atomic columns of the doped Mg_2Si lattice, oriented along the [111] zone axis, are visible in Figure 5.6b. In these Z-contrast imaging conditions, the brighter atomic columns on the image (identified with pink arrows) are distributed randomly over the entire 2-D projection of the lattice, and contain heavier elements such as Ge and Bi, which are located on substitutional sites replacing Si atoms.[116,140] It is clear that the dopant atoms are rather homogenously distributed within the bulk of the grain. Figure 5.6c illustrates this in much better clarity where a site with

88

significantly brighter intensity (pink arrow) can be clearly seen in proximity to another site with relatively weaker intensity (green arrow).
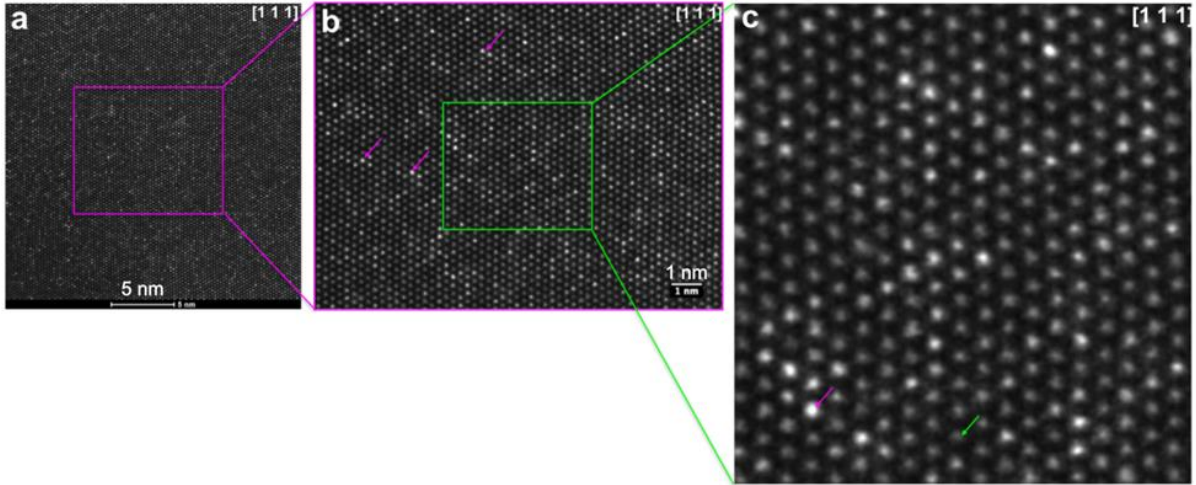
Figure 5.6   (a) and (b) Atomic resolution STEM-HAADF images corresponding to a region in the bulk of a grain oriented along [111] zone axis; (c) magnified region from (b), the green arrow indicating an atomic column with no significant brighter intensities as compared to the atomic column highlighted by the pink arrow.

Raman spectra of $Mg_2Si_{0.877}Ge_{0.1}Bi_{0.023}$ with different amounts of MWCNT are shown in Figure 5.7. The pure MWCNT was also measured as the reference. As can be seen, all the samples demonstrate the higher frequency D mode (disordered) and G mode[295,296] at around 1350 cm^{-1} and 1590 cm^{-1}, respectively. No shift is observed in the D and G bands, which indicates the CNTs neither decomposed under pressure used for consolidation nor reacted with the base material. Although the regular breathing mode is specific to CNT, we cannot observe this mode for multi-wall carbon nanotube due to the larger strains of multi wall nanotubes, which hinder its vibration along the radial direction compared to the single wall carbon nanotubes.[297]
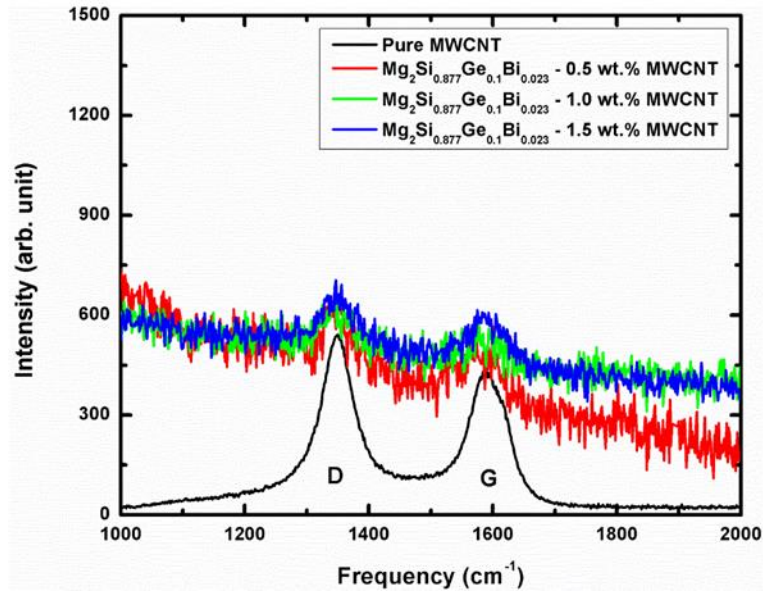
Figure 5.7   Raman spectra of the $Mg_2Si_{0.877}Ge_{0.1}Bi_{0.023}$/MWCNT samples.

The electrical conductivity of all the nanocomposites is shown in Figure 5.8. For all samples, the electrical conductivity increases with temperature below 600 K and then decreases due to an increase in electron-phonon interaction, which dominates charge carrier scattering at higher temperature. Adding multi wall carbon nanotubes increases the electrical conductivity from $\sigma = 450 \ \Omega^{-1}cm^{-1}$ for the sample without MWCNT to 500 $\Omega^{-1}cm^{-1}$ for the sample containing 0.5 weight-% MWCNT at 323 K.
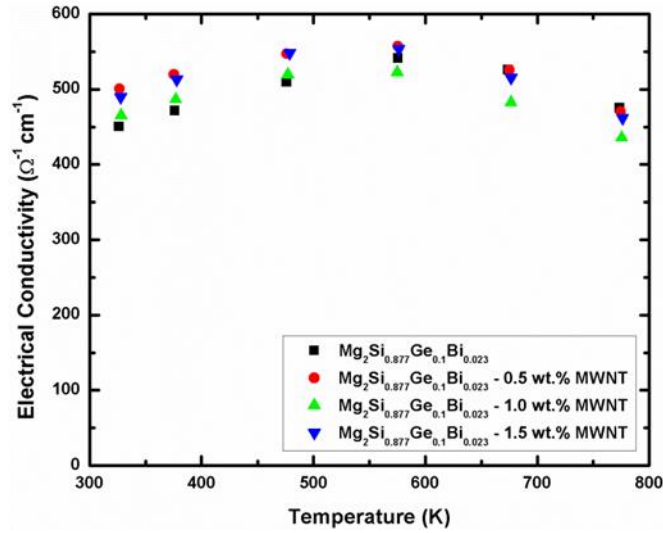
Figure 5.8   Electrical conductivity of the $Mg_2Si_{0.877}Ge_{0.1}Bi_{0.023}$/MWCNT samples.

The main reason for the increased electrical conductivity is due to the increase in n (Figure 5.9), since the mobility (μ_H) (Figure 5.10) of all the samples is very similar. The sample containing 0.5 wt.% MWCNT shows the highest carrier concentration on average below 300 K with the maximum value of around 8.4×10^{19} per cm^3 at 280 K. Although increasing the amount of carbon nanotubes slightly decreases the carrier concentration, the undoped sample exhibits the lowest on average. The mobility of all samples increases with temperatures, which could be due to the existence of MgO at the grain boundaries, which dominates the grain boundary scattering at lower temperature[116] as also observed in Sb-doped Mg_2Si.[198]

A comparison between different Bi-doped Mg_2Si nanocomposites is given in Table 5.2. The 0.5 wt.-% MWCNT sample shows an electrical conductivity of $\sigma = 470$ $\Omega^{-1}cm^{-1}$ at 773 K, which is in between the SWCNH and the Si nanoparticle composite samples with $\sigma = 312$ $\Omega^{-1}cm^{-1}$ and 658 $\Omega^{-1}cm^{-1}$, respectively.
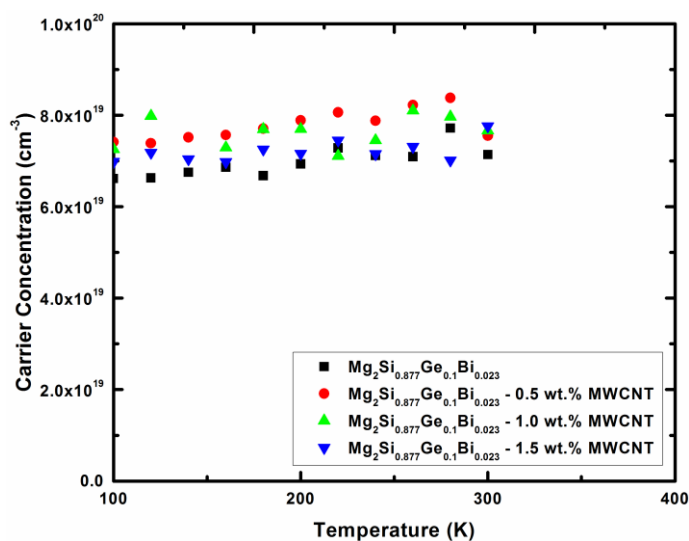
Figure 5.9   Room temperature carrier concentration of the $Mg_2Si_{0.877}Ge_{0.1}Bi_{0.023}$/MWCNT samples.
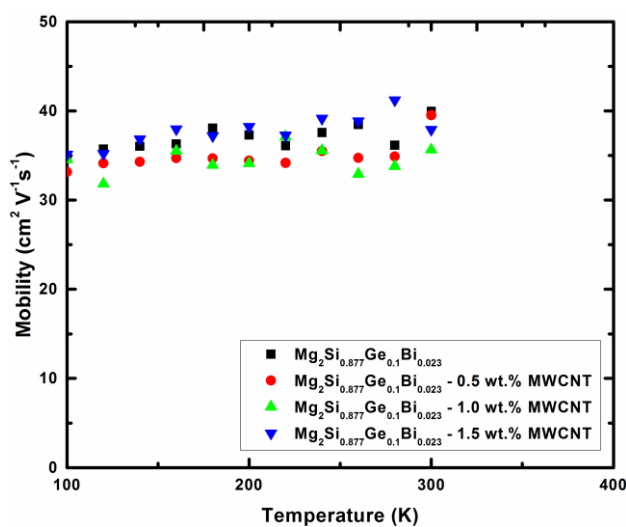
Figure 5.10   Low temperature Hall mobility of the $Mg_2Si_{0.877}Ge_{0.1}Bi_{0.023}$/MWCNT samples.

The main difference between the electrical conductivity of the MWCNT-containing sample and the one containing Si nanoparticles is due to the 50 percent higher carrier concentration of 11.7×10^{19} per cm^3 of the latter.

Table 5.2   Thermoelectric properties of $Mg_2Si_{0.877}Ge_{0.1}Bi_{0.023}$/0.5% MWCNT at 773 K in comparison to other Mg_2Si-based nanocomposites.

	$Mg_2Si_{0.877}Ge_{0.1}Bi_{0.023}$ / 0.5% MWCNT	$Mg_2Si:Bi_{0.02}$ / SWCNH [137]	Mg_2Si / 2.5 mol% $Si_{1\%Bi}$ [293]
$\sigma/(\Omega^{-1}cm^{-1})$	470	312	658
$S/(\mu V\ K^{-1})$	−200	−216	−204
$\kappa/(W\ m^{-1}K^{-1})$	2.2	3.4	3.1
$L/(10^{-8}\ V^2K^{-2})$	1.6	2.5	2.2
$\kappa_L/(W\ m^{-1}K^{-1})$	1.6	2.9	2.0
$\mu/(cm^2V^{-1}s^{-1})$ [300 K]	40	n/a	13
$n/(10^{19}\ cm^{-3})$ [300 K]	7.6	n/a	11.7
ZT	0.67	0.32	0.67

Figure 5.11 exhibits the temperature dependence of the Seebeck coefficient. All the composites show a negative Seebeck value, indicative of electrons as the major charge carriers. The Seebeck value is around $S = -100\ \mu V\ K^{-1}$ at 323 K in every case, and it increases with increasing temperature. For the samples containing MWCNT, the increase is more noticeable, at 773 K with $S = -200\ \mu V\ K^{-1}$ for the 0.5 wt.-% MWCNT composite compared to $S = -180\ \mu V\ K^{-1}$ for the pristine sample. Thus, adding MWCNT resulted in an enhancement in Seebeck coefficient while maintaining the electrical conductivity. This phenomenon was also observed in $(Bi_{0.2}Sb_{0.8})_2Te_3$/MWCNT nanocomposites,[290] and can be attributed to the energy filtering of the low energy charge carriers,[298–301] which is a common phenomenon in nanocomposites due to the nanophase-matrix interface.[302] On the other hand, the SWCNH sample has a slightly higher (absolute) Seebeck coefficient ($S = -215\ \mu V\ K^{-1}$), which is related to its noticeably low electrical conductivity (Table 5.2).
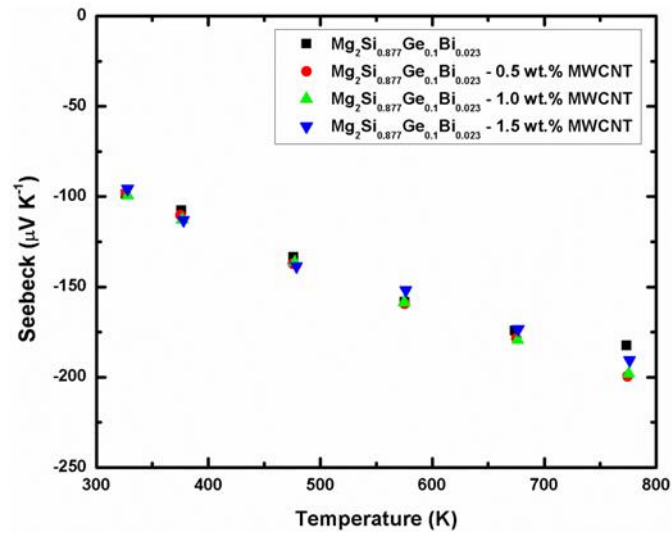
Figure 5.11   Seebeck coefficient of the $Mg_2Si_{0.877}Ge_{0.1}Bi_{0.023}$/MWCNT samples.

The capability of a thermoelectric material to generate electrical power is measured by the power factor, *P.F.* = $S^2\sigma$, which is demonstrated in Figure 5.12. The power factor of all samples starts around 5 μW cm^{-1}K^{-2} at 323 K and increases with temperature. Except for the pristine sample, which reaches its maximum power factor of roughly 16 μW cm^{-1}K^{-2} at around 673 K, all the nanocomposites show their highest value at around 773 K, with the 0.5 wt.-% MWCNT sample attaining ~ 19 μW cm^{-1}K^{-2}. Obtaining higher power factors would lead to higher output power density which makes the material more suitable for practical use.[303]
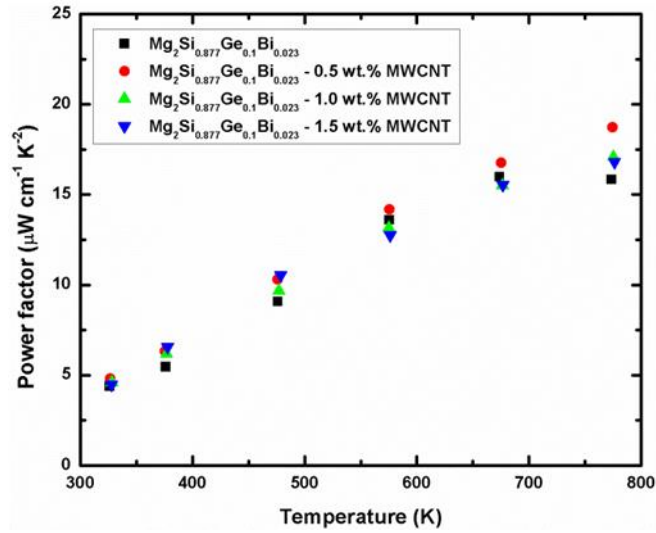
Figure 5.12 Power factor of MWCNT/Mg$_2$Si$_{0.877}$Ge$_{0.1}$Bi$_{0.023}$ samples.

Figure 5.13 shows the thermal conductivity of all nanocomposites studied in this work, which was calculated based on the measured thermal diffusivity data. Because of the dominant acoustic phonon scattering, the thermal conductivity of all samples decreases with increasing temperature. The 1.5 wt.-% MWCNT sample demonstrates the lowest thermal conductivity of 2.07 W m^{-1}K^{-1}, which is substantially lower than that of the samples containing SWCNH and Si nanoparticle composites. This reduction in thermal conductivity can come from the combination of having both Ge and MWCNT in the sample. Since the thermal conductivity of MWCNT is increasing with temperature,[304] the propitious effect of MWCNT on thermal conductivity of nanocomposites is more dominant in the medium temperature range (Figure 5.14).
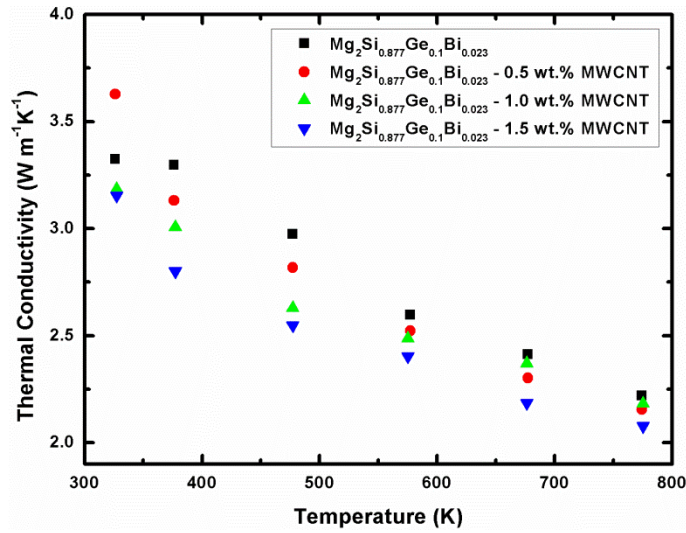
Figure 5.13   Thermal conductivity of the $Mg_2Si_{0.877}Ge_{0.1}Bi_{0.023}$/MWCNT samples.
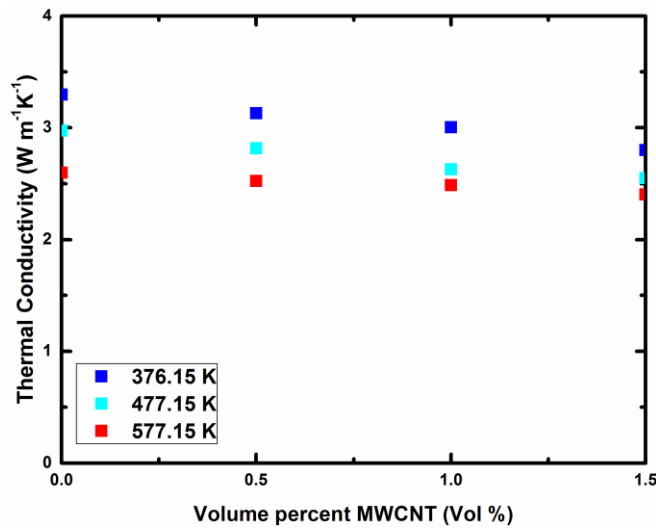
Figure 5.14   Medium temperature thermal conductivity of all samples with respect to MWCNT content.

The electronic thermal conductivity, κ_e, was calculated by applying the Wiedemann-Franz law $\kappa_e = L\sigma T$. The Lorenz numbers, L, that were used in calculating κ_e are shown in Figure S5 and were obtained from Equation 4.2 by utilizing the single parabolic band and elastic carrier scattering estimation. The electronic thermal conductivity of all samples is

nearly the same and it increases approximately from 0.3 W $m^{-1}K^{-1}$ at 323 K to 0.6 W $m^{-1}K^{-1}$ at 773 K, which leads us to the conclusion that the reduction in thermal conductivity is chiefly coming from changes in the lattice contribution (Figure 5.15). The sample containing 1.5 wt.-% MWCNT depicts the lowest lattice thermal conductivity of 1.49 W $m^{-1}K^{-1}$ at 773 K, compared to 2.85 W $m^{-1}K^{-1}$ and 2.0 W $m^{-1}K^{-1}$ determined for the SWCNH and Si nanoparticle composites, respectively.
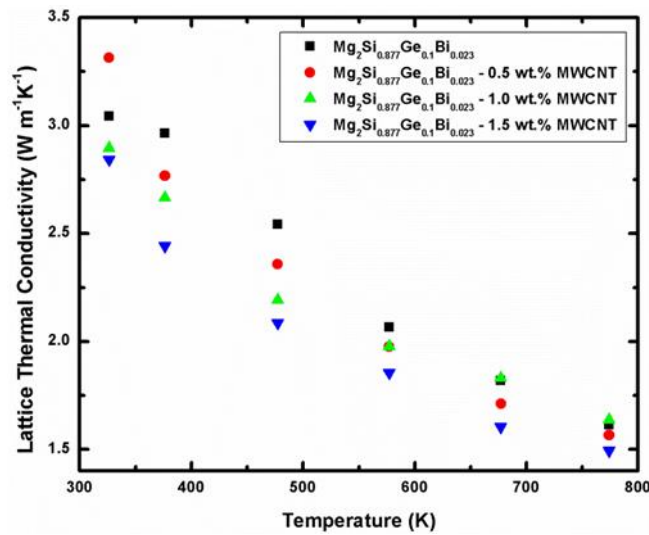
Figure 5.15   Lattice thermal conductivity of the $Mg_2Si_{0.877}Ge_{0.1}Bi_{0.023}$/MWCNT samples.

After measuring all the thermoelectric properties, the thermoelectric figure of merit *ZT* was computed (Figure 5.16). The *ZT* of all composites increases with increasing temperature. While all the nanocomposites show higher *ZT* than the pristine sample, the 0.5 wt.-% MWCNT sample reaches a maximum value of *ZT* = 0.67 at 773 K among all MWCNT. This matches *ZT* of the Si nanoparticle counterpart, and is more than twice of what was achieved for the Bi doped SWCNH composites.
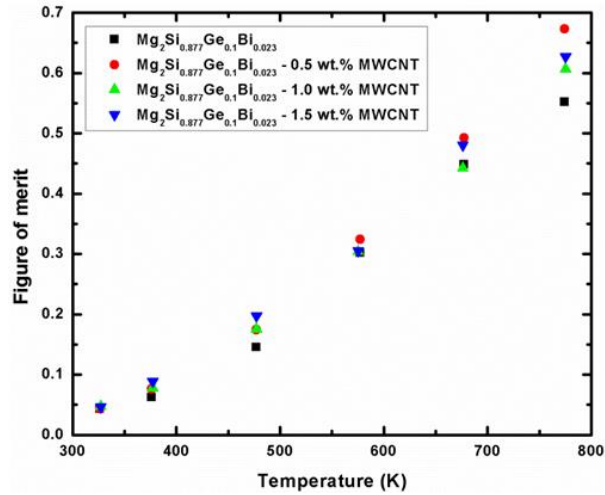
Figure 5.16 Figure of merit of the $Mg_2Si_{0.877}Ge_{0.1}Bi_{0.023}$/MWCNT samples.

One of the main issues in thermoelectric nanocomposites research is the homogeneity of the distributed nano phase in the matrix and its effect on the properties of the nanocomposites. To examine the reliability of the presented data, a second bar was cut from a different part of the 0.5 wt.-% MWCNT pellet, and the obtained power factor (Figure 5.17) is equal within experimental error.
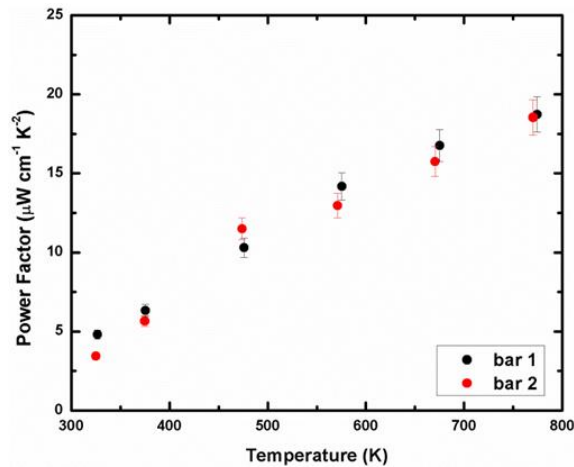
Figure 5.17 Power factor of two bars obtained from 0.5% MWCNT/$Mg_2Si_{0.877}Ge_{0.1}Bi_{0.023}$ nanocomposite (6% error is considered).

5.4 Conclusion

Atomic resolution imaging and EDX analyses on $Mg_2Si_{0.877}Ge_{0.1}Bi_{0.023}$/0.5 wt.-% MWCNT sample revealed a rather homogenous distribution of Ge and Bi in the bulk of the grains, although Ge partially segregates along the grain boundaries. With Z-contrast imaging, we have shown the random distribution in solid solution of Bi and Ge atoms in the Mg_2Si lattice ultimately leading to local lattice distortions of the lattice due to size effects. The inclusion of multi-wall carbon nanotubes into $Mg_2Si_{0.877}Ge_{0.1}Bi_{0.023}$ matrix at low concentration not only maintained the high temperature electrical conductivity, but also led to a 10% improvement of the high temperature Seebeck coefficient, which could be due to energy filtering that originated from the $Mg_2Si_{0.877}Ge_{0.1}Bi_{0.023}$ - MWCNT matrix interfaces.

Although the existence of MWCNT enhanced phonon scattering especially at medium temperature lowered the lattice thermal conductivity, this reduction is compensated at higher temperature due to the thermal transport behavior of MWCNT. The positive effect of MWCNT on thermoelectric properties of $Mg_2Si_{0.877}Ge_{0.1}Bi_{0.023}$ is manifested by the enhanced thermoelectric figure of merit, ZT, with all the nanocomposites achieving higher ZT values than the pristine sample. The highest improvement of more than 20% belongs to the sample containing 0.5 wt.-% MWCNT with its ZT of 0.67 at 773 K. Comparing with the other nano inclusions that were applied to Mg_2Si based thermoelectrics, MWCNT exhibited the most promising effect on TE properties, and further development may be implemented through adding tin or in situ nano-structuring via ball milling.

Chapter 6

Effect of SiC Nano-inclusion on Thermoelectric properties of Mg$_2$Si$_{0.676}$Ge$_{0.3}$Bi$_{0.024}$

6.1 Introduction

The effect of silicon carbide (SiC) nanoparticles on the thermoelectric properties of Mg$_2$Si$_{0.676}$Ge$_{0.3}$Bi$_{0.024}$ is described in the following chapter. Although bulk SiC has high room temperature thermal conductivity,[305–307] adding small amounts of SiC nanoparticles reduced the thermal conductivity of Bi$_{0.5}$Sb$_{1.5}$Te$_3$, Bi$_2$Te$_{2.7}$Se$_{0.3}$,[308] and Bi$_2$Te$_3$.[309] With this contribution, we discuss – for the first time – the effect of SiC nanoparticles on the thermoelectric properties of Mg$_2$Si based materials, here with 0.3 Ge per formula unit, as that resulted in the best performance in our previous study.[140] To the best of the authors' knowledge, no studies of nanocomposites with Mg$_2$Si$_{1-x}$Ge$_x$ solid solutions are known except for our previous multi wall carbon nanotube composites,[310] which inspired us to perform this investigation.

6.2 Experimental Methods

The detailed Mg$_2$Si$_{0.676}$Ge$_{0.3}$Bi$_{0.024}$ synthesis conditions were described in Chapter 4. The synthesized samples were ground into powders, manually mixed and then divided into four batches. Different amounts of silicon carbide (SiC) nanoparticles (Alfa Aesar, β modification, 45 nm - 55 nm) were added to each batch and mixed for 3 to 5 minutes using a Fisher Scientific vortex mixer until no SiC nanoparticle agglomerations were observed. Small traces of MgO were observed in powder X-ray diffraction patterns (Figure 6.1), which is a typical side product in Mg$_2$Si based compounds.[68] The measured densities together with the calculated specific heat of all the samples are available in Table 6.1. Theoretical densities of the composite (d_C) were calculated using the mixture rule (Equation 5.1). The accuracy of Dulong-Petit approximation on the specific heat of the bismuth doped Mg$_2$Si$_{1-x}$Ge$_x$ system was confirmed in our previous study.[140] Since adding SiC nanoparticles only changed the

specific heat by less than 1%, which is within the error range of the measurement, the calculated values of specific heat from Dulong-Petit approximation were applied to obtain the thermal conductivity. All the procedures for samples consolidation and measurements are the same as the ones discussed in previous chapters.
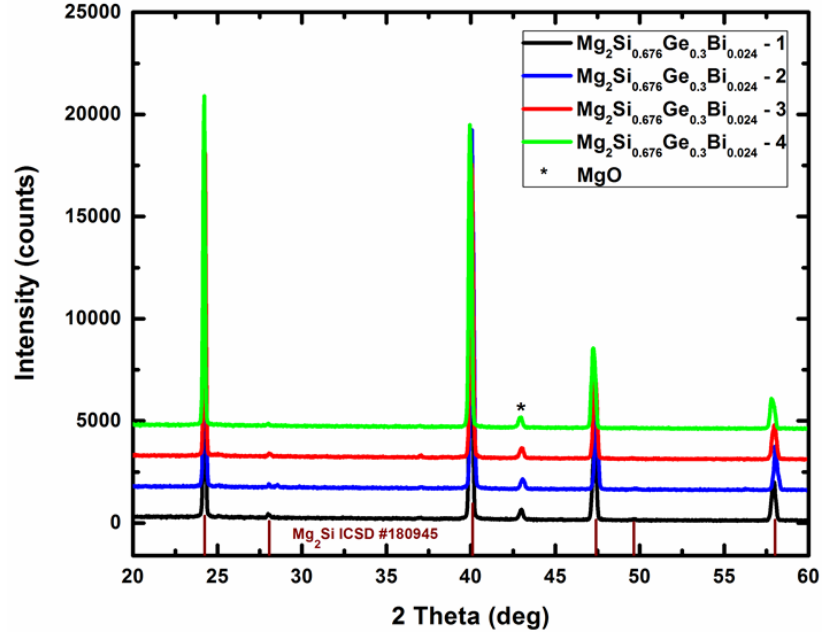
Figure 6.1   Powder XRD patterns of the four $Mg_2Si_{0.676}Ge_{0.3}Bi_{0.024}$ samples prior to combining them.

Table 6.1   Densities and specific heat of $Mg_2Si_{0.676}Ge_{0.3}Bi_{0.024}$/SiC nanocomposites.

Sample	Density Archimedes (g cm^{-3})	Theoretical density	C_p
$Mg_2Si_{0.676}Ge_{0.3}Bi_{0.024}$	2.32	94%	0.793
$Mg_2Si_{0.676}Ge_{0.3}Bi_{0.024}$/0.5 wt.-% SiC	2.33	94%	0.794
$Mg_2Si_{0.676}Ge_{0.3}Bi_{0.024}$/1.0 wt.-% SiC	2.33	94%	0.796
$Mg_2Si_{0.676}Ge_{0.3}Bi_{0.024}$/1.5 wt.-% SiC	2.31	93%	0.799

6.3 Results and Discussion

The polycrystalline nature of the sample with grain sizes larger than 10 μm is depicted in Low-magnification STEM imaging (Figure 6.2a). The selected three grains for analyses are identified as 1, 2 and 3, and the Kikuchi patterns (Figure 6.2b) obtained from these grains further confirmed that the grains are oriented differently. In contrast to the bulk of the grain, grain boundaries (identified by green arrow) demonstrated brighter intensities which could be related to different composition between the bulk of the grain and the grain boundary.
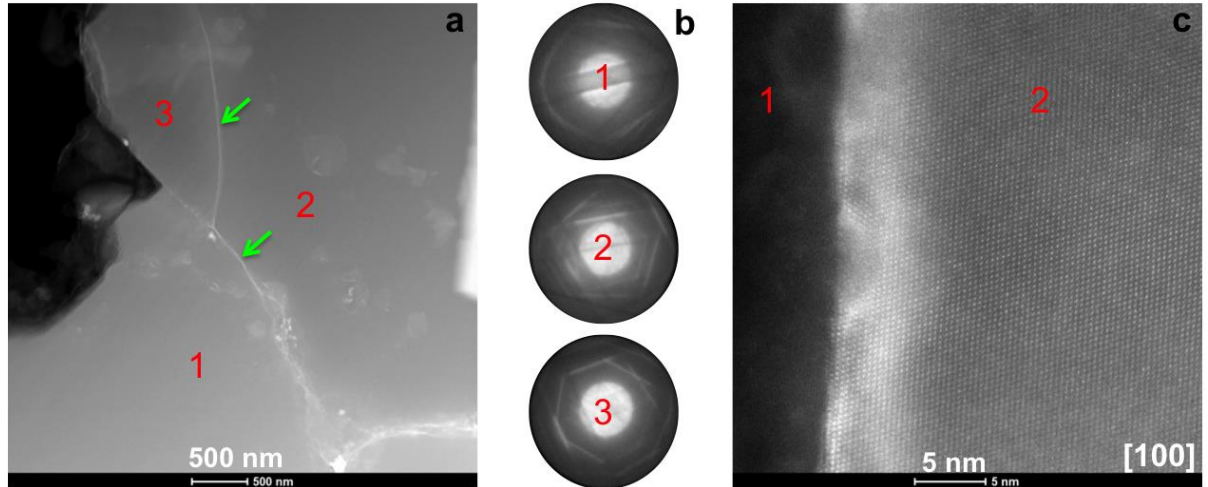
Figure 6.2   a) Low magnification STEM-HAADF image of three selected grains in the polished sample; b) Kikuchi patterns corresponding to grains 1, 2 and 3; c) atomic-resolution STEM-HAADF image of a boundary between the grains 1 and 2.The grain 2 is oriented along [100] zone-axis.

To shed more light on the distribution of the heavier elements (Ge, Bi) in both regions, detailed STEM-HAADF and EDX analyses were performed, and the characterization results are discussed in the following sections. The atomic-resolution STEM-HAADF image shown in Figure 6.2c corresponds to a region at the grain-boundary, separating grain 1 and grain 2 discussed in Figure 6.2a. The dots visible in the region

corresponding to grain 2 are individual atomic columns of the doped Mg_2Si lattice that is oriented along [100] zone-axis. It is evident that along the grain boundary, the intensities of these atomic-columns are stronger compared to those in the bulk of the grain (Figure 6.3). Considering the Z-dependence in these imaging conditions, we infer that the brightness of these columns stems from the Ge/Bi atoms located on the $4a$ Wyckoff site replacing Si atoms; as also deduced from the image simulations discussed in our earlier work.[310] Since the image intensity is sensitive to the precise location of the scattering atoms, the relative variation in the intensities within the columns indicates that these columns could contain single/multiple substitution of Ge/Bi atoms. Image simulations analyses were carried out to validate if the dopant segregation comes solely from Ge, Bi or their combination.
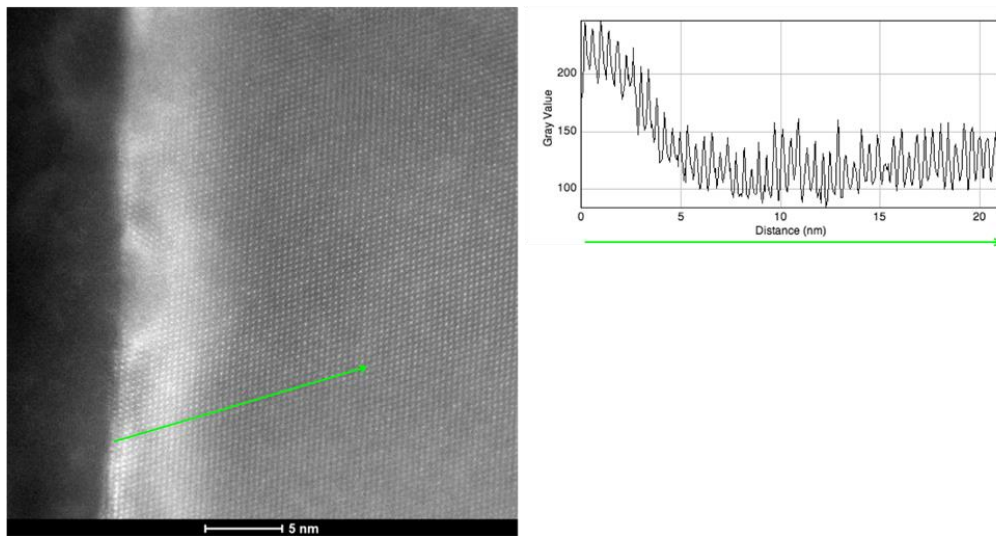
Figure 6.3   Line profile showing decreasing intensity from grain boundary to bulk.

In this respect, the multislice method was utilized to simulate STEM-HAADF images for a given crystalline lattice/supercell. To keep all the conditions of image formation identical, the supercell (Figure 6.4a) was constructed in a way that the intensity from atomic columns of (1) undoped Mg_2Si, (2) Si substituted with only Ge, (3) with only Bi, (4) with both Ge and Bi, can all be obtained from the same image. Two cases along the z direction

103

were formulated on the basis that the separation distance between Ge and Bi atoms are (1) farther (2 nm, Figure 6.4b) (2) closer (0.5 nm, Figure 6.4c).
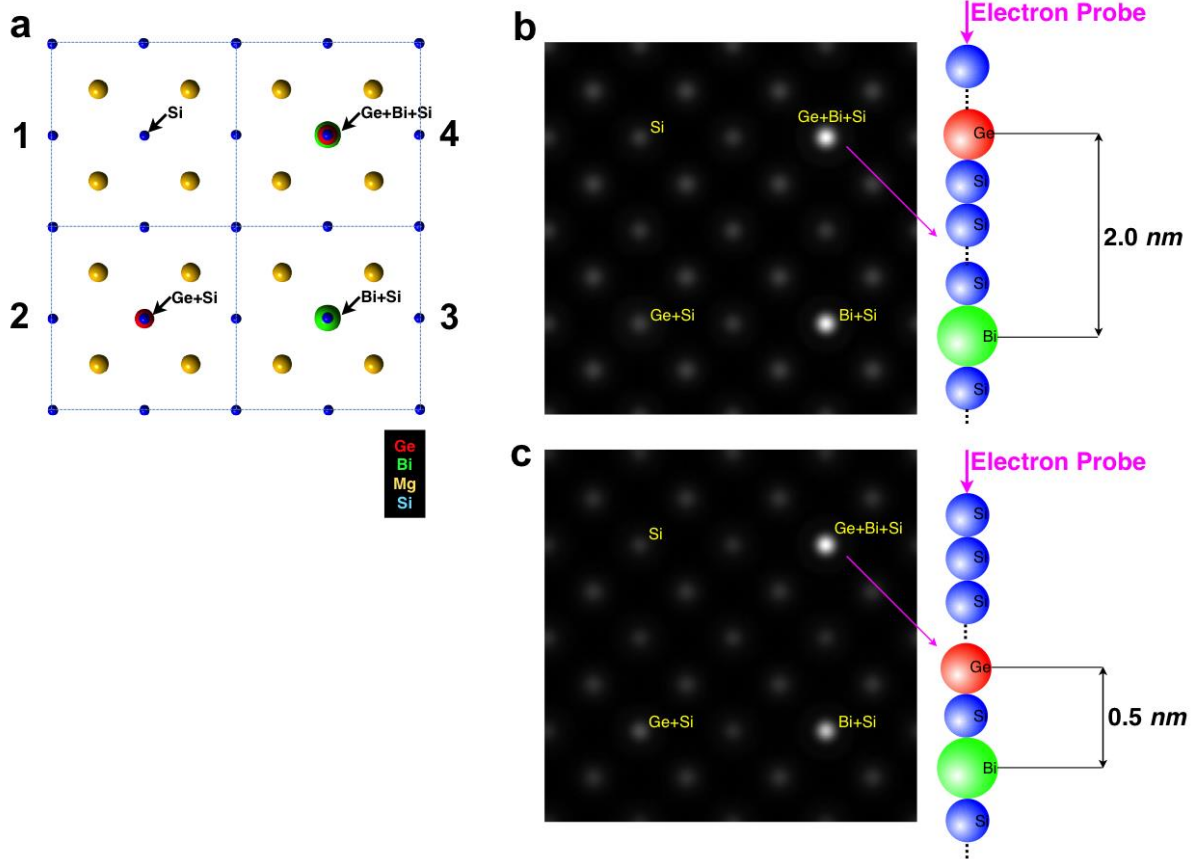
Figure 6.4   a) Schematic illustration of the super cell of Mg_2Si: (1) undoped; (2) substituted with only Ge; (3) only with Bi; (4) with a combination of Ge and Bi, along the z direction; b) simulated multislice images of the supercell for Ge-Bi separation distances of 2 nm; b) simulated multislice images of the supercell for Ge-Bi separation distances of 0.5 nm.

The location of Bi atoms was fixed to 20th position viewed from the surface, and Ge was varied between the 3rd and 12th position. The intensities obtained at each of the column locations corresponding to (1) to (4), are quantified for both conditions as shown in Figure 6.5a and Figure 6.5c. Evidently, the columns doped with only Bi appear with higher

integrated intensity compared to the one containing only Si and Ge. Proceeding further, the pure Ge and Bi intensities can also be extracted to calculate their contributions to the overall column intensity in the case of mix occupancy. The results are shown in Figure 6.5b and Figure 6.5d corresponding to Ge-Bi separation distances of 2 nm and 0.5 nm, respectively. It can be concluded that the contribution of Bi to the overall column intensity is significantly higher than Ge in both cases. This calculation offers high confidence to state that the grain boundary segregation observed is most likely due to Bi and not Ge.
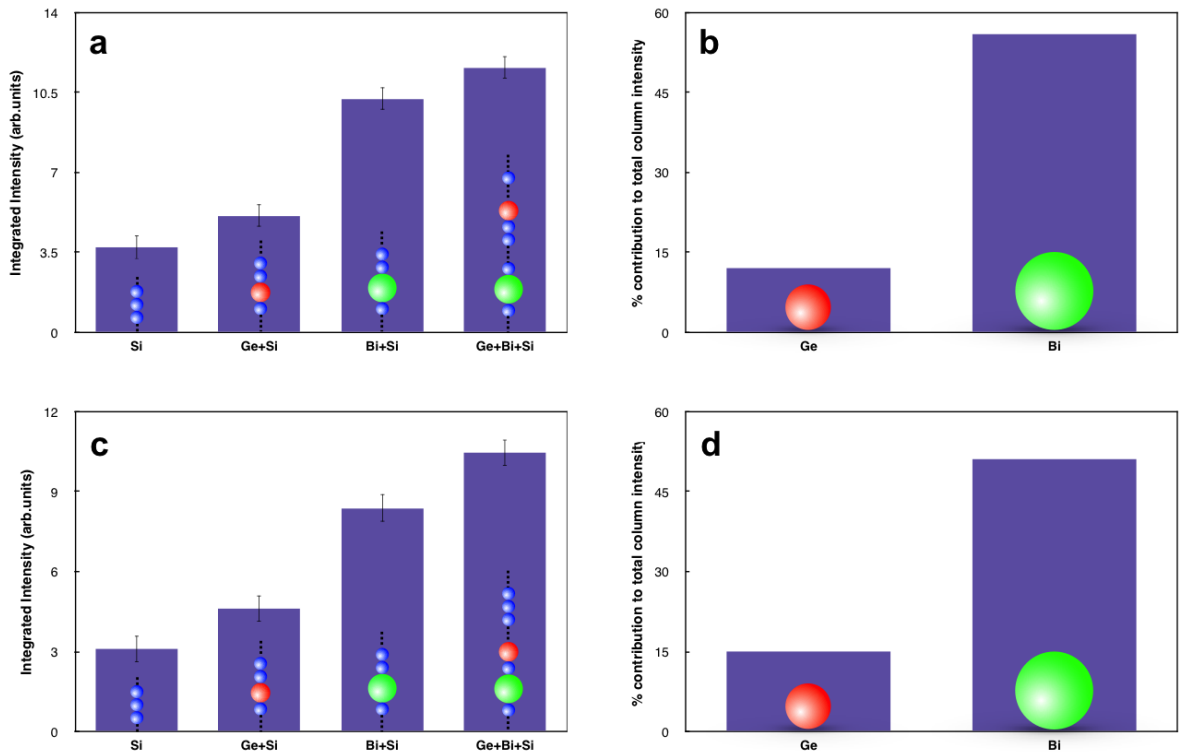
Figure 6.5   a) Integrated intensities for respective column compositions (from Figure 2, with Ge-Bi distance = 2 nm); b) relative contributions of Ge and Bi to the total column intensity in the case of the Ge/Bi mixed occupancy with Ge-Bi distance = 2 nm; c) integrated intensities for respective column compositions (from Figure 2, with Ge-Bi distance = 0.5 nm); d) relative contributions of Ge and Bi to the total column intensity in the case of the Ge/Bi mixed occupancy with Ge-Bi distance = 0.5 nm.

To better understand the intensity variation in the image with the position of Ge and Bi along the z direction in Mg_2Si unit cell (Figure 6.6a), a second set of simulations was carried out on Mg_2Si supercells consisting of $2 \times 1 \times 25$ repeats along the x, y and z directions, respectively (Figure 6.6b). The simulated images created for the supercell doped with Ge and Bi are shown in Figure 6.7a. The locations of Ge and Bi atoms in the x, y plane are identifiable in Figure 5a, and their z coordinate was varied from 1 to 25 in increments of 5. The intensities obtained from the simulated STEM-HAADF images correlated with atomic-columns containing Ge, Bi and Si-only sites were quantified. Consequently, the variation in the relative contribution of Ge and Bi to the total column intensity was calculated as a function of their location along the z direction, as illustrated in Figure 6.7b. Firstly, it can be seen that in all cases, the contribution of Bi remains significantly higher than that of Ge. Secondly, the plot also reveals that there are variations in these calculated values with respect to the lattice sites, corroborating with the fact that each column under an electron microscope is probed differently.
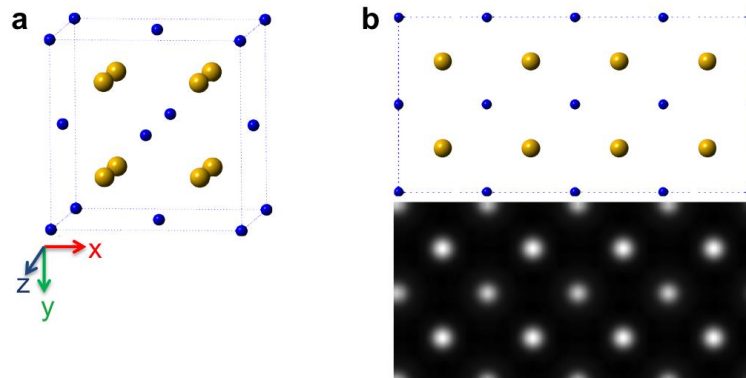
Figure 6.6   a) Schematic illustration of the Mg_2Si unit cell; b) simulated multislice image from the super cell of Mg_2Si (containing repeated unit cell $2 \times 1 \times 25$ times along the x, y, z directions.
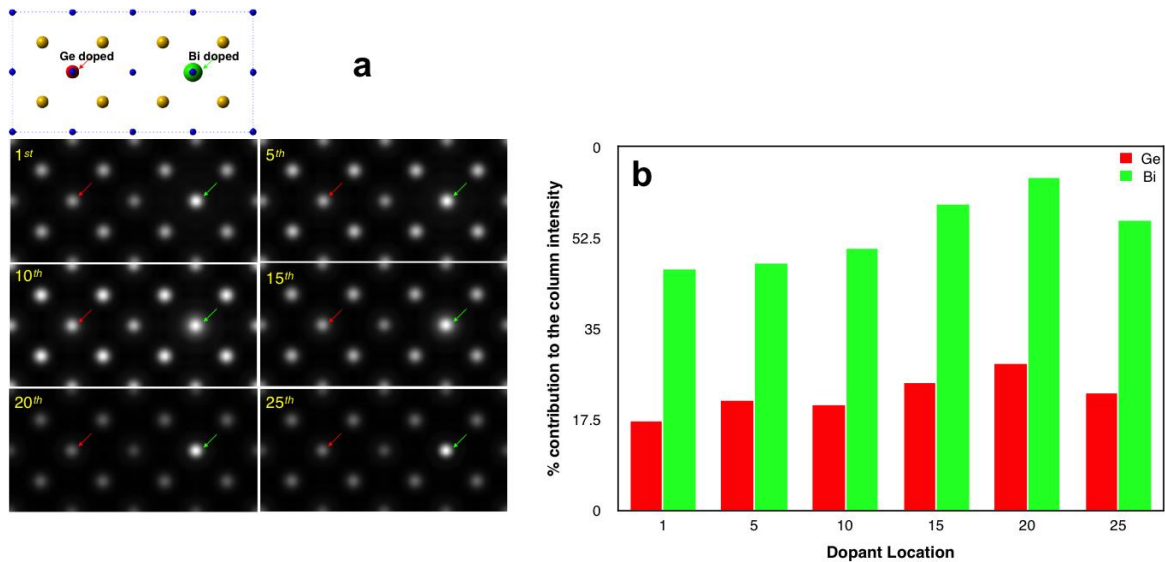
Figure 6.7   a) Simulated multislice image from the super cell ($2 \times 1 \times 25$ unit cell) of Mg$_2$Si substituted with Ge and Bi; with the locations of Ge and Bi identified by red and green arrows; b) the variation in relative contribution of Ge and Bi to the total column intensity as a function of dopant location along the z direction.

To confirm the above-postulated Bi segregation experimentally, alongside the STEM imaging discussed in Figure 6.2, we carried out elemental analyses via EDX. As shown in Figure 6.8, elemental line scans for Ge and Bi were performed across the grain boundary. The results indicate an accumulation of Bi along the grain boundary, but no clear Ge concentration changes. It is worth to mention that in contrast to this, a segregation of Ge was observed in MWCNTs samples,[310] which suggests the possibility of grain boundary engineering with respect to the type of nano-inclusion to manipulate the thermoelectric properties of the material. Finally, EDX spot analyses were carried out over a region within the three grains (1, 2 and 3) of Figure 1a to examine the elemental distributions in the bulk of the grain.
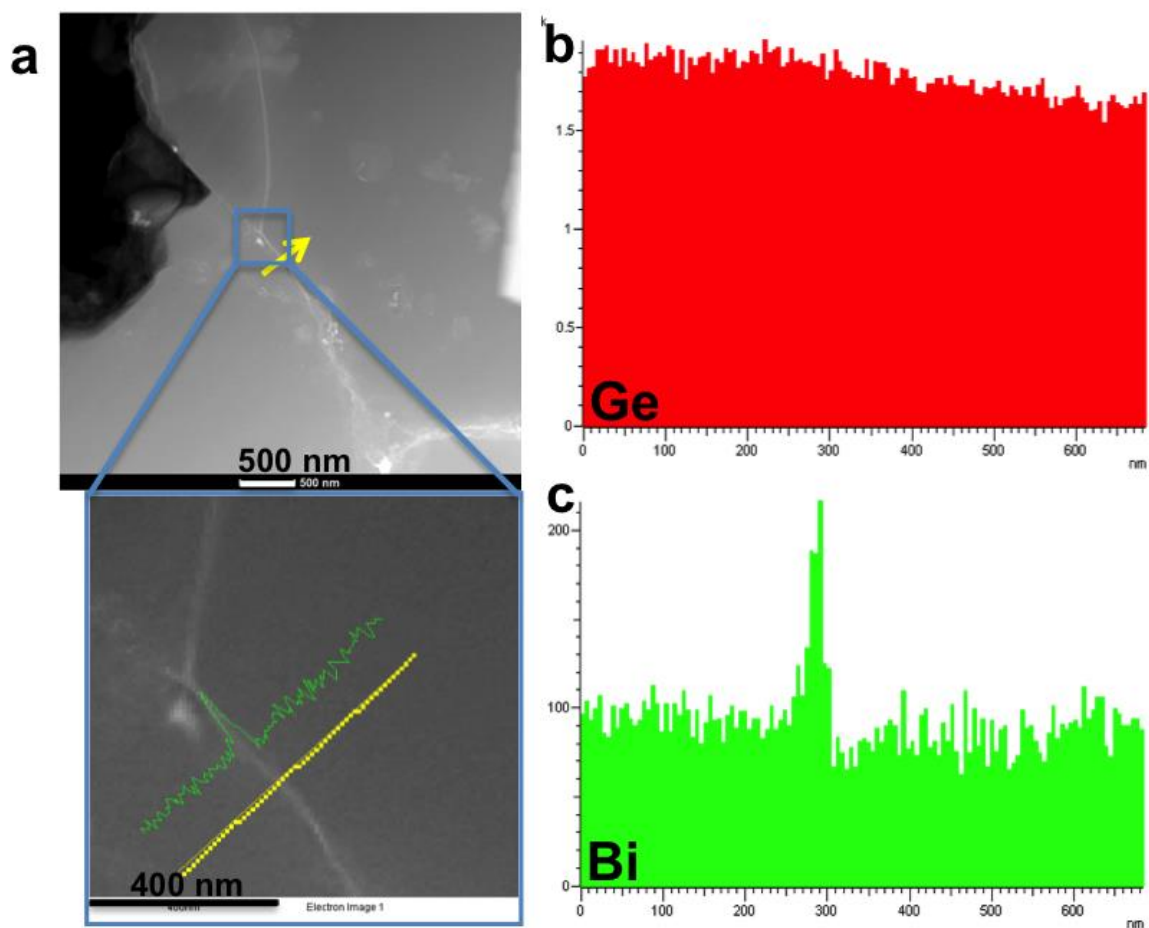
Figure 6.8   a) Low-magnification STEM-HAADF image with the magnified area of
interest for the line scan; b) elemental EDX line profile of Ge along the yellow line shown in
a); c) elemental EDX line profile of Bi.

The quantified results (Table 6.2) confirm the presence of Ge and Bi in the bulk of
the grain. Grain 1 seemed to be rich in Ge compared to the nominal Ge content; since Ge and
Bi are supposed to occupy the same site in the structure, the excess amount of Ge inside the
grain occurs with more Bi at the boundaries.

Table 6.2   EDX spot analyses for areas identified in Figure 6.2 within the grains in weight-%.

Grain	Mg	Si	Ge	Bi
1	47.3	15.0	31.6	6.2
2	51.0	20.1	23.2	5.8
3	50.6	19.4	24.7	5.3
Average	49.6	18.1	26.5	5.8
Nominal composition wt. %	51.6	20.2	23.2	5.3

The electrical conductivity of all $Mg_2Si_{0.676}Ge_{0.3}Bi_{0.024}$/SiC nanocomposites is shown in Figure 6.9. Adding SiC reduces the electrical conductivity in steps from 545 $\Omega^{-1}cm^{-1}$ to 420 $\Omega^{-1}cm^{-1}$ at 325 K. Although β-SiC has the smallest band gap of 2.4 eV among all other SiC polytypes,[306,307] such a consistent reduction was expected due to its insulating character. The difference between the electrical conductivity of the samples becomes less significant at higher temperatures, e.g. 395 $\Omega^{-1}cm^{-1}$ compared to 370 $\Omega^{-1}cm^{-1}$ at 773 K for the samples containing 0.5 wt.-% and 1.5 wt.-% SiC, respectively. All samples containing SiC exhibited less severe reduction in high temperature electrical conductivity (85% to 88% of the value at 323 K) compared to the pristine sample reaching 79% of its initial value at 323 K. This could be due to the existence of Bi at the grain boundaries of nanocomposites that can facilitate charge carrier transport. The opposite effect was seen in the case of MWCNT nanocomposites,[310] where the segregation of Ge at the boundaries led all the MWCNT containing samples to reach around 93% of their initial values at 323 K with the matrix showing 105% of its 323 K value. The low temperature electrical conductivity of the composites obtained from the Hall measurements, depicted in Figure 6.10, is in good agreement with our high temperature data.
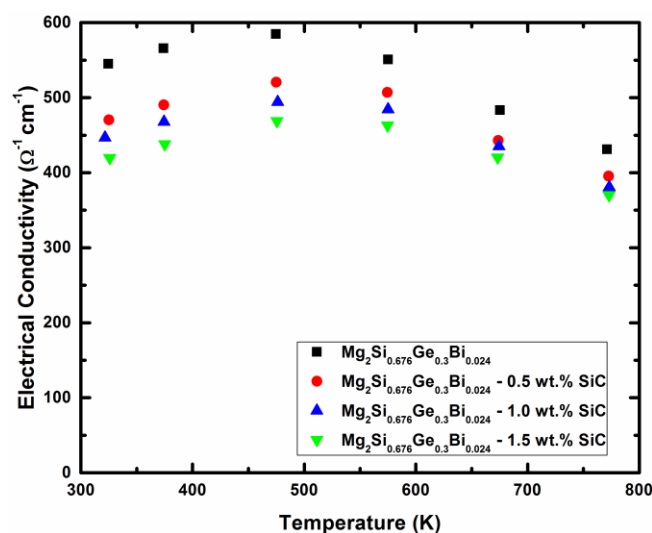
Figure 6.9   Electrical conductivity of the $Mg_2Si_{0.676}Ge_{0.3}Bi_{0.024}$/SiC nanocomposites.
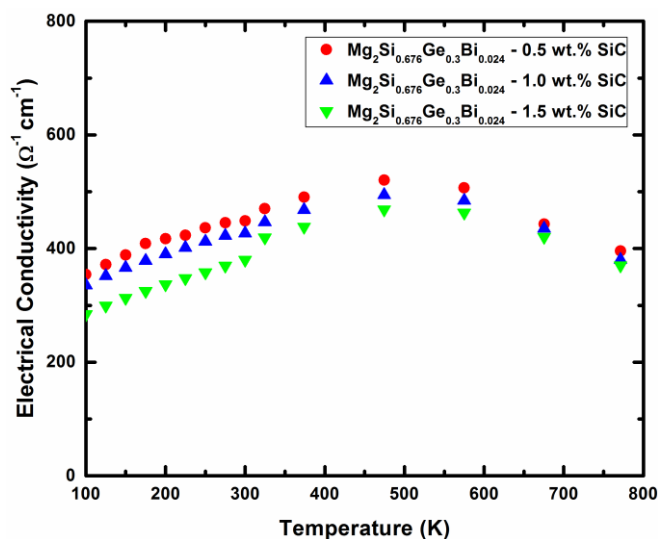
Figure 6.10   Electrical conductivity of the $Mg_2Si_{0.676}Ge_{0.3}Bi_{0.024}$/SiC nanocomposites between 2 K and 800 K (results below 300 K obtained from Hall measurements).

Due to the low concentration of the inert nanoparticles in the sample, no significant changes were observed in the carrier concentration of the samples containing SiC (Figure 6.11a), and all samples displayed a basically temperature independent carrier concentration

110

of around 6.5×10^{19} per cm^3. Therefore, the reduction in electrical conductivity must have majorly come from a lower mobility. The sample containing 1.5 wt.-% SiC exhibits the lowest mobility among all samples with 37 cm^{2}V^{-1}s^{-1} at 300 K, with the other ones having > 42 cm^{2}V^{-1}s^{-1} (Figure 6.11b). The sample containing Si nanoparticles published by Kauzlarich et al. had a mobility of around 13 cm^{2}V^{-1}s^{-1} at 300 K (Table 6.3), which is approximately three times lower than the ones achieved for our SiC nanocomposites. This could be due to its very high carrier concentration that increased the electron-phonon interaction. To better understand the effect of SiC nanoparticles on the mobility of charge carriers, the mean free path of carriers (l_e) was calculated using Equation 6.1:[311]

$$l_e = \frac{3\mu \, (2\pi m^* k_B T)^{0.5}}{4e}$$

Equation 6.1

Table 6.3　　Thermoelectric properties of Mg$_2$Si$_{0.877}$Ge$_{0.1}$Bi$_{0.023}$/0.5% SiC at 773 K in comparison to other nanocomposites.

	Mg$_2$Si$_{0.676}$Ge$_{0.3}$Bi$_{0.024}$ /0.5% SiC	Mg$_2$Si$_{0.877}$Ge$_{0.1}$Bi$_{0.023}$ /0.5% MWCNT[310]	Mg$_2$Si/2.5 mol% Si$_{1\%Bi}$[293]
σ/(Ω^{-1}cm^{-1})	396	470	658
S/(μV K^{-1})	−212	−200	−204
κ/(W m^{-1}K^{-1})	1.82	2.15	3.1
L/(10^{-8} V^{2}K^{-2})	1.60	1.62	2.2
κ_L/(W m^{-1}K^{-1})	1.33	1.56	2.0
μ/(cm^{2}V^{-1}s^{-1}) [300 K]	42	39.5	13
n/(10^{19} cm^{-3}) [300 K]	6.67	7.55	11.7
ZT	0.75	0.67	0.67

Where e, k_B, μ, m^* and T are carrier charge, Boltzmann constant, carrier mobility, effective mass and absolute temperature, respectively. The effective mass applied in equation (1) was calculated by using the experimental Seebeck value and carrier concentration.[22] The so calculated mean free path is between 3 nm and 4 nm, i.e. much lower than the average size of SiC nanoparticles (~50 nm). Due to this significant size difference, charge carriers spend more time within the nanoparticles and go through various scattering mechanisms in addition to phonon scattering.[312]
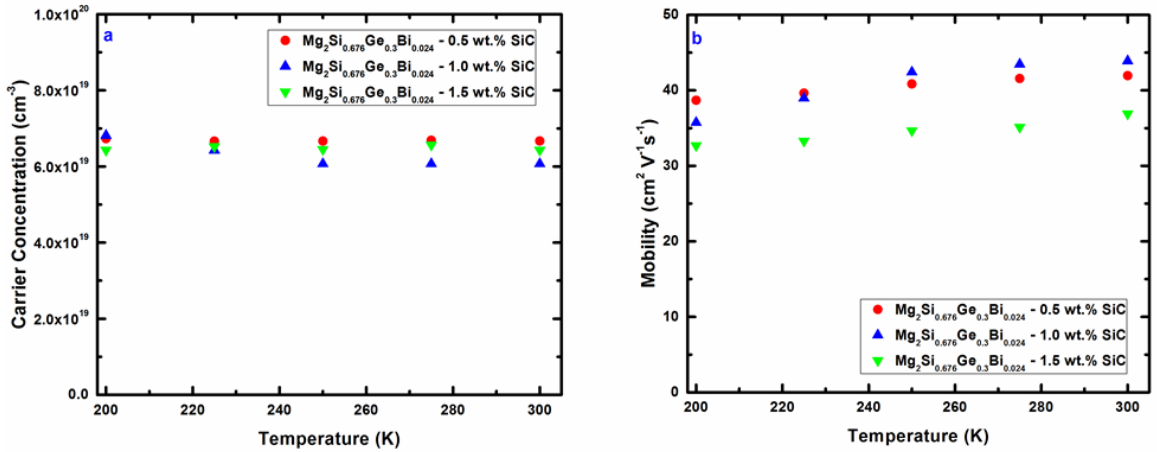
Figure 6.11   a) Room temperature carrier concentration; b) low temperature Hall mobility of the Mg$_2$Si$_{0.676}$Ge$_{0.3}$Bi$_{0.024}$/SiC nanocomposites.

The absolute values of the Seebeck coefficient increase with increasing temperature in all cases presented here (Figure 6.12). The negative Seebeck value of all composites is due to electrons as dominant charge carriers. Introducing SiC nanoparticles slightly enhances the Seebeck value especially at higher temperature (above 600 K), reaching the maximum value at 773 K for the sample containing 1 wt.-% SiC with $S = -215$ µV K^{-1} as compared to the pristine sample with $S = -202$ µV K^{-1}. The slight enhancement of the Seebeck coefficient for the composites might partially stem from the filtering effect caused by the nanoparticle-matrix interface.[302] The 0.5 wt.-% SiC composite also shows a higher $S = -212$ µV K^{-1} at 773

K than the MWCNT and Si nanoparticle composites (Table 6.3), which could be a consequence of its lower carrier concentration.
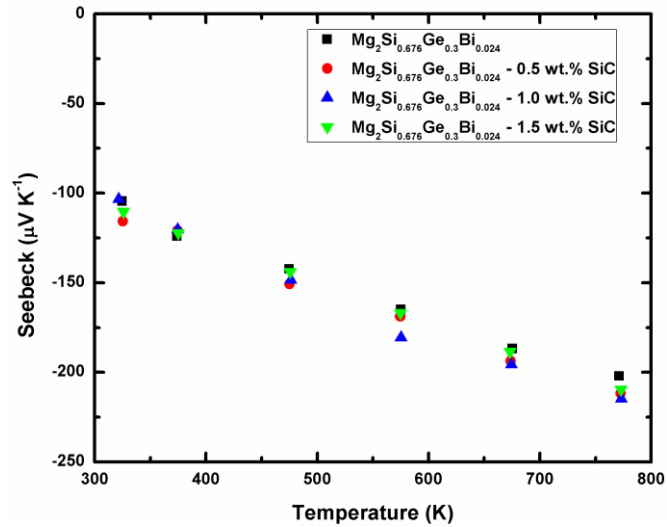
Figure 6.12   Seebeck coefficient of the $Mg_2Si_{0.676}Ge_{0.3}Bi_{0.024}$/SiC nanocomposites.

The thermal conductivity of all samples decreases with elevating temperature (Figure 6.13a), due to the dominant acoustic phonon scattering. All the samples containing SiC have lower thermal conductivity and diffusivity (Figure 6.14) than the pristine sample; which could be due to the presence of various Bi rich regions (in addition to the increased number of scattering interfaces) at the grain boundaries that can scatter different ranges of phonons; this effect was observed before in skutterudite samples containing Ag nanoparticles.[313] The sample containing 1.5 wt.-% SiC displays the lowest room temperature thermal conductivity of 2.68 W $m^{-1}K^{-1}$, which is approximately 20% lower than that of the pristine sample. The 0.5 wt.-% SiC composite reaches the minimum value of 1.82 W $m^{-1}K^{-1}$, drastically lower than the 0.5 wt.-% MWCNT composite (Table 6.3), which may be in part due to the different Si/Ge ratio.
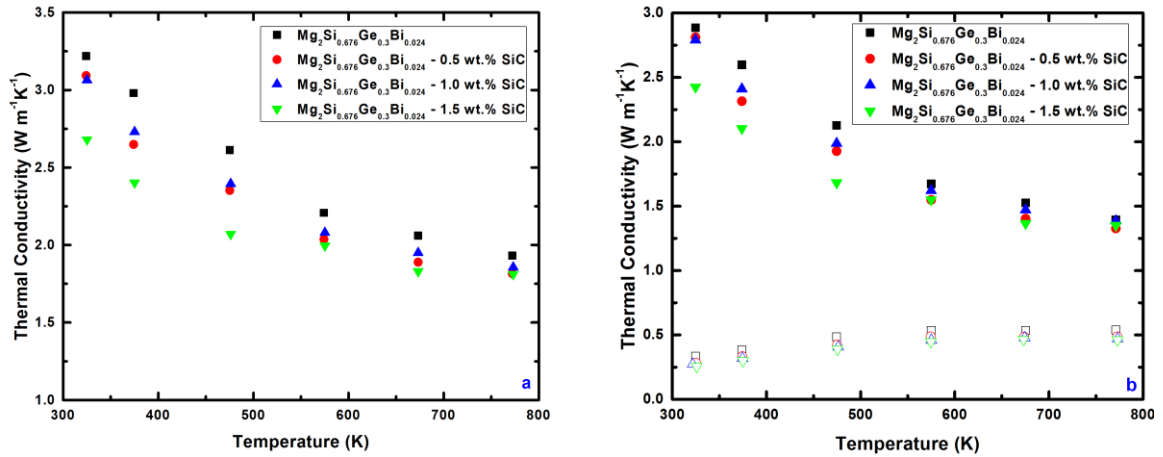
Figure 6.13   a) Thermal conductivity; b) lattice thermal conductivity (solid symbols) and electronic contribution (open symbols) of the $Mg_2Si_{0.676}Ge_{0.3}Bi_{0.024}$/SiC nanocomposites.
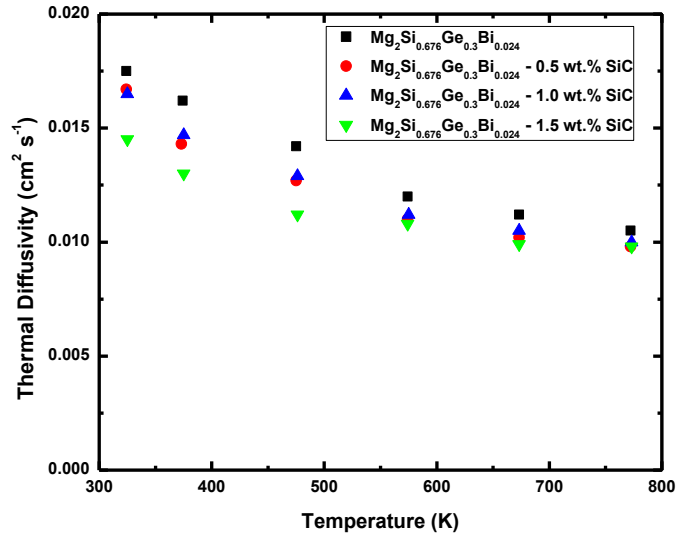
Figure 6.14   Thermal diffusivity of $Mg_2Si_{0.676}Ge_{0.3}Bi_{0.024}$/SiC nanocomposites.

The lattice thermal conductivity, κ_{ph}, of all samples (Figure 6.13b) was extracted from the thermal conductivity, κ, by subtracting the electronic part of the thermal conductivity, κ_e, which was calculated by utilizing the Wiedemann-Franz law, $\kappa_e = L\sigma T$. To obtain the

114

temperature dependence Lorenz numbers, L (Figure 6.15), in order to calculate κ_e, the single parabolic band and elastic carrier scattering approximation were applied via Equation 4.2.
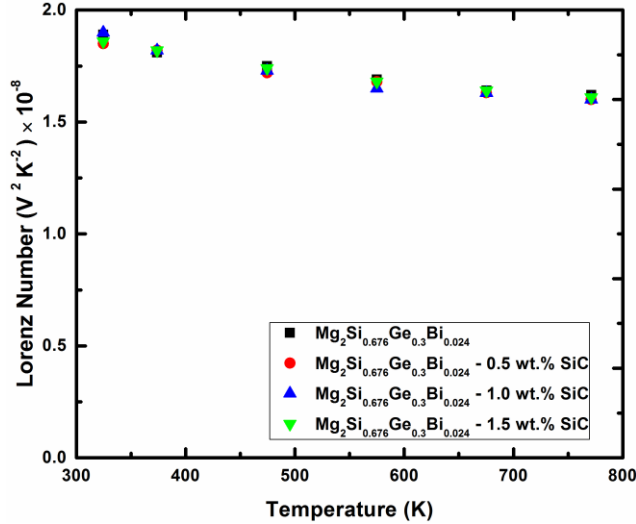
Figure 6.15   Temperature dependance of Lorenz number for Mg$_2$Si$_{0.676}$Ge$_{0.3}$Bi$_{0.024}$/SiC nanocomposites.

All the nanocomposites show lower lattice thermal conductivity than the pristine sample, with the minimum value of 1.33 W m^{-1}K^{-1} at 773 K belonging to the sample with 0.5 wt.-% SiC. This value is lower than the ones obtained for the MWCNT and Si nanoparticle composites as listed in Table 6.3. The electronic thermal conductivity of all samples increases at first with increasing temperature and then saturates at around 0.5 W m^{-1}K^{-1} after 600 K. It can be concluded that the reduction in total thermal conductivity mainly originates from lower κ_{ph}, due to the similarity of κ_e for all samples. That the high temperature values, e.g. all around 1.85 W m^{-1}K^{-1} at 773 K, are very similar, could be due to increasing charge carrier phonon interactions at high temperatures that compensate for the scattering effect coming from nanoparticles.

Figure 6.16 demonstrates the thermoelectric figure of merit ZT within the range of 300 K to 800 K. The figure of merit of all samples increases with increasing temperature,

with the highest values reached by the 0.5 wt.-% SiC sample. This culminates in $ZT = 0.75$ at 773 K, which is higher than the ZT values achieved for the $Mg_2Si_{1-x}Ge_x$ and Mg_2Si nanocomposites (Table 6.3).
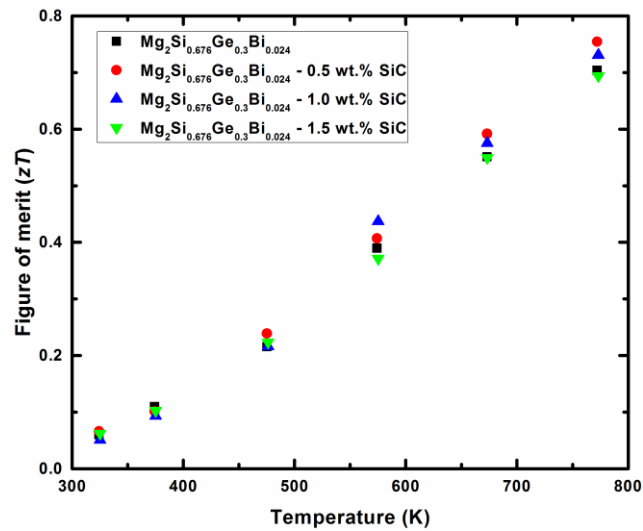
Figure 6.16   Figure of merit of the $Mg_2Si_{0.676}Ge_{0.3}Bi_{0.024}$/SiC nanocomposites.

To check for homogeneity and reproducibility, a second piece was cut from a different part of the 0.5 wt.-% SiC pellet was used for a new measurement, and the reproduced power factor (Figure 6.17) is within the estimated experimental error.

116
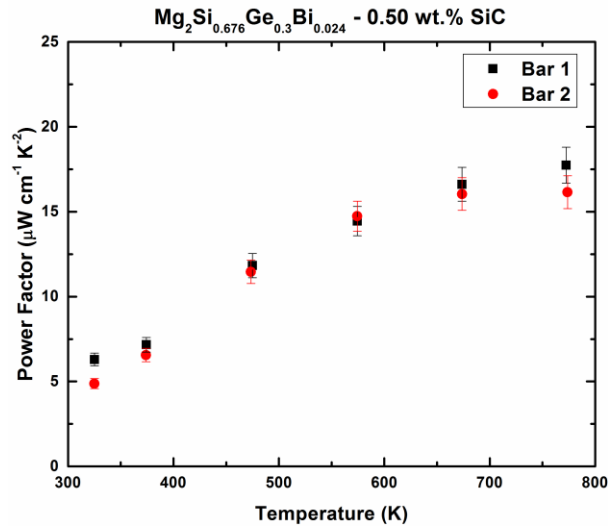
Figure 6.17   Power factor of two bars cut from the same $Mg_2Si_{0.676}Ge_{0.3}Bi_{0.024}$/0.5% SiC nanocomposite (6% estimated error).

6.4 Conclusion

Introducing SiC into $Mg_2Si_{0.676}Ge_{0.3}Bi_{0.024}$ matrix not only affected acoustic phonon scattering, which led to the lowest thermal conductivity of 1.81 W $m^{-1}K^{-1}$ at 773 K, but also hampered the mobility of charge carriers. The approximately twelve times larger size of nanoparticles with respect to electron mean free path (~4 nm), decreased the relaxation time of charge carriers, which then resulted in the lowest electrical conductivity of 370 $\Omega^{-1}cm^{-1}$ at 773 K for the sample containing the highest wt.-% of SiC. Due to the nominally equivalent Bi doping level of all composites in addition to the small SiC concentrations, all the composites exhibited similar carrier concentration of 6.5×10^{19} cm^{-3} between 200 K and 300 K. The EDX line scan of the grain boundary revealed a Bi rich character at the grain boundaries of the $Mg_2Si_{0.676}Ge_{0.3}Bi_{0.024}$/SiC composite, which could be a helpful clue for grain boundary engineering approach. All in all, the sample with 0.5 wt.-% SiC reached a maximum *ZT* of 0.75 at 773 K, which is among the highest so far achieved through nano-inclusion techniques implemented in doped Mg_2Si and $Mg_2Si_{1-x}Ge_x$ thermoelectrics. In the

future, the effect of adding different sizes of SiC nanoparticles on the microstructure and thermoelectric properties of superior $Mg_2Si_{1-x}Sn_x$ based materials can be studied.

Chapter 7

Conclusion and Future Work

Magnesium silicide based materials are undeniably the best *n*-type TE candidate among the silicides. Although the high cubic symmetry of the anti-fluorite structure facilitates the phonon transport therefore causing the relatively high thermal conductivity of these compounds, alloying and nano-inclusion seemed to be reliable approaches to reduce the thermal conductivity.

The STEM-HAADF images on the Sb- and Bi-doped Mg_2Si samples, showed only the partial substitution of the dopants in Si position, while the rest most probably forms Mg_3Sb_2 and Mg_3Bi_2, found at the grain boundaries of doped Mg_2Si particles. As a result, the experimentally determined carrier concentration was lower than originally expected. The presence of Sb and Bi at the boundaries of doped Mg_2Si may enhance the carrier mobility and thus the thermoelectric performance.

Alloying the Bi doped Mg_2Si with germanium, exhibited to be effective in reducing the thermal conductivity of Mg_2Si from about $\kappa > 7$ W m^{-1}K^{-1} down to values below 4 W m^{-1}K^{-1} at room temperature. The $Mg_2Si_{0.677}Ge_{0.3}Bi_{0.023}$ sample obtained the lowest κ and κ_L. The partial occupation of interstitial sites with Mg in addition to the presence of Ge-rich domains within the $Mg_2(Si,Ge,Bi)$ grains confirmed through HRTEM results, which could lead to a lower thermal and electrical conductivity in addition to the alloying effect/increased mass fluctuation. Bi also seems to be a more effective dopant than Sb in enhancing the thermoelectric figure of merit *ZT* in this system.

The addition of multi-wall carbon nanotubes to $Mg_2Si_{0.877}Ge_{0.1}Bi_{0.023}$ at low concentration led to a 10% improvement of the high temperature Seebeck coefficient while maintaining the high temperature electrical conductivity. This effect could be due to energy filtering that originated from the $Mg_2Si_{0.877}Ge_{0.1}Bi_{0.023}$ - MWCNT matrix interfaces. Although the existence of MWCNT reduced the lattice thermal conductivity particularly at medium temperature through enhanced phonon scattering, this reduction is compensated at higher temperature due to the thermal transport behavior of MWCNT at higher temperature.

All in all, the thermoelectric figure of merit, *ZT*, is improved more than 20% for the sample containing 0.5 wt.-% MWCNT with its *ZT* of 0.67 at 773 K. This makes the MWCNT one of the most promising candidates for the nano-inclusion in this system.

Introducing SiC into $Mg_2Si_{0.676}Ge_{0.3}Bi_{0.024}$ matrix seemed to affect both acoustic phonon and the mobility of charge carriers. The relaxation time of charge carriers reduced due to the larger size of nanoparticles with respect to electron mean free path. Bi rich character of the grain boundaries of the $Mg_2Si_{0.676}Ge_{0.3}Bi_{0.024}$/SiC composite was revealed by the EDX line scan, which could be helpful for later studies on grain boundary engineering. In summary, the sample with 0.5 wt.-% SiC gained a maximum *ZT* of 0.75 at 773 K, which is one of the highest so far achieved through nanocomposite methods implemented in doped Mg2Si and $Mg_2Si_{1-x}Ge_x$ thermoelectrics.

For future investigation, we recommend to study both the carrier and phonon mean free paths in the solid solution samples containing tin and possibly lead. This study would shed light on the size of nano-inclusion that should be used to majorly target phonons instead of charge carriers. The size effect of the nano-inclusion can also be studied experimentally, but may require the synthesis of nanoparticle to achieve higher homogeneity with a more targeted size. After identifying the optimum size of the nanoparticle, the desired amount can be explored through changing the volume percent of the nano-inclusion while fixing its size. Another crucial study in the nanocomposite samples, is to calculate the barrier height produced by the interface of nanoparticle - matrix and its effect on TE properties of the samples. Different types of nanoparticles with various ranges of band gap can be considered for this purpose.

Bibliography

[1] G. Kauffman, Chem. Educ. **4**, 36 (1999).

[2] T.M. Tritt and M.A. Subramanian, MRS Bull. **31**, 188 (2006).

[3] D.D. Pollock, in *CRC Handb. Thermoelectr.*, edited by D.M. Rowe (CRC Press, New York, 1995), pp. 7–17.

[4] A.F. Ioffe, *Semiconductor Thermoelements, and Thermoelectric Cooling* (Infosearch, ltd., 1957).

[5] G. Slack, in *CRC Handb. Thermoelectr.*, edited by D.M. Rowe (CRC Press, New York, 1995), pp. 407–440.

[6] V. Murashov and M.A. White, in *Therm. Conduct. Theory, Prop. Appl.*, edited by T.M. Tritt (Springer Science & Business Media, 2004), pp. 93–104.

[7] X. Shi, J. Yang, S. Bai, J. Yang, H. Wang, M. Chi, J.R. Salvador, W. Zhang, L. Chen, and W. Wong-Ng, Adv. Funct. Mater. **20**, 755 (2010).

[8] S. V Faleev and F. Léonard, Phys. Rev. B **77**, 214304/1 (2008).

[9] M. Zebarjadi, K. Esfarjani, A. Shakouri, J.-H. Bahk, Z. Bian, G. Zeng, J. Bowers, H. Lu, J. Zide, and A. Gossard, Appl. Phys. Lett. **94**, 202105 (2009).

[10] M.S. Dresselhaus, G. Chen, M.Y. Tang, R.G. Yang, H. Lee, D.Z. Wang, Z.F. Ren, J.-P. Fleurial, and P. Gogna, Adv. Mater. **19**, 1043 (2007).

[11] W. Kim, J. Zide, A. Gossard, D. Klenov, S. Stemmer, A. Shakouri, and A. Majumdar, Phys. Rev. Lett. **96**, 045901 (2006).

[12] R. Yang, G. Chen, and M.S. Dresselhaus, Phys. Rev. B **72**, 125418 (2005).

[13] E.L. Corral, H. Wang, J. Garay, Z. Munir, and E. V Barrera, J. Eur. Ceram. Soc. **31**, 391 (2011).

[14] S. Fiameni, S. Battiston, S. Boldrini, A. Famengo, F. Agresti, S. Barison, and M. Fabrizio, J. Solid State Chem. **193**, 142 (2012).

[15] P.A. Kinzie, *Thermocouple Temperature Measurement* (Wiley New York, 1973).

[16] Furlong; Richard R.; Wahlquist Earl J., Nucl. News **42**, 26 (1999).

[17] P.R. Mahaffy, C.R. Webster, S.K. Atreya, H. Franz, M. Wong, P.G. Conrad, D.N. Harpold, J.J. Jones, L.A. Leshin, H. Manning, T. Owen, R.O. Pepin, S.W. Squyres, and M. Trainer, Science **341**, 263 (2013).

[18] R.E. Simons and R.C. Chu, in *Semicond. Therm. Meas. Manag. Symp. 2000. Sixt. Annu. IEEE* (IEEE, 2000), pp. 1–9.

[19] T.C. Harman, B. Paris, S.E. Miller, and H.L. Goering, J. Phys. Chem. Solids **2**, 181 (1957).

[20] J.A. Wollam, H. Beale, and I.L. Spain, *Properties of Crystalline Bismuth Selenide and Its Use as a Hall Effect Magnetometer* (National Aeronautics and Space Administration, Cleveland, OH (USA). Lewis Research Center, 1972).

[21] S. Scherrer and H. Scherrer, in *Thermoelectr. Handb. Macro to Nano*, edited by D.M. Rowe (CRC Press, 2005).

[22] G.J. Snyder and E.S. Toberer, Nat. Mater. **7**, 105 (2008).

[23] H.J. Goldsmid, Materials (Basel). **7**, 2577 (2014).

[24] W. Xie, S. Wang, S. Zhu, J. He, X. Tang, Q. Zhang, and T.M. Tritt, J. Mater. Sci. **48**, 2745 (2013).

[25] F. Wu, H. Song, F. Gao, W. Shi, J. Jia, and X. Hu, J. Electron. Mater. **42**, 1140 (2013).

[26] L.-H. Ye, K. Hoang, A.J. Freeman, S.D. Mahanti, J. He, T.M. Tritt, and M.G. Kanatzidis, Phys. Rev. B **77**, 245203 (2008).

[27] B. Du, H. Li, J. Xu, X. Tang, and C. Uher, Chem. Mater. **22**, 5521 (2010).

[28] K.F. Hsu, S. Loo, F. Guo, W. Chen, J.S. Dyck, C. Uher, T. Hogan, E.K. Polychroniadis, and M.G. Kanatzidis, Science **303**, 818 (2004).

[29] J. Androulakis, K.F. Hsu, R. Pcionek, H. Kong, C. Uher, J.J. D'Angelo, A. Downey, T. Hogan, and M.G. Kanatzidis, Adv. Mater. **18**, 1170 (2006).

[30] M.G. Kanatzidis, Chem. Mater. **22**, 648 (2009).

[31] P.F.P. Poudeu, J. D'Angelo, A.D. Downey, J.L. Short, T.P. Hogan, and M.G. Kanatzidis, Angew. Chemie **118**, 3919 (2006).

[32] G.S. Nolas, D.T. Morelli, and T.M. Tritt, Annu. Rev. Mat. Sci. **29**, 89 (1999).

[33] D.J. Singh and W.E. Pickett, Phys. Rev. B **50**, 11235 (1994).

[34] T. Caillat, J.-P. Fleurial, and A. Borshchevsky, J. Cryst. Growth **166**, 722 (1996).

[35] W. Jeitschko and D. Braun, Acta Crystallogr. Sect. B Struct. Crystallogr. Cryst. Chem. **33**, 3401 (1977).

[36] J.P. Fleurial, T. Caillat, and A. Borshchevsky, in *Thermoelectr. 1997. Proc. ICT'97. XVI Int. Conf.* (IEEE, 1997), pp. 1–11.

[37] G.S. Nolas, M. Kaeser, R.T.I. Littleton, and T.M. Tritt, Appl. Phys. Lett. **77**, 1855 (2000).

[38] X. Shi, H. Kong, C.-P. Li, C. Uher, J. Yang, J.R. Salvador, H. Wang, L. Chen, and W. Zhang, Appl. Phys. Lett. **92**, 182101 (2008).

[39] X. Shi, J. Yang, J.R. Salvador, M. Chi, J.Y. Cho, H. Wang, S. Bai, J. Yang, W. Zhang, and L. Chen, J. Am. Chem. Soc. **133**, 7837 (2011).

[40] G.J. Snyder, M. Christensen, E. Nishibori, T. Caillat, and B.B. Iversen, Nat. Mater. **3**, 458 (2004).

[41] M. Tapiero, S. Tarabichi, J.G. Gies, C. Noguet, J.P. Zielinger, M. Joucla, J.L. Loison, M. Robino, and J. Herion, Sol. Energy Mater. **12**, 257 (1985).

[42] T. Caillat, J.-P. Fleurial, and A. Borshchevsky, J. Phys. Chem. Solids **58**, 1119 (1997).

[43] K. Kurosaki, A. Kosuga, H. Muta, M. Uno, and S. Yamanaka, Appl. Phys. Lett. **87**, 61919 (2005).

[44] Q. Guo, M. Chan, B.A. Kuropatwa, and H. Kleinke, Chem. Mater. **25**, 4097 (2013).

[45] Q. Guo, A. Assoud, and H. Kleinke, Adv. Energy Mater. **4**, (2014).

[46] C.M. Bhandari and D.M. Rowe, Contemp. Phys. **21**, 219 (1980).

[47] C.B. Vining and J.-P. Fleurial, in *Proc. X Int. Conf. Thermoelectr. USA* (1991), pp. 1–14.

[48] G.A. Slack and M.A. Hussain, J. Appl. Phys. **70**, 2694 (1991).

[49] V. Fano, in *CRC Handb. Thermoelectr.*, edited by D.M. Rowe (CRC Press, New York, 1995), pp. 257–266.

[50] A.D. LaLonde, Y. Pei, H. Wang, and G. Jeffrey Snyder, Mater. Today **14**, 526 (2011).

[51] A.D. LaLonde, Y. Pei, and G.J. Snyder, Energy Environ. Sci. **4**, 2090 (2011).

[52] Y. Pei, A. LaLonde, S. Iwanaga, and G.J. Snyder, Energy Environ. Sci. **4**, 2085 (2011).

[53] D. Parker and D.J. Singh, Phys. Rev. B **82**, 35204 (2010).

[54] H. Wang, Y. Pei, A.D. LaLonde, and G.J. Snyder, Adv. Mater. **23**, 1366 (2011).

[55] E.A. Skrabek and D.S. Trimmer, in *CRC Handb. Thermoelectr.*, edited by D.M. Rowe (CRC Press, Boca Raton, FL, 1995), pp. 267–275.

[56] J. Davidow and Y. Gelbstein, J. Electron. Mater. **42**, 1542 (2013).

[57] E.M. Levin, S.L. Bud'Ko, and K. Schmidt-Rohr, Adv. Funct. Mater. **22**, 2766 (2012).

[58] C.J. Goebel, *SNAP 19 Pioneer and 11 RTG Deep Space Performance* (Teledyne Energy Systems, Timonium, MD, 1975).

[59] F. Casper, T. Graf, S. Chadov, B. Balke, and C. Felser, Semicond. Sci. Technol. **27**, 63001 (2012).

[60] S. Sakurada and N. Shutoh, Appl. Phys. Lett. **86**, 82105 (2005).

[61] X. Yan, G. Joshi, W. Liu, Y. Lan, H. Wang, S. Lee, J.W. Simonson, S.J. Poon, T.M. Tritt, and G. Chen, Nano Lett. **11**, 556 (2010).

[62] D. Wood and A. Zunger, Phys. Rev. B. Condens. Matter **34**, 4105 (1986).

[63] O.O. Kurakevych, T.A. Strobel, D.Y. Kim, and G.D. Cody, Angew. Chemie **52**, 8930 (2013).

[64] O. Madelung, U. Rössler, and M. Schulz, editors , *Non-Tetrahedrally Bonded Elements and Binary Compounds I* (Springer-Verlag, Berlin/Heidelberg, 1998).

[65] R. Nakagawa, H. Katsumata, S. Hashimoto, and S. Sakuragi, Jpn. J. Appl. Phys. **54**, 085503 (2015).

[66] E. Godlewska, K. Mars, R. Mania, and S. Zimowski, Intermetallics **19**, 1983 (2011).

[67] W. Xiong, X. Qin, M. Kong, and L. Chen, Trans. Nonferrous Met. Soc. China **16**, 987 (2006).

[68] T. Ikeda, L. Haviez, Y. Li, and G.J. Snyder, Small **8**, 2350 (2012).

[69] D. Berthebaud and F. Gascoin, J. Solid State Chem. **202**, 61 (2013).

[70] M. Yoshinaga, T. Iida, M. Noda, T. Endo, and Y. Takanashi, Thin Solid Films **461**, 86 (2004).

[71] H. Itahara, T. Yamada, S.-Y. Oh, R. Asahi, H. Imagawa, and H. Yamane, Chem. Commun. **50**, 4315 (2014).

[72] Y. Maeda, K.P. Homewood, T. Sadoh, Y. Terai, K. Yamaguchi, K. Akiyama, M. Akasaka, T. Iida, K. Nishio, and Y. Takanashi, Thin Solid Films **515**, 8237 (2007).

[73] G. Fu, L. Zuo, J. Longtin, C. Nie, and R. Gambino, J. Appl. Phys. **114**, (2013).

[74] W.B. Whitten, P.L. Chung, and G.C. Danielson, J. Phys. Chem. Solids **26**, 49 (1965).

[75] M.R.J. Van Buuren, F. Voermans, and H. Van Kempen, J. Phys. Chem. 9519 (1995).

[76] P.M. Lee, Phys. Rev. **135**, (1964).

[77] U. Winkler, Helv. Phys. Acta 633 (1955).

[78] W. Klemm and H. Westlinning, Zeitschrift Fur Anorg. Und Allg. Chemie **245**, 365 (1941).

[79] G.H. Grosch and K.-J. Range, J. Alloys Compd. **235**, 250 (1996).

[80] A.K. Nikitin, E. N., Tkalenko, E. N., Zaisev, V. K., Zaslavski, A. I., & Kuznetsov, J Inorg. Mater 1656 (1970).

[81] Y.H. Duan, Y. Sun, J. Feng, and M.J. Peng, Phys. B Condens. Matter **405**, 701 (2010).

[82] P. Jund, R. Viennois, C. Colinet, G. Hug, M. Fèvre, and J.-C. Tédenac, J. Phys. Condens. Matter **25**, 035403 (2013).

[83] A. Kato, T. Yagi, and N. Fukusako, J. Phys. Condens. Matter **21**, 205801 (2009).

[84] R. Viennois, P. Jund, C. Colinet, and J.C. Tédenac, J. Solid State Chem. **193**, 133 (2012).

[85] M. Akasaka, T. Iida, T. Nemoto, J. Soga, J. Sato, K. Makino, M. Fukano, and Y. Takanashi, J. Cryst. Growth **304**, 196 (2007).

[86] H.R. Shanks, J. Cryst. Growth **23**, 190 (1974).

[87] P. Zwolenski, J. Tobola, and S. Kaprzyk, J. Alloys Compd. **627**, 85 (2015).

[88] B.D. Lichter, J. Electrochem. Soc. **109**, 819 (1962).

[89] H.Y. Chen and N. Savvides, J. Cryst. Growth **312**, 2328 (2010).

[90] Q.S. Meng, W.H. Fan, R.X. Chen, and Z. a. Munir, J. Alloys Compd. **509**, 7922 (2011).

[91] Q. Zhang, W. Liu, C. Liu, K. Yin, and X.F. Tang, J. Electron. Mater. (2014).

[92] Y. Oto, T. Iida, T. Sakamoto, R. Miyahara, a. Natsui, K. Nishio, Y. Kogo, N. Hirayama, and Y. Takanashi, Phys. Status Solidi Curr. Top. Solid State Phys. **10**, 1857 (2013).

[93] T. Sakamoto, T. Iida, A. Matsumoto, Y. Honda, T. Nemoto, J. Sato, T. Nakajima, H. Taguchi, and Y. Takanashi, J. Electron. Mater. **39**, 1708 (2010).

[94] H. Gao, T. Zhu, X. Zhao, and Y. Deng, Dalt. Trans. **43**, 14072 (2014).

[95] Q. Zhang, J. He, X.B. Zhao, S.N. Zhang, T.J. Zhu, H. Yin, and T.M. Tritt, J. Phys. D. Appl. Phys. **41**, 185103 (2008).

[96] X. Zhou, G. Wang, H. Chi, X. Su, J.R. Salvador, W. Liu, X. Tang, and C. Uher, J. Electron. Mater. **41**, 1589 (2012).

[97] T. Noda, H. Kon, Y. Furukawa, N. Otsuka, O.A. Nishida, and K. Masumoto, Mater. Trans. - JIM **33**, 845 (1992).

[98] Y. Isoda, M. Held, S. Tada, and Y. Shinohara, J. Electron. Mater. **43**, 2053 (2014).

[99] N. V. Morozova, S. V. Ovsyannikov, I. V. Korobeinikov, A.E. Karkin, K.I. Takarabe, Y. Mori, S. Nakamura, and V. V. Shchennikov, J. Appl. Phys. **115**, 213705 (2014).

[100] T. Sakamoto, T. Iida, S. Kurosaki, K. Yano, H. Taguchi, K. Nishio, and Y. Takanashi, J. Electron. Mater. **40**, 629 (2011).

[101] J.I. Tani and H. Kido, J. Alloys Compd. **466**, 335 (2008).

[102] X. Hu, M.R. Barnett, and A. Yamamoto, J. Alloys Compd. (2015).

[103] N.T. Satyala, J.S. Krasinski, and D. Vashaee, 2012 IEEE Green Technol. Conf. 1 (2012).

[104] J.I. Tani and H. Kido, Jpn. J. Appl. Phys. **46**, 3309 (2007).

[105] M. Ioannou, G. Polymeris, E. Hatzikraniotis, A.U. Khan, K.M. Paraskevopoulos, and T. Kyratsi, J. Electron. Mater. **42**, 1827 (2013).

[106] Y. Hayatsu, T. Iida, T. Sakamoto, S. Kurosaki, K. Nishio, Y. Kogo, and Y. Takanashi, J. Solid State Chem. **193**, 161 (2012).

[107] W. Liu, Q. Zhang, X. Tang, H. Li, and J. Sharp, J. Electr. Mater. **40**, 1062 (2011).

[108] Z. Du, T. Zhu, Y. Chen, J. He, H. Gao, G. Jiang, T.M. Tritt, and X. Zhao, J. Mater. Chem. **22**, 6838 (2012).

[109] T. Dasgupta, C. Stiewe, R. Hassdorf, A.J. Zhou, L. Boettcher, and E. Mueller, Phys. Rev. B **83**, 235207 (2011).

[110] W. Liu, X. Tang, and J. Sharp, J. Phys. D **43**, 085406/1 (2010).

[111] M. Søndergaard, M. Christensen, K.A. Borup, H. Yin, and B.B. Iversen, J. Electron. Mater. **42**, 1417 (2012).

[112] A.U. Khan, N. Vlachos, and T. Kyratsi, Scr. Mater. **69**, 606 (2013).

[113] W. Liu, X. Tang, H. Li, J. Sharp, X. Zhou, and C. Uher, **2**, (2011).

[114] S.-W. You, D.-K. Shin, and I.-H. Kim, J. Korean Phys. Soc. **64**, 1346 (2014).

[115] J. Tobola, S. Kaprzyk, and H. Scherrer, J. Electron. Mater. **39**, 2064 (2010).

[116] N. Farahi, M. VanZant, J. Zhao, J.S. Tse, S. Prabhudev, G.A. Botton, J.R. Salvador, F. Borondics, Z. Liu, and H. Kleinke, Dalton Trans. **43**, 14983 (2014).

[117] J.-Y. Jung, K.-H. Park, and I.-H. Kim, IOP Conf. Ser. Mater. Sci. Eng. **18**, 142006 (2011).

[118] K. Arai, A. Sasaki, Y. Kimori, M. Iida, T. Nakamura, Y. Yamaguchi, K. Fujimoto, R. Tamura, T. Iida, and K. Nishio, Mater. Sci. Eng. B **195**, 45 (2015).

[119] J.I. Tani and H. Kido, Intermetallics **15**, 1202 (2007).

[120] N. Hirayama, T. Iida, H. Funashima, S. Morioka, M. Sakamoto, K. Nishio, Y. Kogo, Y. Takanashi, and N. Hamada, J. Electron. Mater. **44**, 1656 (2014).

[121] H. Gao, T. Zhu, X. Liu, L. Chen, and X. Zhao, J. Mater. Chem. **21**, 5933 (2011).

[122] H. Le-Quoc, S. Béchu, S. Populoh, a. Weidenkaff, and a. Lacoste, J. Alloys Compd. **546**, 138 (2013).

[123] H. Gao, T. Zhu, X. Zhao, and Y. Deng, J. Solid State Chem. **220**, 157 (2014).

[124] X. Zhang, H. Liu, S. Li, F. Zhang, Q. Lu, and J. Zhang, Mater. Lett. **123**, 31 (2014).

[125] M. Søndergaard, M. Christensen, K.A. Borup, H. Yin, and B.B. Iversen, Acta Mater. **60**, 5745 (2012).

[126] G. Bernard-Granger, C. Navone, J. Leforestier, M. Boidot, K. Romanjek, J. Carrete, and J. Simon, Acta Mater. **96**, 437 (2015).

[127] J. Tani and H. Kido, Phys. B Condens. Matter **364**, 218 (2005).

[128] W. Liu, Q. Zhang, K. Yin, H. Chi, X. Zhou, X. Tang, and C. Uher, J. Solid State Chem. **203**, 333 (2013).

[129] X. Zhang, H. Liu, Q. Lu, J. Zhang, and F. Zhang, Appl. Phys. Lett. **103**, 063901 (2013).

[130] M. Ioannou, G.S. Polymeris, E. Hatzikraniotis, K.M. Paraskevopoulos, and T. Kyratsi, J. Phys. Chem. Solids **75**, 984 (2014).

[131] P. Gao, X. Lu, I. Berkun, R.D. Schmidt, E.D. Case, and T.P. Hogan, Appl. Phys. Lett. **105**, 202104 (2014).

[132] A. Kolezynski, P. Nieroda, P. Jelen, M. Sitarz, and K.T. Wojciechowski, Vib. Spectrosc. **76**, 31 (2014).

[133] K. Mars, H. Ihou-Mouko, G. Pont, J. Tobola, and H. Scherrer, J. Electron. Mater. **38**, 1360 (2009).

[134] X. Zhang, H. Liu, Q. Lu, J. Zhang, and F. Zhang, Appl. Phys. Lett. **103**, 063901 (2013).

[135] A.U. Khan, N.V. Vlachos, E. Hatzikraniotis, G.S. Polymeris, C.B. Lioutas, E.C. Stefanaki, K.M. Paraskevopoulos, I. Giapintzakis, and T. Kyratsi, Acta Mater. **77**, 43 (2014).

[136] Z. Du, T. Zhu, and X. Zhao, Mater. Lett. **66**, 76 (2012).

[137] S. Fiameni, S. Battiston, S. Boldrini, A. Famengo, F. Agresti, S. Barison, and M. Fabrizio, J. Solid State Chem. **193**, 142 (2012).

[138] S.-W. You, I.-H. Kim, S.-M. Choi, and W.-S. Seo, J. Korean Phys. Soc. **63**, 2153 (2013).

[139] S.-M. Choi, K.-H. Kim, I.-H. Kim, S.-U. Kim, and W.-S. Seo, Curr. Appl. Phys. **11**, S388 (2011).

[140] N. Farahi, S. Prabhudev, G.A. Botton, J. Zhao, J.S. Tse, Z. Liu, J.R. Salvador, and H. Kleinke, J. Alloys Compd. **644**, 249 (2015).

[141] W. Liu, H. Chi, H. Sun, Q. Zhang, K. Yin, X. Tang, Q. Zhang, and C. Uher, Phys. Chem. Chem. Phys. **16**, 6893 (2014).

[142] S. Muthiah, B. Sivaiah, B. Gahtori, K. Tyagi, A.K. Srivastava, B.D. Pathak, A. Dhar, and R.C. Budhani, J. Electron. Mater. **43**, 2035 (2014).

[143] J.-Y. Jung and I.-H. Kim, Electron. Mater. Lett. **6**, 187 (2010).

[144] J.-Y. Jung and I.-H. Kim, J. Electron. Mater. **40**, 1144 (2011).

[145] S. Tada, Y. Isoda, H. Udono, H. Fujiu, S. Kumagai, and Y. Shinohara, J. Electron. Mater. **43**, 1580 (2013).

[146] Q. Zhang, L. Cheng, W. Liu, Y. Zheng, X. Su, H. Chi, H. Liu, Y. Yan, X. Tang, and C. Uher, Phys. Chem. Chem. Phys. **16**, 23576 (2014).

[147] A. Kolezynski, P. Nieroda, and K.T. Wojciechowski, Comput. Mater. Sci. **100**, 84 (2015).

[148] Y. Isoda, S. Tada, T. Nagai, H. Fujiu, and Y. Shinohara, Mater. Trans. **51**, 868 (2010).

[149] Y. Isoda, S. Tada, T. Nagai, H. Fujiu, and Y. Shinohara, J. Electron. Mater. **39**, 1531 (2010).

[150] S. Kim, B. Wiendlocha, H. Jin, J. Tobola, and J.P. Heremans, J. Appl. Phys. **116**, 153706 (2014).

[151] X. Han and G. Shao, J. Mater. Chem. C **3**, 530 (2015).

[152] A. Prytuliak, E. Godlewska, K. Mars, and D. Berthebaud, J. Electron. Mater. **43**, 3746 (2014).

[153] H. Ihou-Mouko, C. Mercier, J. Tobola, G. Pont, and H. Scherrer, J. Alloys Compd. **509**, 6503 (2011).

[154] W. Liu, K. Yin, X. Su, H. Li, Y. Yan, X. Tang, and C. Uher, Intermetallics **32**, 352 (2013).

[155] Q. Zhang, X.B. Zhao, H. Yin, and T.J. Zhu, J. Alloys Compd. **464**, 9 (2008).

[156] L.M. Zhang, Y.G. Leng, H.Y. Jiang, L.D. Chen, and T. Hirai, in *Proc. ICT2001. 20 Int. Conf. Thermoelectr. (Cat. No.01TH8589)* (IEEE, 2001), pp. 233–235.

[157] S. Tada, Y. Isoda, H. Udono, H. Fujiu, S. Kumagai, and Y. Shinohara, Phys. Status Solidi Curr. Top. Solid State Phys. **10**, 1704 (2013).

[158] S.-W. You, D.-K. Shin, and I.-H. Kim, J. Korean Phys. Soc. **65**, 57 (2014).

[159] G. Bernard-Granger, R. Vracar, C. Navone, J. Leforestier, M. Boidot, J. Carrete, B. Deniau, and J. Simon, Scr. Mater. (2015).

[160] R.B. Song, T. Aizawa, and J.Q. Sun, Mater. Sci. Eng. B **136**, 111 (2007).

[161] W. Li, L. Lindsay, D. a. Broido, D. a. Stewart, and N. Mingo, Phys. Rev. B **86**, 174307 (2012).

[162] J.J. Pulikkotil, D.J. Singh, S. Auluck, M. Saravanan, D.K. Misra, A. Dhar, and R.C. Budhani, Phys. Rev. B **86**, 1 (2012).

[163] A.Y. Samunin, V.K. Zaitsev, P.P. Konstantinov, M.I. Fedorov, G.N. Isachenko, A.T. Burkov, S. V. Novikov, and E.A. Gurieva, J. Electron. Mater. **42**, 1676 (2012).

[164] D. a. Pshenai-Severin, M.I. Fedorov, and a. Y. Samunin, J. Electron. Mater. **42**, 1707 (2013).

[165] Q. Zhang, J. He, T.J. Zhu, S.N. Zhang, X.B. Zhao, and T.M. Tritt, Appl. Phys. Lett. **93**, 102109 (2008).

[166] M. Søndergaard, M. Christensen, K.A. Borup, H. Yin, and B.B. Iversen, J. Mater. Sci. **48**, 2002 (2013).

[167] K. Yin, Q. Zhang, Y. Zheng, X. Su, X. Tang, and C. Uher, J. Mater. Chem. C **7**, (2015).

[168] M. Riffel and J. Schilz, Fifteenth Int. Conf. Thermoelectr. 133 (1996).

[169] Q. Zhang, Y. Zheng, X. Su, K. Yin, X. Tang, and C. Uher, Scr. Mater. **96**, 1 (2015).

[170] M.B.A. Bashir, S. Mohd Said, M.F.M. Sabri, D.A. Shnawah, and M.H. Elsheikh, Renew. Sustain. Energy Rev. **37**, 569 (2014).

[171] P. Gao, I. Berkun, R.D. Schmidt, M.F. Luzenski, X. Lu, P. Bordon Sarac, E.D. Case, and T.P. Hogan, J. Electron. Mater. **43**, 1790 (2014).

[172] P. Bellanger, S. Gorsse, G. Bernard-Granger, C. Navone, A. Redjaimia, and S. Vivès, Acta Mater. **95**, 102 (2015).

[173] X. Liu, T. Zhu, H. Wang, L. Hu, H. Xie, G. Jiang, G.J. Snyder, and X. Zhao, Adv. Energy Mater. **3**, 1238 (2013).

[174] V.K. Zaitsev, M.I. Fedorov, a. T. Burkov, E. a. Gurieva, I.S. Eremin, P.P. Konstantinov, S. V. Ordin, S. Sano, and M.V. Vedernikov, 21st Int. Conf. Thermoelectr. 151 (2002).

[175] W. Liu, X. Tang, H. Li, K. Yin, J. Sharp, X. Zhou, and C. Uher, J. Mater. Chem. **22**, 13653 (2012).

[176] S. Vivès, P. Bellanger, S. Gorsse, C. Wei, Q. Zhang, and J.C. Zhao, Chem. Mater. **26**, 4334 (2014).

[177] J.-H. Bahk, Z. Bian, and A. Shakouri, Phys. Rev. B **89**, 075204 (2014).

[178] Q. Zhang, T.J. Zhu, a. J. Zhou, H. Yin, and X.B. Zhao, Phys. Scr. **2007**, 123 (2007).

[179] T. Dasgupta, C. Stiewe, J. de Boor, and E. Müller, Phys. Status Solidi **211**, 1250 (2014).

[180] V.K. Zaitsev, M.I. Fedorov, E.A. Gurieva, I.S. Eremin, P.P. Konstantinov, A.Y. Samunin, and M. V Vedernikov, Phys. Rev. B **74**, 045207/1 (2006).

[181] W. Luo, M. Yang, F. Chen, Q. Shen, H. Jiang, and L. Zhang, Mater. Sci. Eng. B **157**, 96 (2009).

[182] S. Muthiah, J. Pulikkotil, a. K. Srivastava, A. Kumar, B.D. Pathak, A. Dhar, and R.C. Budhani, Appl. Phys. Lett. **103**, 053901 (2013).

[183] E.N. Nikitin, V.G. Bazanov, and V.I. Tarasov, Sov. Phys. Solid State **3**, 2648 (1961).

[184] L. Chen, G. Jiang, Y. Chen, Z. Du, X. Zhao, T. Zhu, J. He, and T.M. Tritt, J. Mater. Res. **26**, 3038 (2011).

[185] J.-W. Liu, M. Song, M. Takeguchi, N. Tsujii, and Y. Isoda, J. Electron. Mater. **44**, 407 (2014).

[186] B. Abeles, Phys. Rev. **131**, 1906 (1963).

[187] X.J. Tan, W. Liu, H.J. Liu, J. Shi, X.F. Tang, and C. Uher, Phys. Rev. B **85**, 205212 (2012).

[188] W. Liu, X. Tan, K. Yin, H. Liu, X. Tang, J. Shi, Q. Zhang, and C. Uher, Phys. Rev. Lett. **108**, 166601 (2012).

[189] R.D. Shannon, Acta Crystallogr. Sect. A **32**, 751 (1976).

[190] R.T. Sanderson, J. Am. Chem. Soc. **105**, 2259 (1983).

[191] J. Tani and H. Kido, Intermetallics **16**, 418 (2008).

[192] W. Liu, X. Tang, and J. Sharp, J. Phys. D. Appl. Phys. **43**, 085406 (2010).

[193] W. Liu, Q. Zhang, K. Yin, H. Chi, X. Zhou, X. Tang, and C. Uher, J. Solid State Chem. **203**, 333 (2013).

[194] W. Liu, X. Tang, H. Li, K. Yin, J. Sharp, X. Zhou, and C. Uher, J. Mater. Chem. **22**, 13653 (2012).

[195] A.U. Khan, N. Vlachos, and T. Kyratsi, Scr. Mater. **69**, 606 (2013).

[196] J.-W. Liu, M. Song, M. Takeguchi, N. Tsujii, and Y. Isoda, J. Electron. Mater. (2014).

[197] A. J. Slifka, B. J. Filla and J. M. Phelps, J. Res. Natl. Inst. Stand. Technol. **103**, 357 (1998).

[198] J. de Boor, T. Dasgupta, H. Kolb, C. Compere, K. Kelm, and E. Mueller, Acta Mater. **77**, 68 (2014).

[199] Z. Du, T. Zhu, Y. Chen, J. He, H. Gao, G. Jiang, T.M. Tritt, and X. Zhao, J. Mater. Chem. **22**, 6838 (2012).

[200] G. Jiang, J. He, T. Zhu, C. Fu, X. Liu, L. Hu, and X. Zhao, Adv. Funct. Mater. **24**, 3776 (2014).

[201] P. Gao, I. Berkun, R.D. Schmidt, M.F. Luzenski, X. Lu, P. Bordon Sarac, E.D. Case, and T.P. Hogan, J. Electron. Mater. **43**, 1790 (2013).

[202] L. Zhang, P. Xiao, L. Shi, G. Henkelman, J.B. Goodenough, and J. Zhou, J. Appl. Phys. **117**, 155103 (2015).

[203] H. Ning, G.D. Mastrorillo, S. Grasso, B. Du, T. Mori, C. Hu, Y. Xu, K. Simpson, G. Maizza, and M. Reece, J. Mater. Chem. A **3**, 17426 (2015).

[204] Z. Pan, Y. Du, B. Huang, H. Xu, Y. Liu, H. Chen, W. Xiong, and R. Schmid-Fetzer, J. Mater. Sci. **41**, 2525 (2006).

[205] P. Manfrinetti, M.L. Fornasini, and A. Palenzona, Intermetallics **8**, 223 (2000).

[206] Z. Yang, D. Shi, B. Wen, R. Melnik, S. Yao, and T. Li, J. Solid State Chem. **183**, 136 (2010).

[207] D.B. Migas, V.O. Bogorodz, A.B. Filonov, V.L. Shaposhnikov, V.E. Borisenko, and N.G. Galkin, Jpn. J. Appl. Phys. **54**, 07JA03 (2015).

[208] C. Wen, T. Nonomura, A. Kato, Y. Kenichi, H. Udono, K. Isobe, M. Otake, Y. Kubota, T. Nakamura, Y. Hayakawa, and H. Tatsuoka, Phys. Procedia **11**, 106 (2011).

[209] Y. Imai, A. Watanabe, and M. Mukaida, J. Alloys Compd. **358**, 257 (2003).

[210] C. Wen, T. Nonomura, K. Isobe, Y. Kubota, T. Nakamura, Y. Hayakawa, A. Kato, and H. Tatsuoka, IOP Conf. Ser. Mater. Sci. Eng. **18**, 142014 (2011).

[211] D.B. Migas, V.L. Shaposhnikov, A.B. Filonov, N.N. Dorozhkin, and V.E. Borisenko, J. Phys. Condens. Matter **19**, 346207 (2007).

[212] X. Tao, J. Yang, L. Xi, and Y. Ouyang, J. Solid State Chem. **194**, 179 (2012).

[213] Y. Imamura, H. Muta, K. Kurosaki, and S. Yamanaka, in *2006 25th Int. Conf. Thermoelectr.* (IEEE, 2006), pp. 535–538.

[214] T. Inaba, A. Kato, K. Miura, M. Akasaka, T. Iida, Y. Momose, and H. Tatsuoka, Thin Solid Films **515**, 8226 (2007).

[215] A. Palenzona and M. Pani, J. Alloys Compd. **373**, 214 (2004).

[216] Y. Imai and A. Watanabe, Intermetallics **10**, 333 (2002).

[217] S. Brutti, D. Nguyen-Manh, and D.G. Pettifor, J. Alloys Compd. **457**, 29 (2008).

[218] J. Hu, A. Kato, T. Sadoh, Y. Maeda, K.N. Galkin, T. V. Turchin, and H. Tatsuka, Int. J. Mod. Phys. B **24**, 3693 (2010).

[219] J. Evers and A. Weiss, Solid State Commun. **17**, 41 (1975).

[220] M. Imai, T. Naka, T. Furubayashi, H. Abe, T. Nakama, and K. Yagasaki, Appl. Phys. Lett. **86**, 032102 (2005).

[221] G.E. Pringle, Acta Crystallogr. Sect. B Struct. Crystallogr. Cryst. Chem. **28**, 2326 (1972).

[222] K. Hashimoto, K. Kurosaki, Y. Imamura, H. Muta, and S. Yamanaka, J. Appl. Phys. **102**, 063703 (2007).

[223] Y.-K. Kuo, B. Ramachandran, and C.-S. Lue, Front. Chem. **2**, 106 (2014).

[224] C.S. Lue, C.N. Kuo, J.Y. Huang, H.L. Hsieh, H.Y. Liao, B. Ramachandran, and Y.K. Kuo, J. Phys. D. Appl. Phys. **46**, 315303 (2013).

[225] C.S. Lue, M.D. Chou, N. Kaurav, Y.T. Chung, and Y.K. Kuo, Appl. Phys. Lett. **94**, 192105 (2009).

[226] C.S. Lue, S.F. Wong, J.Y. Huang, H.L. Hsieh, H.Y. Liao, B. Ramachandran, and Y.K. Kuo, J. Appl. Phys. **113**, 013710 (2013).

[227] M. Pani and A. Palenzona, J. Alloys Compd. **454**, L1 (2008).

[228] S. Kishino, T. Imai, T. Iida, Y. Nakaishi, M. Shinada, Y. Takanashi, and N. Hamada, J. Alloys Compd. **428**, 22 (2007).

[229] Y. Imai and A. Watanabe, Thin Solid Films **515**, 8219 (2007).

[230] K. Hashimoto, K. Kurosaki, H. Muta, and S. Yamanaka, MRS Proc. **1044**, 1044 (2007).

[231] U. Aydemir, A. Ormeci, H. Borrmann, B. Böhme, F. Zürcher, B. Uslu, T. Goebel, W. Schnelle, P. Simon, W. Carrillo-Cabrera, F. Haarmann, M. Baitinger, R. Nesper, H.G. Von Schnering, and Y. Grin, Zeitschrift Fur Anorg. Und Allg. Chemie **634**, 1651 (2008).

[232] L.-D. Zhao, J. He, D. Berardan, Y. Lin, J.-F. Li, C.-W. Nan, and N. Dragoe, Energy Environ. Sci. **7**, 2900 (2014).

[233] X. Lu, D.T. Morelli, Y. Xia, F. Zhou, V. Ozolins, H. Chi, X. Zhou, and C. Uher, Adv. Energy Mater. **3**, 342 (2013).

[234] U. Schubert and N. Hüsing, *Synthesis of Inorganic Materials* (John Wiley & Sons, 2012).

[235] M. Ladd and R. Palmer, *Structure Determination by X-Ray Crystallography: Analysis by X-Rays and Neutrons* (Springer Science & Business Media, 2013).

[236] G. Will, *Powder Diffraction: The Rietveld Method and the Two Stage Method to Determine and Refine Crystal Structures from Powder Diffraction Data* (Springer Science & Business Media, 2006).

[237] J.I. Langford and A.J.C. Wilson, J. Appl. Crystallogr. **11**, 102 (1978).

[238] T.M. Tritt, *Thermal Conductivity: Theory, Properties, and Applications* (Springer Science & Business Media, 2006).

[239] L. Vozár and W. Hohenauer, High Temp. Press. **35/36**, 253 (2003).

[240] F.I. Chu, R.E. Taylor, and A.B. Donaldson, J. Appl. Phys. **51**, 336 (1980).

[241] W.J. Parker, R.J. Jenkins, C.P. Butler, and G.L. Abbott, J. Appl. Phys. **32**, 1679 (1961).

[242] M.E. Brown, *Introduction to Thermal Analysis: Techniques and Applications* (Springer Science & Business Media, 2001).

[243] W. Zhou and Z.L. Wang, editors , *Scanning Microscopy for Nanotechnology* (Springer New York, New York, NY, 2007).

[244] K.A. Borup, J. de Boor, H. Wang, F. Drymiotis, F. Gascoin, X. Shi, L. Chen, M.I. Fedorov, E. Müller, B.B. Iversen, and G.J. Snyder, Energy Environ. Sci. **8**, 423 (2015).

[245] G.J. Snyder and E.S. Toberer, Nat. Mater. **7**, 105 (2008).

[246] H. Wang, S. Bai, L. Chen, A. Cuenat, G. Joshi, H. Kleinke, J. König, H.W. Lee, J. Martin, M.-W. Oh, W.D. Porter, Z. Ren, J. Salvador, J. Sharp, P. Taylor, A.J. Thompson, and Y.C. Tseng, J. Electron. Mater. **44**, 4482 (2015).

[247] H. Wang, W.D. Porter, H. Böttner, J. König, L. Chen, S. Bai, T.M. Tritt, A. Mayolet, J. Senawiratne, C. Smith, F. Harris, P. Gilbert, J. Sharp, J. Lo, H. Kleinke, and L. Kiss, J. Electron. Mater. **42**, 1073 (2013).

[248] H. Wang, W.D. Porter, H. Böttner, J. König, L. Chen, S. Bai, T.M. Tritt, A. Mayolett, J. Senawiratne, C. Smith, F. Harris, P. Gilbert, J.W. Sharp, J. Lo, H. Kleinke, and L.I. Kiss, J. Electr. Mater. **42**, 654 (2013).

[249] E.J. Kirkland, *Image Simulation in Transmission Electron Microscopy* (Cornell University, ,

Ithaca, NY, USA, 2006).

[250] J.P. Perdew, K. Burke, and M. Ernzerhof, Phys. Rev. Lett. **77**, 3865 (1996).

[251] G. Kresse and J. Hafner, Phys. Rev. B **47**, 558 (1993).

[252] G. Kresse and J. Furthmüller, Comput. Mater. Sci. **6**, 15 (1996).

[253] G. Kresse and J. Hafner, Phys. Rev. B **49**, 14251 (1994).

[254] G. Kresse, Phys. Rev. B **54**, 11169 (1996).

[255] L. Hedin, Phys. Rev. **139**, A796 (1965).

[256] P. García-González and R. Godby, Phys. Rev. B **63**, 075112 (2001).

[257] G. Kresse, Phys. Rev. B **59**, 1758 (1999).

[258] P.E. Blöchl, Phys. Rev. B **50**, 17953 (1994).

[259] M.-X. Chen, First-Principles Modeling of Thermoelectric Materials, 2012.

[260] G.K.H. Madsen and D.J. Singh, Comput. Phys. Commun. **175**, 67 (2006).

[261] A.B. Kuzmenko, Rev. Sci. Instrum. **76**, 083108 (2005).

[262] A. Stella, A.D. Brothers, R.H. Hopkins, and D.W. Lynch, Phys. Status Solidi **23**, 697 (1967).

[263] P. Boulet and M.C. Record, J. Chem. Phys. **135**, 0 (2011).

[264] F. Tran and P. Blaha, Phys. Rev. Lett. **102**, 226401 (2009).

[265] B. Arnaud and M. Alouani, Phys. Rev. B **64**, 033202 (2001).

[266] A.M. Fox, *Optical Properties of Solids* (Oxford University Press, 2001).

[267] S.K. Bux, M.T. Yeung, E.S. Toberer, G.J. Snyder, R.B. Kaner, and J.-P. Fleurial, J. Mater. Chem. **21**, 12259 (2011).

[268] G.S. Nolas, D. Wang, and M. Beekman, Phys. Rev. B **76**, 235204 (2007).

[269] D. McWilliams and D.W. Lynch, Phys. Rev. **130**, 2248 (1963).

[270] P. YU and M. Cardona, *Fundamentals of Semiconductors: Physics and Materials Properties* (Springer Science & Business Media, 2013).

[271] S.K. Bux, M.T. Yeung, E.S. Toberer, G.J. Snyder, R.B. Kaner, and J.-P. Fleurial, J. Mater. Chem. **21**, 12259 (2011).

[272] S.-M. Choi, K.-H. Kim, I.-H. Kim, S.-U. Kim, and W.-S. Seo, Curr. Appl. Phys. **11**, S388 (2011).

[273] M. Cutler, J. Leavy, and R. Fitzpatrick, Phys. Rev. **133**, A1143 (1964).

274 E. Ratai, M.P. Augustine, and S.M. Kauzlarich, J. Phys. Chem. B **107**, 12573 (2003).

275 A.B. Kuzmenko, Rev. Sci. Instrum. **76**, 083108/1 (2005).

276 M. Fox, *Optical Properties of Solids*, 2nd editio (Oxford University Press, New York City, NY, USA, 2010).

277 J.P. Perdew, K. Burke, and M. Ernzerhof, Phys. Rev. Lett. **77**, 3865 (1996).

278 S.-W. You and I.-H. Kim, J. Korean Phys. Soc. **64**, 690 (2014).

279 T.M. Tritt, editor , *Thermal Conductivity* (Springer US, 2004).

280 C. Kittel, *Introduction to Solid State Physics*, 7th ed. (John Wiley & Sons, Inc., New York City, NY, 1996).

281 H. Wang, A.D. LaLonde, Y. Pei, and G.J. Snyder, Adv. Funct. Mater. **23**, 1586 (2013).

282 M.I. Fedorov, D.A. Pshenay-Severin, V.K. Zaitsev, S. Sano, and M.V. Vedernikov, in *Proc. ICT'03. 22nd Int. Conf. Thermoelectr. (IEEE Cat. No.03TH8726)* (IEEE, 2003), pp. 142–145.

283 V.I. Fistul', *Heavily Doped Semiconductors* (Springer New York, Boston, MA, 1995).

284 T. Ando, NPG Asia Mater. **1**, 17 (2009).

285 C. Qin, X. Shi, S.Q. Bai, L.D. Chen, and L.J. Wang, Mater. Sci. Eng. A **420**, 208 (2006).

286 D. Suh, D. Lee, C. Kang, I.-J. Shon, W. Kim, and S. Baik, J. Mater. Chem. **22**, 21376 (2012).

287 F. Ren, H. Wang, P.A. Menchhofer, and J.O. Kiggans, Appl. Phys. Lett. **103**, 221907 (2013).

288 Y. Zhang, X.L. Wang, W.K. Yeoh, R.K. Zheng, and C. Zhang, Appl. Phys. Lett. **101**, 031909 (2012).

289 K.T. Kim, S.Y. Choi, E.H. Shin, K.S. Moon, H.Y. Koo, G.-G. Lee, and G.H. Ha, Carbon N. Y. **52**, 541 (2013).

290 Y.H. Yeo and T.S. Oh, Mater. Res. Bull. **58**, 54 (2014).

291 J. Yang and F.R. Stabler, J. Electron. Mater. **38**, 1245 (2009).

292 D. Cederkrantz, N. Farahi, K.A. Borup, B.B. Iversen, M. Nygren, and A.E.C. Palmqvist, J. Appl. Phys. **111**, 023701 (2012).

293 T. Yi, S. Chen, S. Li, H. Yang, S. Bux, Z. Bian, N. a. Katcho, A. Shakouri, N. Mingo, J.-P. Fleurial, N.D. Browning, and S.M. Kauzlarich, J. Mater. Chem. **22**, 24805 (2012).

294 N. Farahi, S. Prabhudev, G. Botton, J. Zhao, J.S. Tse, Z. Liu, J.R. Salvador, and H. Kleinke, J. Alloy. Compd. **644**, 249 (2015).

295 M.S. Dresselhaus, G. Dresselhaus, P.C. Eklund, and A.M. Rao, in *Phys. Fullerene-Based*

Fullerene-Related Mater. (Springer Netherlands, 2000), pp. 331–379.

[296] A.M. Rao, A. Jorio, M.A. Pimenta, M.S.S. Dantas, R. Saito, G. Dresselhaus, and M.S. Dresselhaus, Phys. Rev. Lett. **84**, 1820 (2000).

[297] J.H. Lehman, M. Terrones, E. Mansfield, K.E. Hurst, and V. Meunier, Carbon N. Y. **49**, 2581 (2011).

[298] Y. Zhang, J.-H. Bahk, J. Lee, C.S. Birkel, M.L. Snedaker, D. Liu, H. Zeng, M. Moskovits, A. Shakouri, and G.D. Stucky, Adv. Mater. **26**, 2755 (2014).

[299] A. Shakouri, Annu. Rev. Mater. Sci. **41**, 399 (2011).

[300] A. Soni, Y. Shen, M. Yin, Y. Zhao, L. Yu, X. Hu, Z. Dong, K.A. Khor, M.S. Dresselhaus, and Q. Xiong, Nano Lett. **12**, 4305 (2012).

[301] N.D.Y. Truong, H. Kleinke, and F. Gascoin, Dalt. Trans. **43**, 15092 (2014).

[302] D.L. Medlin and G.J. Snyder, Curr. Opin. Colloid Interface Sci. **14**, 226 (2009).

[303] W. Liu, H.S. Kim, S. Chen, Q. Jie, B. Lv, M. Yao, Z. Ren, C.P. Opeil, S. Wilson, C.-W. Chu, and Z. Ren, Proc. Natl. Acad. Sci. U. S. A. **112**, 3269 (2015).

[304] R. Prasher, Phys. Rev. B **77**, 075424 (2008).

[305] G.A. Slack, J. Appl. Phys. **35**, 3460 (1964).

[306] G.L. Harris, *Properties of Silicon Carbide*, No. 13 (IET, London, UK, 1995).

[307] R. Gerhardt, *Properties and Applications of Silicon Carbide* (InTech, 2011).

[308] D.-W. Liu, J.-F. Li, C. Chen, and B.-P. Zhang, J. Electron. Mater. **40**, 992 (2010).

[309] J.-F. Li and J. Liu, Phys. Status Solidi **203**, 3768 (2006).

[310] N. Farahi, S. Prabhudev, M. Bugnet, G. Botton, J. Zhao, J.S. Tse, J.R. Salvador, and H. Kleinke, RSC Adv. **5**, 65328 (2015).

[311] Y. Zheng, Q. Zhang, X. Su, H. Xie, S. Shu, T. Chen, G. Tan, Y. Yan, X. Tang, C. Uher, and G.J. Snyder, Adv. Energy Mater. **5**, 1401391 (2015).

[312] M. Zebarjadi, K. Esfarjani, M.S. Dresselhaus, Z.F. Ren, and G. Chen, Energy Environ. Sci. **5**, 5147 (2012).

[313] X. Zhou, G. Wang, L. Zhang, H. Chi, X. Su, J. Sakamoto, and C. Uher, J. Mater. Chem. **22**, 2958 (2012).